

DOCTORAL THESIS

Some Novel Algorithms for Processing Sensor Array Output Signals

Allan Tart

TALLINN UNIVERSITY OF TECHNOLOGY
DOCTORAL THESIS
26/2021

Some Novel Algorithms for Processing Sensor Array Output Signals

ALLAN TART



TALLINN UNIVERSITY OF TECHNOLOGY
School of Information Technologies
Thomas Johann Seebeck Department of Electronics

This dissertation was accepted for the defence of the degree of Doctor of Philosophy in Electronics and Telecommunication on April 20, 2021

Supervisor: Tõnu Trump
Virgostell OÜ
Tallinn, Estonia

Co-supervisor: Ivo Mürsepp
Thomas Johann Seebeck Department of Electronics
Tallinn University of Technology
Tallinn, Estonia

Opponents: Prof. Mats Bengtsson
School of Electrical Engin. and Comp. Science
Royal Institute of Technology (KTH)
Stockholm, Sweden

Tuomas Aittomäki
Department of Signal Processing and Acoustics
Aalto University
Espoo, Finland

Defence of the thesis: June 11, 2021, Tallinn

Declaration:

Hereby I declare that this doctoral thesis, my original investigation and achievement, submitted for the doctoral degree at Tallinn University of Technology has not been submitted for doctoral or equivalent academic degree.

Allan Tart

signature



European Union
European Regional
Development Fund



Investing
in your future

Copyright: Allan Tart, 2021
ISSN 2585-6898 (publication)
ISBN 978-9949-83-699-4 (publication)
ISSN 2585-6901 (PDF)
ISBN 978-9949-83-700-7 (PDF)
Printed by Koopia Niini & Rauam

TALLINNA TEHNIKAÜLIKOOL
DOKTORITÖÖ
26/2021

Uudsed algoritmid antennivõre väljundsignaali töötlemiseks

ALLAN TART



To my father.

TABLE OF CONTENTS

LIST OF PUBLICATIONS	9
OTHER RELATED PUBLICATIONS	9
AUTHOR’S CONTRIBUTIONS TO THE PUBLICATIONS.	10
INTRODUCTION	13
NOMENCLATURE	22
1. Array Processing.	25
1.1. Array Models	25
1.1.1. Uniform Rectangular Array.	28
1.1.2. Uniform Linear Array	29
1.2. Data Model	31
1.3. Sample Covariance Matrix.	33
2. Beamforming	35
2.1. Data Independent Beamforming	36
2.2. Data Dependent Beamforming	39
2.2.1. Linearly Constrained Minimum Variance Beamformer	40
2.2.2. Generalized Sidelobe Canceller	40
2.3. Adaptive Beamforming	42
2.4. Robust Beamforming.	44
2.4.1. Robust Data Dependent Beamforming	44
2.4.2. Robust Data Independent Beamforming	45
2.4.3. Robust General Sidelobe Canceller	46
2.5. Chapter Summary	46
3. Direction of Arrival Estimation	49
3.1. Beamforming DOA Estimation Techniques.	50

3.2. Subspace Based Methods	52
3.2.1. MUSIC	52
3.2.2. ESPRIT	53
3.3. Parametric Methods	54
3.3.1. Maximum Likelihood Estimator	54
3.3.2. Maximum A Posteriori Estimator	56
3.4. Performance Comparison	57
3.5. Chapter Summary	59
CONCLUSIONS	61
REFERENCES.	63
ABSTRACT	73
KOKKUVÕTE.	75
APPENDIX A : Two Dimensional Robust Beamforming for Air-Ground Communication System	77
APPENDIX B : Addressing Security Issues in ADS-B with Robust Two Dimensional Generalized Sidelobe Canceller	87
APPENDIX C : Position Report Enhancement Using Bayesian Estimator .	95
APPENDIX D : Robust Adaptive Beamforming for Air Surveillance System using 2D Antenna Array	107
APPENDIX E : OpenSky Report 2020: Analysing In-Flight Emergencies Using Big Data	115
CURRICULUM VITAE	127
ELULOOKIRJELDUS	129

LIST OF PUBLICATIONS

The work of this thesis is based on the following publications :

- A A. Tart and T. Trump, "Two dimensional robust beamforming for air-ground communication system," 2014 Integrated Communications, Navigation and Surveillance Conference (ICNS) Conference Proceedings, Herndon, VA, USA, 2014, pp. B2-1-B2-8, doi: 10.1109/ICNSurv.2014.6819978.
- B A. Tart and T. Trump, "Addressing security issues in ADS-B with robust two dimensional generalized sidelobe canceller," 2017 22nd International Conference on Digital Signal Processing (DSP), London, 2017, pp. 1-5, doi: 10.1109/ICDSP.2017.8096046.
- C A. Tart and T. Trump, "Position Report Enhancement Using Bayesian Estimator," in IEEE Aerospace and Electronic Systems Magazine, vol. 36, no. 1, pp. 4-13, 1 Jan. 2021, doi: 10.1109/MAES.2020.3015604.

OTHER RELATED PUBLICATIONS

- D A. Tart and T. Trump, "Robust adaptive beamforming for surveillance system using 2D antenna array," 2014 Tyrrhenian International Workshop on Digital Communications - Enhanced Surveillance of Aircraft and Vehicles (TIWDC/ESAV), Rome, Italy, 2014, pp. 110-115, doi: 10.1109/TIWDC-ESAV.2014.6945459.
- E X. Olive et al., "OpenSky Report 2020: Analysing in-flight emergencies using big data," 2020 AIAA/IEEE 39th Digital Avionics Systems Conference (DASC), San Antonio, TX, USA, 2020, pp. 1-10, doi: 10.1109/DASC50938.2020.9256787.

AUTHOR'S CONTRIBUTIONS TO THE PUBLICATIONS

Contribution to the papers in this thesis are:

- A In paper presented in [Appendix A] author proposed to use two dimensional beamforming to achieve interference suppression capabilities in an aerial communication system. For that the one dimensional Generalised Sidelobe Canceller (GSC) using Slepian sequences both in the steering and blocking branch as proposed in [1] was extended into two dimensions. The region where no signal suppression is allowed, was defined as a rectangle. Author developed a theoretical basis, performed the simulations and analysed the results. The author wrote the paper and the supervisor helped with the revision and by giving feedback.
- B In paper presented in [Appendix B] author proposed to use two dimensional beamforming to achieve interference suppression capabilities in an aerial communication system similar to what was discussed in [Appendix A]. The main difference between the two is in the angular region, where no signal suppression is allowed. In current case it is defined as a disc. Author developed a theoretical basis, performed the simulation trials and analysed the results. The author wrote the paper and the supervisor helped with the revision and by giving feedback.
- C In paper presented in [Appendix C] author proposed an algorithm that takes signal sources' self knowledge about its position into consideration, when estimating the signals direction of arrival (DOA). Author developed a theoretical basis, performed the simulation trials and analysed the results. The author wrote the paper and the supervisor helped with the revision and by giving feedback.
- D In paper presented in [Appendix D] proposed to use two dimensional robust GSC that uses Slepian sequences in both steering and blocking branches specifically in ADS-B receivers. Author developed a theoretical basis, performed the simulation trials and analysed the results. The author wrote the paper and the supervisor helped with the revision and by giving feedback.

- E The paper presented in [Appendix E] analyses emergency squawks transmitted by aircraft in distress situations, their causes and consequences. Author contributed to with analysing the geographical distribution of the emergencies and providing feedback to the principal author.

INTRODUCTION

Although array processing algorithms date back a while with some of its most notable algorithms originating back from the 1970s and 1980s (e.g. [2, 3]) it continues to play a key role in modern communication systems. Due to that the field is very much in focus of the research community. We will give two examples, where the potential of an array processing has been widely recognised by the community: telecommunications and air surveillance systems used in civil aviation.

Array Processing in Mobile Communications

The mobile data traffic growth forecast in [4] says that in the Global average around 34GB of data per smartphone will be used by 2026. In the same time in North America for example, the consumed data volume is expected to be more than 45GB per month per smartphone. It is worth noting that these numbers do not include data generated by other types of use cases (e.g. Internet-of-Things (IoT), Fixed Wireless Access (FWA), etc), each having their specific service level requirements (e.g. latency and reliability). Needless to say, data demand is significant, and will put a lot of pressure to mobile networks.

In [5, 6] authors argue that occupying additional frequency bands in the millimetre wavelength regions and implementing massive MIMO will cater to the ever increasing data demand needs. Authors in [7] showed in their study that the mmW (millimetre wave) has a great potential in 5G networks and in MIMO systems specifically.

Countless research since then and first commercial mmW enabled 5G network launched recently¹ show the mmW potential. The high attenuation of the mmW in the propagation environment obviously poses some problems to the mobile systems. Authors in [9] propose to make use of array processing also in the control tasks in contrast to LTE where these tasks are carried out using omnidirectional antenna patterns.

In [10, 11, 12] the benefits of multi user (MU)-MIMO and one of its enablers beamforming is discussed. Authors argue that large arrays can be used to provide a very high beamforming gain and spatial multiplexing of users, thereby

¹Story in Wired [8] suggest that in second half of 2020 two of the network operators combined proved mmW enabled mobile service in around 80 cities across US.

increasing spectral and energy efficiency. Authors in [13] have reported that MU-MIMO largely outperforms the conventional MIMO in terms of achievable data rates. The benefits are achieved through the usage of large-scale antenna arrays which accompanies the usage of mmW and higher frequencies as discussed in [14] for example. In addition to the latter, a study presented in [15] gives a comprehensive overview about the current status of state-of-the-art signal processing techniques and related challenges. Authors argue that even though a lot has been done, there is still a lot to improve in order to keep up with the increasing demands.

While a large amount of effort has been put into developing the 5G systems supporting strict requirements on data throughput, latency and reliability, the scientific community has proposed further directions for the mobile networks. For example [16] predicts that MU-MIMO eventually will lead to cell-free mobile networks. Others, for example [17, 18, 19] are setting a scene for 6G networks where large scale antenna arrays and MU-MIMO system enhancements play again key enabling roles.

Much of the research today is focusing on improving Channel State Information (CSI) estimation efficiency. As pointed out in [20], in addition to channel gain, channel matrix contains information about DOA, so being able to retrieve knowledge about transmitter location efficiently will reduce the CSI estimation effort.

Array Processing in Air Surveillance Systems

The cornerstone of modern air surveillance systems used in Air Traffic Control (ATC) is Secondary Surveillance Radar (SSR). Originally it was developed and used in the 1940s during World War II, where it was called “Identification Friend or Foe” (IFF). In addition to being a surveillance system, SSR can also be looked at as a communication system. Using a transponder, located on board of an aircraft, target identification and altitude information is transmitted to ATC. The ground segment of the system interrogates at 1030 MHz frequency and transponder transmits a replay message at 1090 MHz. [21, 22, 23]

All the technical details of a SSR system are formally set out in [24]. In [25] some background for its design choices is given. Both those sources reveal that the key requirement of the SSR based surveillance system has always been the interoperability with existing ATC systems. That has made it virtually impossible to eliminate the root causes of the problems with the surveillance systems. One of them being saturation of the up-link and down-link channels that results with replay messages overlapping in time. Some of the issues where overlapped replay messages can lead to is discussed in [26] (also presented in [Appendix E]). The study shows that a considerable number of emergency codes (Mode A codes: 7500 for hijacking, 7600 for radio failure and 7700 for general emergencies) are unreliable because they are most probably wrongly decoded. The most probable cause for the erroneous decoding is overlapped messages

and failure of the replay separation (or "de-garbling") algorithms. The issue is getting worse as [27] forecasts up to 84% traffic forecast by the year 2040. As a result, garbling of the surveillance signals and the issues caused by that get more severe².

Yet another issue of the modern air surveillance system is the lack of security measures [29]. Especially prone to lack of security related vulnerabilities is the technique called ADS-B (Automatic dependent Surveillance System - Broadcast). ADS-B is a surveillance technique, where aircraft broadcasts its self determined position to surrounding receivers [30]. As is shown in [29, 31, 32, 33, 34] for example, it is relatively effortless to adversely interfere with the systems behaviour. Although, several different data link protocols have been standardised for ADS-B (e.g. VDL Model 4 and UAT [35, 36]) the SSR based Extended Squitter (1090ES) (described in [37]) has taken a dominant role in the field. To illustrate its dominance we note that 1090ES has been named as a means for compliance to Surveillance Performance and Inseparability Rule (SPI IR) [38, 39]. SPI IR is a law passed by the European Council that mandates the usage of ADS-B in the majority of aircraft. The 1090ES also carries a lead role in the USA air space as well [40]. Obviously, the flaws in a safety critical system that is so wide spread across the globe need to be addressed. We argue that the array processing can employed to mitigate at least some of the issues listed above.

Array processing has been an integral part of surveillance systems for a long time. For de-garbling and angular resolution enhancement array processing has been proposed in [41, 42, 43, 44]. For mitigating the security risks, different array processing based approaches have been proposed e.g. [45, 46, 47, 48, 49, 50]. Nevertheless, ever-increasing complexity of the airspace and involvement of new actors as suggested in [51, 52, 53, 54] will definitely require robust and well performing methods for communications purposes.

Contribution of the Thesis

The thesis contributes to two main parts of the array processing: *beamforming* and *Direction of Arrival (DOA) estimation*.

The contribution was made by answering to the following research questions:

1. How to implement Slepian sequences in the steering and blocking branch of a two dimensional Robust Generalized Sidelobe Canceller (R-GSC)?
2. For the R-GSC with Slepian sequences, how to define the uncertainty region as a rectangle?
3. For the R-GSC with Slepian sequences, how to define the uncertainty region as a disc?

²Forecast published in [28] suggest that the effect of COVID on the air traffic growth is short term looking from the 2040 perspective

4. What is the R-GSC with Slepian sequences performance in terms of achievable Signal-to-Interference-plus-Noise-Ratio (SINR) and how does it compare to data dependent robust adaptive GSC?
5. Can the R-GSC with Slepian sequences be used to *de-garble* the ADS-B messages?
6. How to fuse signal source knowledge about its location with signal DOA estimated by an antenna array?
7. Can data fusion method work reliably without specific knowledge about the received signal strength and the noise power?
8. What is the method's performance in terms of Mean Square Error (MSE) and how does it compare to other DOA estimation algorithms?

The Author's contribution to the field of array processing is summarised below.

In the field of beamforming, the thesis presents a robust Generalised Sidelobe Canceller (GSC) based beamformer that uses two dimensional Slepian sequences with large energy concentration capabilities both in steering and blocking branches. In [Appendix A] and [Appendix D] angular region, where the target is expected to be, is defined as rectangle. In [Appendix B] the angular region is defined as a disc. The proposed methods allow accurately steer the antenna electronically toward desired azimuth and elevation angle while choosing appropriate uncertainty/robustness region. The method can be used in air surveillance systems for de-garbling the overlapping signal. In 5G base stations to mitigate the inter- and intracell interference or avoid interfering with satellite systems as reported in [55].

In the field of DOA estimation the thesis presents an Maximum A Posteriori (MAP) algorithm that utilises targets self knowledge about its position. At the same time, no knowledge about the signal power or noise power is assumed. In [Appendix C] it is shown that the proposed method outperforms ML and MUSIC in case of small number of array elements and high array covariance matrix estimation error.

Outline of the Thesis

This section provides an outline of the thesis with a brief summary of the material presented in each chapter.

Chapter 1: Array Processing. Brief introduction to the field of array processing is given in this chapter. It includes some basic definitions and relations that are used for synthesising and analysing arrays.

Chapter 2: Beamforming. An overview of beamforming algorithms is given. The main goal is to compare different types of beamforming techniques and provide some motivation for the work presented in the appendices.

Chapter 3: Direction of Arrival Estimation. An overview of DOA estimation algorithms is given. The main goal of this chapter is to compare different types of DOA estimation techniques and provide some motivation for the work presented in the appendices.

Conclusions. This chapter concludes the work by summarising the work presented and provides some ideas for the future work.

NOMENCLATURE

ABBREVIATIONS:

(N)LMS (Normalised) Least Mean Square

(R)-GSC (Robust) - General Sidelobe Canceller

5G 5th generation of mobile communication system

ADS-B Automatic dependent Surveillance - Broadcast

AoA Angle of Arrival

AoD Angle of Departure

ATC Air Traffic Control

DOA Direction of Arrival

ESPRIT Estimation of Signal Parameters via Rotational Invariance Techniques

FWA Fixed Wireless Access

GB giga-byte, a measure of data volume.

IoT Internet of Things

LCMV Linearly Constrained Minimum Variance

MAP Maximum A Posteriori

ML Maximum Likelihood

MUSIC Multiple Signal Classification

MVDR Minimum Variance Distortionless Response

m meter, a unit of length.

NM nautical mile, a unit of length, 1 NM \sim 1.852 m.

SINR Signal to Noise and Interference Ratio

SNR Signal to Noise Ratio

SSR Secondary Surveillance Radar

UAT Universal Access Transceiver

ULA Uniform Linear Array

URA Uniform Rectangular Array

VDL Model 4 VHF Data Link - Mode 4

VHF Very High Frequency

s.t. subject to

SYMBOLS:

Ψ diagonal matrix with $\exp(ju_l)$ on its main diagonal ($l = 0, \dots, L$).

$[\cdot]^*$ conjugate of a scalar variable.

$[\cdot]^H$ Hermitian (conjugate) transpose of a matrix

$[\cdot]^T$ transpose of a matrix.

$\|\cdot\|_F$ Frobenius norm of a matrix.

Π^\perp orthogonal projections of a matrix onto noise subspace.

Π orthogonal projections of a matrix onto signal subspace.

ΔT time it takes for plane wave to fully illuminate an array.

Δu defines the span of angular region, where beamformer should not suppress an incoming signals.

\det determinant of a matrix.

ϵ mean square error.

η signal to interference plus noise ratio.

$\hat{\cdot}$ estimate of some arbitrary parameter.

λ signal wavelength.

\ln natural logarithm.

$\mathcal{N}(\mu, \sigma^2)$ normal distribution with mean μ and variance σ^2 .

$\mathcal{U}(a, b)$ uniform distribution between lower bound a and upper bound b .

$Re\{\cdot\}$ real part of a complex number.

$\text{diag}[\cdot]$ diagonal matrix, bracketed vector reveals elements on its main diagonal

$\max(\cdot)$ largest value of a set.

ϕ elevation angle of the signal source.

τ_m wave propagation delay.

$\mathbf{0}$ null matrix.

\mathbf{a} signal sampled at locations \mathbf{p} at time instance t .

\mathbf{C}_b blocking matrix, responsible for suppressing the desired signal in the blocking branch in GSC.

\mathbf{D} diagonal matrix with eigenvalues of \mathbf{R}_x on its main diagonal in descending order.

\mathbf{p}_m vector containing the locations of an array elements.

\mathbf{r} array response vector $\mathbf{r} = [r_0, r_1, \dots, r_{L-1}]$.

\mathbf{R}_x data covariance matrix $\mathbf{R}_x = E[\mathbf{x}\mathbf{x}^H]$.

\mathbf{T} nuisance parameter in ESPRIT.

\mathbf{U} $M \times M$ matrix containing M eigenvectors of the \mathbf{R}_x .

\mathbf{u} unit vector defining the signal field direction of arrival.

\mathbf{U}_n $M \times M - L$ matrix containing noise space eigenvectors of the \mathbf{R}_x .

\mathbf{U}_s $M \times L$ matrix containing signal space eigenvectors of the \mathbf{R}_x .

$\mathbf{U}_{s,i}$ i -th submatrix of signal space eigenvector matrix, used in ESPRIT.

\mathbf{V} steering matrix; steering vectors for each source are the matrix columns.

\mathbf{v} array steering vector.

\mathbf{V}_i i -th submatrix of the steering matrix \mathbf{V} , used in ESPRIT.

\mathbf{w} weight vector of a digital filter.

- \mathbf{w}_a adaptive filter weight vector, part of blocking branch of GSC. The weights **are** continuously updated.
- \mathbf{w}_b weight vector of blocking branch in GSC. The weights **are not** continuously updated.
- \mathbf{w}_s weight vector of steering branch in GSC.
- $\mathbf{x}(t)$ array input signal at time instance t .
- θ azimuth angle of the signal source.
- $A(t)$ signal amplitude at time instance t .
- B_s signal bandwidth.
- c signal propagation velocity in a medium, in the context of current work $c = 3 \times 10^8 m/s$.
- d distance between adjacent ULA elements.
- d_x distance between adjacent URA elements along x -axis.
- d_y distance between adjacent URA elements along y -axis.
- D_{max} largest dimension of an array.
- $E[\cdot]$ mathematical expectations.
- j imaginary unit; $j = \sqrt{-1}$.
- M number of array elements.
- M_x number of URA elements along x -axis.
- M_y number of URA elements along y -axis.
- P_y power of array output signal $y(t)$.
- t discrete time instance within interval $[0, T]$, where T is an observation period.
- u electrical angle of incidence in cases, where the ULA model is used.
- u_x electrical angle of incidence in respect to x axis in cases, where the URA model is used.
- u_y electrical angle of incidence in respect to y axis incidence, where the URA model is used.

LIST OF FIGURES

1.1	N -element array with arbitrary geometry.	27
1.2	Uniform Rectangular Array (URA) with equal spacing d_x and d_y between the elements.	28
1.3	Uniform Linear Array (ULA) with equal spacing d between the elements.	30
1.4	Array signal processor.	32
1.5	Frobenius distance between $\hat{\mathbf{R}}_x$ and \mathbf{R}_x depending on noise variance σ_n^2	33
2.1	Conventional (delay-and-sum) beamformer.	36
2.2	Outputs signal $y(t)$ of data independent beamformers (bottom) together with desired signal $a_0(t)$ (top) and interfering signal $a_1(t)$	38
2.3	Response of data independent beamformers $G(u)$	39
2.4	Generalized Sidelobe Canceller.	41
2.5	Generic adaptive filter.	42
2.6	MSE of different GSC-s implementations.	43
2.7	Array responses of several different data dependent beamformers.	45
2.8	Responses of several different data independent beamformers.	46
3.1	Beamformer normalised output $P_y(u)$ power at different scan angles u	51
3.2	MUSIC normalised pseudospectrum, $P_y(u)$, at different scan angles u	53
3.3	An example of data log-likelihood function.	55
3.4	An example of a log posteriori PDF function	57
3.5	DOA estimate MSE for different algorithms.	59
3.6	DOA estimate MSE for different signal source angular distances.	60

1. Array Processing

This chapter gives a brief introduction to the field of array processing by describing the basic definitions and relations used for synthesising and analysing arrays.

The theoretical background about the beamforming and DOA estimation will follow in Chapter 2 and Chapter 3 and only some of the underlying assumptions will be looked at in the current chapter.

Firstly the target is assumed to be located in the antenna far-field region, i.e. the distance between the array and signal source is greater than $2D_{max}^2/\lambda$, where D_{max} is the largest dimension of the array and λ is the signal wavelength. In this case a plane wave model approximates propagating waves reasonably well and is used throughout the work.

Secondly, regarding the array geometry, discussions will be confined to Uniform Linear Array (ULA) and Uniform Rectangular Array (URA), their models will be revealed in Section 1.1.1 and in Section 1.1.2 in current chapter.

Thirdly, it is acknowledged that all real array elements do have their radiation patterns but in current work isotropic array elements are considered, i.e., all array elements have 0 dB gain in all directions.

And lastly, we only consider **narrowband** arrays by requiring

$$B_s \cdot \Delta T \ll 1, \quad (1.1)$$

where B_s is a bandwidth of the impinging signal and ΔT is the time it takes for the impinging signal to fully illuminate the array.

1.1. Array Models

Let us consider a plane wave travelling in the direction described by a vector \mathbf{u}

$$\mathbf{u} = \begin{bmatrix} -\sin(\theta) \cos(\phi) \\ -\sin(\theta) \sin(\phi) \\ -\cos(\theta) \end{bmatrix}, \quad (1.2)$$

where θ is azimuth angle and ϕ is elevation angle of signal source relative to the centre point of the coordinate system.

At any given time instance t at arbitrary location in space \mathbf{p}_m a plane wave can be described with the following equation

$$a(t, \mathbf{p}_m) = \text{Re}\left\{A(t) \exp\left[j(\omega t - \mathbf{k}^T \mathbf{p}_m)\right]\right\}, \quad (1.3)$$

where $A(t)$ is the signal amplitude, ω is the signal temporal angular frequency and \mathbf{k} is a the wave vector

$$\mathbf{k} = \frac{2\pi}{\lambda} \mathbf{u}. \quad (1.4)$$

Note that in (1.3), we assume interference has not corrupted the signal.

The sampling location vector \mathbf{p}_m is given by

$$\mathbf{p}_m = [p_{x_m}, p_{y_m}, p_{z_m}]^T, \quad (1.5)$$

where $p_{x_m}, p_{y_m}, p_{z_m}$ are the x, y, z coordinates.

Note that the wave propagation time from coordinate system centre point to the array element location \mathbf{p}_m , denoted by τ_m is

$$\tau_m = \frac{\mathbf{u}^T \mathbf{p}_m}{c}, \quad (1.6)$$

where c is the velocity of propagation. We will return to this relation later in our discussions.

The magnitude of the wave vector $|\mathbf{k}| = \frac{2\pi}{\lambda}$ is often called 'wave number' or 'spatial angular frequency' and describes how many oscillations the wave completes per unit in space. (In contrast, ω is the 'temporal angular frequency' describing how many oscillations does a wave complete per unit in time.)

In case of arbitrary shaped array with M spatially distributed elements in the locations \mathbf{p}_m with $m = 0 \dots M-1$ (Figure 1.1), signal samples can be collected and gathered into the vector $\mathbf{a}(t, \mathbf{p})$.

$$\mathbf{a}(t, \mathbf{p}) = A(t) \exp(j\omega t) \mathbf{v}(\mathbf{k}). \quad (1.7)$$

Note that exponents of $-\mathbf{k}^T \mathbf{p}_m$ in (1.3) has gathered into the vector $\mathbf{v}(\mathbf{k})$

$$\mathbf{v}(\mathbf{k}) = \left[\exp(-j\mathbf{k}^T \mathbf{p}_0), \exp(-j\mathbf{k}^T \mathbf{p}_1), \dots, \exp(-j\mathbf{k}^T \mathbf{p}_{M-1}) \right]^T \quad (1.8)$$

The vector $\mathbf{v}(\mathbf{k})$ is often referred to as an 'array steering vector' and it plays a centre role in the array processing and therefore also in current work. Argument \mathbf{k} describes the direction from which the signal is impinging the array.

For ease of notation in the following discussions variables dependence on the array element position \mathbf{p} will be dropped.

The product $\mathbf{k}^T \mathbf{p}_m$ will also be important in the array processing and therefore it is worth a while to write it out

$$\mathbf{k}^T \mathbf{p}_m = -\frac{2\pi}{\lambda} \left[\sin(\theta) \cos(\phi) \cdot p_{x_m} + \sin(\theta) \sin(\phi) \cdot p_{y_m} + \cos(\theta) \cdot p_{z_m} \right] \quad (1.9)$$

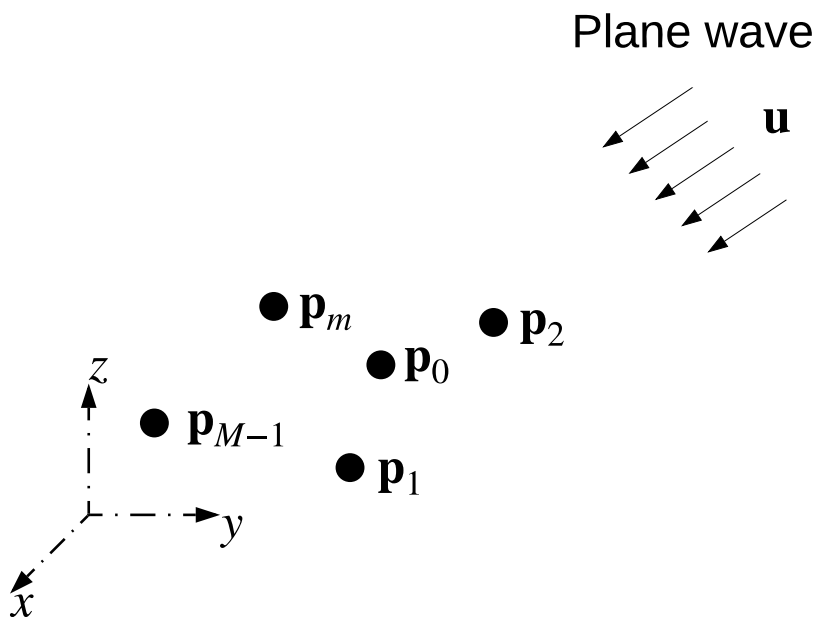


Figure 1.1 N -element array with arbitrary geometry.

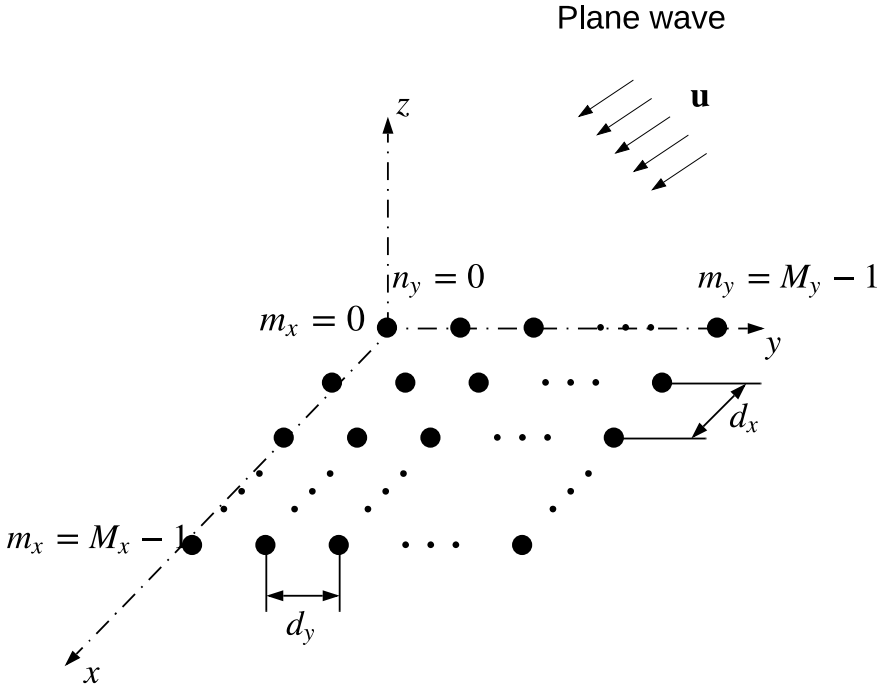


Figure 1.2 Uniform Rectangular Array (URA) with equal spacing d_x and d_y between the elements.

The m -th element of a steering vector $\mathbf{v}(\mathbf{k})$ takes the following form

$$[\mathbf{v}(\theta, \phi)]_m = \exp \left(j \frac{2\pi}{\lambda} \left(\sin(\theta) \cos(\phi) \cdot p_{x_m} + \sin(\theta) \sin(\phi) \cdot p_{y_m} + \cos(\theta) \cdot p_{z_m} \right) \right) \quad (1.10)$$

Making some reasonable assumptions about the layout of an array and about the placement of the sensors within an array, (1.10) can be simplified into a more convenient form. In the following sections some most commonly used array models are looked at: uniform rectangular array (URA) and uniform linear array (ULA). Both of these array models are used in the discussions about beamforming and direction of arrival estimation in following chapters of current work and also in the articles presented in the appendices.

1.1.1. Uniform Rectangular Array

Uniform rectangular array of interest is shown on Figure 1.2. For the convenience of analysing the array, it has been laid down to a x, y -plane (direction of z -axis in this case, is referred to as the 'array boresight'). Its elements are set in orderly

fashion with M_x elements along x -axis and M_y elements along y -axis. Each element can be indicated using its order number $[m_x, m_y]$.

Without the loss of generality, the centre point of a coordinate system is chosen so that it coincides with the element $[0, 0]$. The position of a $[m_x, m_y]$ -th array element can be denoted by coordinate $[p_{x_m}, p_{y_m}]$, where

$$p_{x_m} = m_x d_x, \quad m_x = 0 \dots M_x - 1, \quad (1.11)$$

$$p_{y_m} = m_y d_y, \quad m_y = 0 \dots M_y - 1, \quad (1.12)$$

where d_x and d_y are element spacings along x -axis and y -axis respectively.

If spacing between adjacent array elements along both axis will be the same and equal to half of the signal wavelength λ , i.e. $d_x = d_y = \frac{\lambda}{2}$, the element position vector \mathbf{p}_m takes the form

$$\mathbf{p}_m = \begin{bmatrix} p_{x_m} \\ p_{y_m} \\ 0 \end{bmatrix} = \begin{bmatrix} m_x d_x \\ m_y d_y \\ 0 \end{bmatrix} = \begin{bmatrix} 0.5\lambda m_x \\ 0.5\lambda m_y \\ 0 \end{bmatrix}. \quad (1.13)$$

Equation (1.6) can be rewritten

$$\mathbf{k}^T \mathbf{p}_m = -\pi \left[\sin(\theta) \cos(\phi) \cdot m_x + \sin(\theta) \sin(\phi) \cdot m_y \right] \quad (1.14)$$

$$= -(m_x u_x + m_y u_y), \quad (1.15)$$

where the following ancillary variables have been defined

$$u_x = \pi \sin(\theta) \cos(\phi), \quad (1.16)$$

$$u_y = \pi \sin(\theta) \sin(\phi). \quad (1.17)$$

Note that both u_x and u_y are in the interval $-\pi \dots \pi$ and in literature are often referred to as 'electrical angle of incidence', we will follow this practice in current work.

The steering vector given by (1.8) can now be written

$$\mathbf{v}(u_x, u_y) = \begin{bmatrix} 1 \\ \exp(ju_x + ju_y) \\ \vdots \\ \exp \left[j(M_x - 1)u_x + j(M_y - 1)u_y \right] \end{bmatrix}. \quad (1.18)$$

1.1.2. Uniform Linear Array

Revealing ULA, illustrated on Figure 1.3, steering vector is analogous to URA. In this case all M elements of an array are located on the z -axis with uniform spacing equal to d . Similarly with URA, each element can be indicated using its

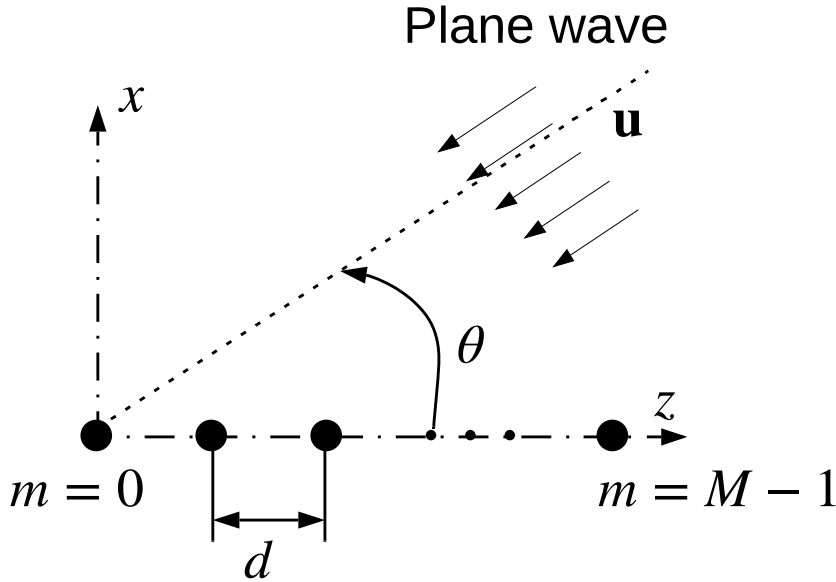


Figure 1.3 Uniform Linear Array (ULA) with equal spacing d between the elements.

order number m and the first element of an array ($m = 0$) is placed at the origin of the coordinate system.

By setting distance between adjacent elements to half of the signal wavelength ($d = \frac{\lambda}{2}$), m -th the element location vector \mathbf{p}_m will take the form

$$\mathbf{p}_m = \begin{bmatrix} 0 \\ 0 \\ md \end{bmatrix}, \quad (1.19)$$

where $m = 0 \dots M - 1$. The product $\mathbf{k}^T \mathbf{p}$ will become

$$\mathbf{k}^T \mathbf{p} = -\pi \cos(\theta) \quad (1.20)$$

$$= -u, \quad (1.21)$$

where we have defined

$$u = \pi \cos(\theta) \quad (1.22)$$

The array steering vector can now be expressed by the following equation

$$\mathbf{v}(u) = \begin{bmatrix} 1 \\ \exp(ju) \\ \vdots \\ \exp(j(M-1)u) \end{bmatrix} \quad (1.23)$$

Likewise to URA, the variable u in ULA model is referred to as 'electrical angle of incidence' and lies within the range $[-\pi, \pi]$.

1.2. Data Model

In this section array signal model is revealed. We assume that signals transmitted by L spatially separated sources reach the antenna array simultaneously, each described by (1.7). To simplify notions $s_l(t) = A_l(t) \exp(j\omega t)$ will be defined, evading references to temporal frequency ω .

All signals travelling through the propagation environment are distorted by additive noise, we have aggregated all such distortions to noise term $\mathbf{n}(t)$, a vector matching the length of the array steering vector. The signal on array elements, gathered into vector $\mathbf{x}(t)$, reveals:

$$\mathbf{x}(t) = s_0(t)\mathbf{v}_0 + \sum_{l=1}^{L-1} s_l(t)\mathbf{v}_l + \mathbf{n}(t). \quad (1.24)$$

Note that we have dropped making explicit reference to signal direction of arrival in the steering vector \mathbf{v} . Instead, subscript is used to indicate the origin of the signal and steering vectors dependence on signals direction of arrival is implicit. We will use subscript 0 to indicate signal from desired source while all other signals are considered being interferers.

The (1.24) can be represented in the matrix form

$$\mathbf{x}(t) = \mathbf{V}\mathbf{s}(t) + \mathbf{n}(t), \quad (1.25)$$

where steering vectors are gathered into $M \times L$ array matrix \mathbf{V}

$$\mathbf{V} = [\mathbf{v}_0, \mathbf{v}_1, \dots, \mathbf{v}_{L-1}] \quad (1.26)$$

and signal samples to $L \times 1$ vector $\mathbf{s}(t)$

$$\mathbf{s}(t) = [s_0(t), s_1(t), \dots, s_{L-1}(t)]^T. \quad (1.27)$$

An important characteristic of the signal on array elements is a spatial covariance matrix $\mathbf{R}_\mathbf{x}$

$$\mathbf{R}_\mathbf{x} = \mathbb{E}[\mathbf{x}(t)\mathbf{x}^H(t)] = \mathbf{V}\mathbf{R}_\mathbf{s}\mathbf{V}^H + \sigma_n^2\mathbf{I}, \quad (1.28)$$

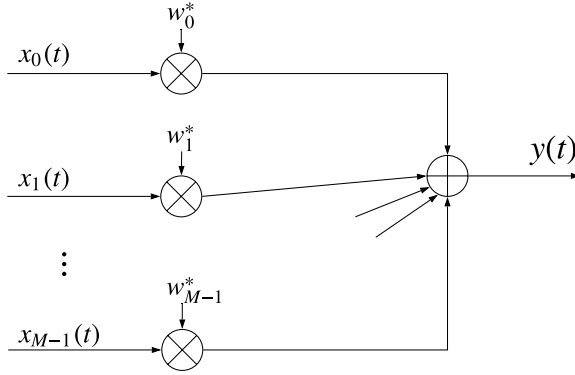


Figure 1.4 Array signal processor.

where $\mathbf{R}_s = E[\mathbf{s}(t)\mathbf{s}^H(t)]$ is a source covariance matrix and $\sigma_n^2\mathbf{I}$ is a noise covariance matrix. Latter implies that noise has a common variance at each array element.

In this work, we assume that signals are statistically independent zero mean random processes which allows the following source covariance model.

$$\mathbf{R}_s = \begin{bmatrix} \sigma_0^2 & 0 & \dots & 0 \\ 0 & \sigma_1^2 & \dots & 0 \\ \vdots & \vdots & \ddots & \vdots \\ 0 & 0 & \dots & \sigma_{L-1}^2 \end{bmatrix}, \quad (1.29)$$

where σ_l^2 is a variance of l -th source signal.

The signal samples involved in $\mathbf{x}(t)$ are usually a subject to a follow-up processing, illustrated on Figure 1.31. It is composed of multiplying signal samples from individual antenna array elements $x_m(t)$ with weights w^* and then adding together the results to form an array output $y(t)$. The procedure represented in matrix form writes

$$y(t) = \mathbf{w}^H \mathbf{x}(t), \quad (1.30)$$

where individual weight values are gathered into a weight vector \mathbf{w} .

Having the weights vector \mathbf{w} , an array can be characterised by its response to signal arriving from given direction u and is defined as

$$G(u) = \mathbf{w}^H \mathbf{v}(u). \quad (1.31)$$

We'll end our data model related discussions by revealing power of an array output signal σ_y^2

$$\sigma_y^2 = E[|y(t)|^2] = \mathbf{w}^H \mathbf{R}_x \mathbf{w}, \quad (1.32)$$

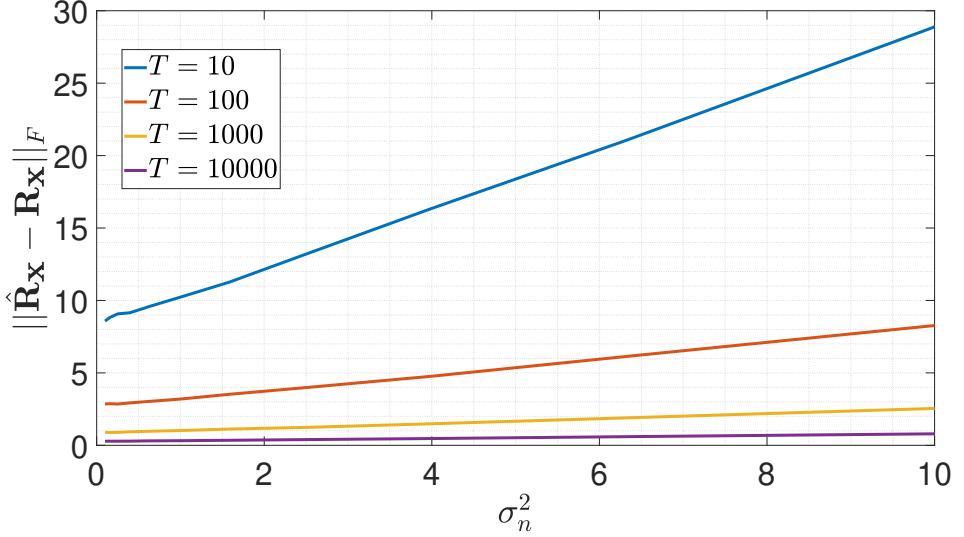


Figure 1.5 Frobenius distance between $\hat{\mathbf{R}}_{\mathbf{x}}$ and $\mathbf{R}_{\mathbf{x}}$ depending on noise variance σ_n^2 .

1.3. Sample Covariance Matrix

In practical settings it is impossible to calculate the array covariance matrix directly using 1.28. Most commonly it is substituted by Sample Covariance Matrix $\hat{\mathbf{R}}_{\mathbf{x}}$

$$\hat{\mathbf{R}}_{\mathbf{x}} = \frac{1}{T} \sum_{t=0}^{T-1} \mathbf{x}(t)\mathbf{x}^H(t), \quad (1.33)$$

where T is an observation period over which the covariance matrix is estimated, $\mathbf{x}(t)$ is array input signal at time instance t with $t = (0, \dots, T)$. To simplify notation, (1.33) can be represented in matrix form

$$\hat{\mathbf{R}}_{\mathbf{x}} = \frac{1}{T} \mathbf{X}\mathbf{X}^H, \quad (1.34)$$

where array signal snapshots $\mathbf{x}(t)$ are gathered into $M \times T$ matrix \mathbf{X} .

It is obvious that the the accuracy with what the sample covariance matrix $\hat{\mathbf{R}}_{\mathbf{x}}$ resembles true covariance matrix $\mathbf{R}_{\mathbf{x}}$ depends on SNR and the number of array signal snapshots T in our disposal. It is illustrated on Figure 1.5, where Frobenius distance between the two in case of different T -s is presented.

We now have revealed all important parameters that are used in current work to describe the array and its input/output signals. In the following chapters we will look at some of the classical beamforming and DOA estimation concepts.

2. Beamforming

In the current chapter an overview of beamforming algorithms is given. The main goal is to compare different types of techniques and provide some motivation for the authors contribution presented in the appendices.

The terminology used in beamforming can be rather confusing. We will make an effort to define the differences in the denotations. The aim is not to establish order in the terminology chaos but to specify the scope of the discussions set out in the current chapter.

The narrowband assumption was mentioned in the introduction of Chapter 1 and as there is no ambiguity in it, we will let it be.

There is, however, some level of ambiguity in terms *analogue*, *digital* and *hybrid* beamforming.

Good explanations of the difference between the *digital* and *analogue* beamforming is given in [56, 57]. In a high level view the difference is straight forward – in digital beamforming, the array weights are applied to discrete valued signals while analogue beamforming works with continuous signals and achieves its objective with phase shifters. This implies, that the main difference between the two is in the method how the array weights are applied to the signal and not so much in how the weights are calculated in the first place.

A more detailed look reveals that digital beamforming provides a higher degree of freedom at the expense of increased complexity [9, 14, 15, 58, 59, 60, 61, 62, 63, 64]. Although promising results with analogue beamforming has been achieved [65, 66, 67], much attention is focusing on *hybrid* beamforming (e.g [58, 68, 69, 70, 71]). In hybrid setting, the array is divided into subarrays, which are controlled independently. With a cost of decreasing the level of freedom, acceptable beamforming performance still can be achieved.

The beamforming in telecommunications domain, while the antenna is in transmission mode (or downlink mode), is often referred to as *precoding*. The challenges are somewhat different, when compared with so-called ”classical” (or receive/uplink) beamforming. Comprehensive overview can be found in [72, 73, 74, 75, 76, 77], in the current thesis these methods will not be reviewed.

The array signal processor in beamforming setting is illustrated on Figure 1.4 and described by (1.30). The effort is focused on recovering the desired signal from the mixture of received signals, i.e. $y(t) \sim s_0(t)$, while surpassing interfering signals and noise. It does that by selecting the array weights vector \mathbf{w} in a way the task will be achieved.

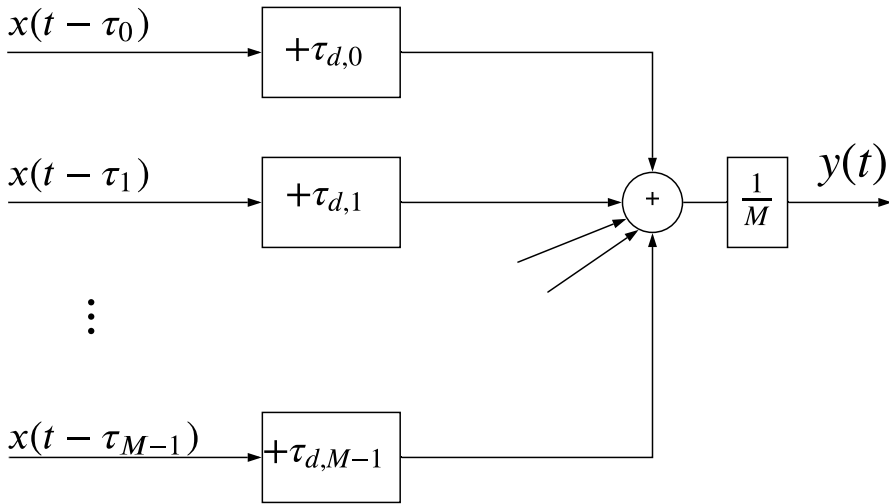


Figure 2.1 Conventional (delay-and-sum) beamformer.

Depending on how values to \mathbf{w} are assigned, beamformers can be classified as either *data independent* or *statistically optimum*. We will briefly look at both by discussing some frequently used algorithms representing the given class of beamformers.

In this chapter, all algorithms use ULA as an array model with all of its implications as described in Section 1.1.2.

The performance of beamformers will be quantified and visualised using either array response $G(u)$ given in (1.32) or Mean Square Error ϵ , in current chapter given by

$$\epsilon = \mathbb{E}[(s_0(t) - y(t))^2]. \quad (2.1)$$

Theory presented in this chapter mainly relays on work presented in [78, 79].

2.1. Data Independent Beamforming

In data independent beamforming the weights in vector \mathbf{w} are chosen so that the array response approximates desired response, independent from data or its statistics.

Let us consider the following setting. At time instance t we wish to receive a signal $s_0(t)$ arriving from a known direction described by u_0 . The desired signal is corrupted by $L - 1$ interfering signals arriving from direction described by u_l , with $l = 1, \dots, L - 1$. If ULA as described in subsection 1.1.2 will be used for

signal reception, array input signal¹ is

$$\mathbf{x}(t) = s_0(t)\mathbf{v}_0 + \sum_{l=1}^{L-1} s_l(t)\mathbf{v}_l. \quad (2.2)$$

In order to receive the desired signal intact, one could delay signal at each element so the signal will be added constructively and consequently, all other signals destructively. Having (1.6) and ULA model in Section 1.1.2, the delay applied on m -th sensor is

$$\tau_m = \frac{mu_0}{\pi c} \quad (2.3)$$

The setup is illustrated on Figure 2.1. Note that after the addition procedure, the output signal is normalised by the number of array elements M to achieve $y(t) \sim s_0(t)$.

Delaying signal at m -th array element is equivalent to multiplication the signal with $\exp(-jmu)$, which is defined as the conjugate of m -th element of the steering vector $\mathbf{v}(u)$. We therefore have effectively defined array weight vector \mathbf{w} as

$$\mathbf{w} = \mathbf{v}^*(u_0) \quad (2.4)$$

and the beamformer is illustrated on Figure 1.4. Array output signal $y(t)$ in this case is

$$y(t) = \frac{1}{M} \mathbf{w}^T \mathbf{x}(t) \quad (2.5)$$

This type of beamformer is often referred to as *delay-and-sum* or *conventional* beamformer.

The conventional beamformer described above can be generalised to cases where one intends to approximate arbitrary desired response. For example, there might be a strong source of interference in a known direction in which case the desired response is zero. Generally speaking, there are L directions to which a certain response r_l is desired. Steering vectors corresponding to all L directions are gathered into matrix \mathbf{V}

$$\mathbf{V} = [\mathbf{v}(0), \dots, \mathbf{v}(L-1)]. \quad (2.6)$$

The desired responses are gathered into vector \mathbf{r}

$$\mathbf{r} = [r_0, \dots, r_{L-1}]^T. \quad (2.7)$$

¹Note that in this setting, we have discarded additive noise from the model. We act so to highlight the interference rejection capabilities of the array processor. In the examples to follow additive noise is included into the discussions.

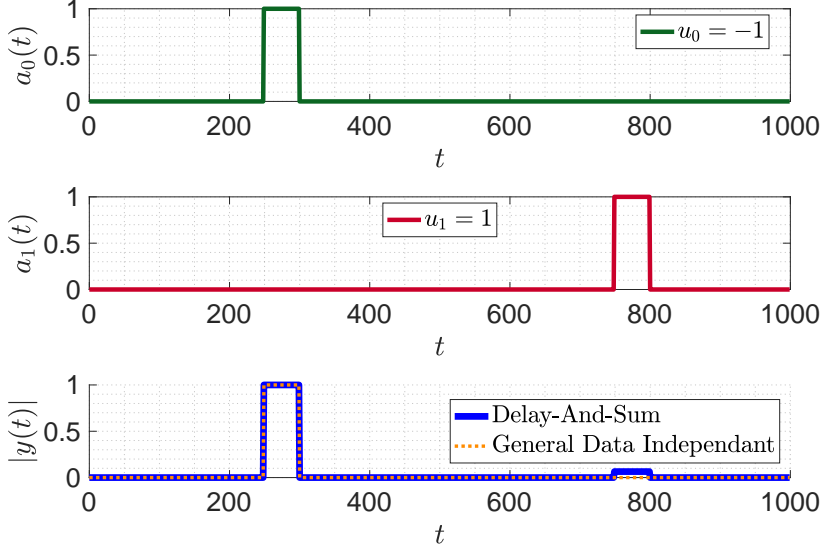


Figure 2.2 Outputs signal $y(t)$ of data independent beamformers (bottom) together with desired signal $a_0(t)$ (top) and interfering signal $a_1(t)$

Natural choice for beamformer design would be via L_2 optimisation, that is choosing \mathbf{w} so that it minimises the squared error between desired and actual array response

$$\min_{\mathbf{w}} |\mathbf{V}^H \mathbf{w} - \mathbf{r}|^2 \quad (2.8)$$

Provided that columns of \mathbf{V} are independent and $\mathbf{V}\mathbf{V}^H$ is invertible, solution to (2.8) is

$$\mathbf{w} = (\mathbf{V}\mathbf{V}^H)^{-1} \mathbf{V}\mathbf{r}. \quad (2.9)$$

To illustrate the performance of delay-and-sum and general data independent beamformers described above, let's view the following example. We have two signal sources at locations $u_0 = -1$ and $u_1 = 1$ each transmitting a single rectangular pulse. As usual, subscript 0 indicates desired signal and source, all other as interference. Hence, the desired array response in this example would be $\mathbf{r} = [1, 0]^T$.

To clearly bring forward the spatial filtering capabilities, we have not modelled additive noise in this example.

We use ULA with $M = 10$ elements to receive the signals. The results are shown on Figure 2.2 and 2.3. First figure presents desired signal (top), interfering

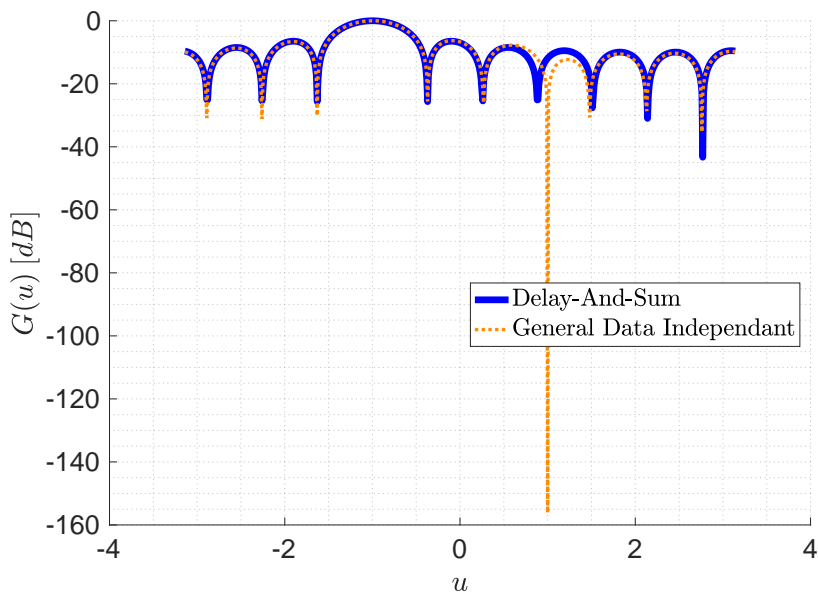


Figure 2.3 Response of data independent beamformers $G(u)$.

signal (middle) and array output signals in case of different beamforming algorithms (bottom) is shown. Second figure presents different beamformers array responses.

The indicated graphs clearly show that both beamformers are able to suppress interfering signals significantly. As one might expect, specifying zeros as the desired response for interfering signal gives better results in spatial filtering.

2.2. Data Dependent Beamforming

Data dependent beamformers, as the name suggests, select array weights based on the statistics of the received signal. Before diving into the subject matter, there are few assumptions that have to be mentioned. Namely, it is assumed that the data is stationary in a wide sense and that its second order statistics are known i.e. data covariance matrix \mathbf{R}_x is known.

There are multitude of different ways for choosing statistically optimal array weight but in the current section only Linearly Constrained Minimum Variance (LCMV) beamformer and Generalised Sidelobe Canceller (GSC) alternative formulation of LCMV as are looked at. Interested readers can turn to the following classical works [78, 79, 80] for a more comprehensive overviews.

The reason for such selection is that LCMV and GSC illustrate relations between different popular beamforming algorithms and are a good basis for further developments.

2.2.1. Linearly Constrained Minimum Variance Beamformer

LCMV beamformer chooses array weights to minimize output signal variance or power subject to response constraints. The constraint is designed to preserve desired signal while minimizing the contributions of interfering signals and noise.

In order to formalise the problem, all L directional constraints are gathered into constraint matrix \mathbf{C}

$$\mathbf{C} = [\mathbf{v}(u_0), \mathbf{v}(u_1), \dots, \mathbf{v}(u_{L-1})]. \quad (2.10)$$

Note that in this case L does not need to be the number of *all* sources. One might interpret it as a number of *known* sources, from which one is a source of desired signal and others sources of interfering signals.

The desired array response corresponding to each known signal source will be gathered into response vector \mathbf{r}

$$\mathbf{r} = [r_0, r_1, \dots, r_{N-1}]^T. \quad (2.11)$$

The problem can be presented

$$\min_{\mathbf{w}} \mathbf{w}^H \mathbf{R}_x \mathbf{w} \quad s.t. \quad \mathbf{C}^H \mathbf{w} = \mathbf{r}, \quad (2.12)$$

where \mathbf{R}_x is array input covariance matrix.

The problem (2.12) is typically solved using Lagrange multiplier method and the solution is given by

$$\mathbf{w}^H = \mathbf{r}^H (\mathbf{C}^H \mathbf{R}_x^{-1} \mathbf{C})^{-1} \mathbf{C}^H \mathbf{R}_x, \quad (2.13)$$

An important thing to note here is that the number of linear constraints in (2.11) is bounded by the number of array elements M . Meaning with L constraints, there will be only $M - L$ degrees of freedom available to minimizing variance.

2.2.2. Generalized Sidelobe Canceller

In this subsection an alternative representation of LCMV beamformer is given. It is called Generalized Sidelobe Canceller (GSC) and it can be used to simplify LCMV implementation.

As GSC has found profound treatment in several classical array processing works (for example [79, 81]), in current work, following [78], only some of the key aspects are given.

LCMV beamformer weight vector, given by (2.13) can be divide into two orthogonal components so that

$$\mathbf{w} = \mathbf{w}_s - \mathbf{w}_b. \quad (2.14)$$

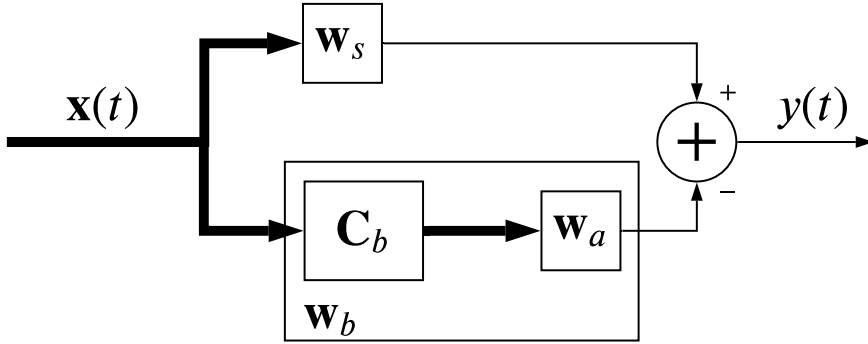


Figure 2.4 Generalized Sidelobe Canceller.

Let's assume that \mathbf{w}_s lies in a range of \mathbf{C} , hence \mathbf{w}_b has to lie in a null space of \mathbf{C} . By definition,

$$\mathbf{C}\mathbf{w}_b = \mathbf{0}, \quad (2.15)$$

therefore

$$\mathbf{w}_s = \mathbf{C}(\mathbf{C}^H\mathbf{C})^{-1}\mathbf{r}, \quad (2.16)$$

as this is the only way to satisfy constraints set in (2.12). Note that (2.16) is equivalent of general data independent beamformer weights given by (2.9) which in turn is a solution to L_2 optimisation problem given by (2.8).

If we define \mathbf{C}_b as a basis for the orthogonal complement of \mathbf{C} and represent \mathbf{w}_b as

$$\mathbf{w}_b = \mathbf{C}_b\mathbf{w}_a, \quad (2.17)$$

the constraint in (2.12) can be rewritten

$$\mathbf{C}^H\mathbf{w}_s - \mathbf{C}^H\mathbf{C}_b\mathbf{w}_a = \mathbf{r}, \quad (2.18)$$

but due to (2.15) latter reduces to

$$\mathbf{C}^H\mathbf{w}_s = \mathbf{r}. \quad (2.19)$$

Equation (2.19) indicates that \mathbf{w}_s is responsible for satisfying the constraints of 2.12 and as \mathbf{w}_a does not depend on constraint matrix \mathbf{C} it provides the degrees of freedom available for minimizing the variance and can be formulated

$$\min_{\mathbf{w}_a} [\mathbf{w}_s - \mathbf{C}_b\mathbf{w}_a]^H \mathbf{R}_x [\mathbf{w}_s - \mathbf{C}_b\mathbf{w}_a]. \quad (2.20)$$

As highlighted earlier, \mathbf{C}_b forms the basis for null space of \mathbf{C} , former can be obtained from the latter using any of the orthogonalization methods.

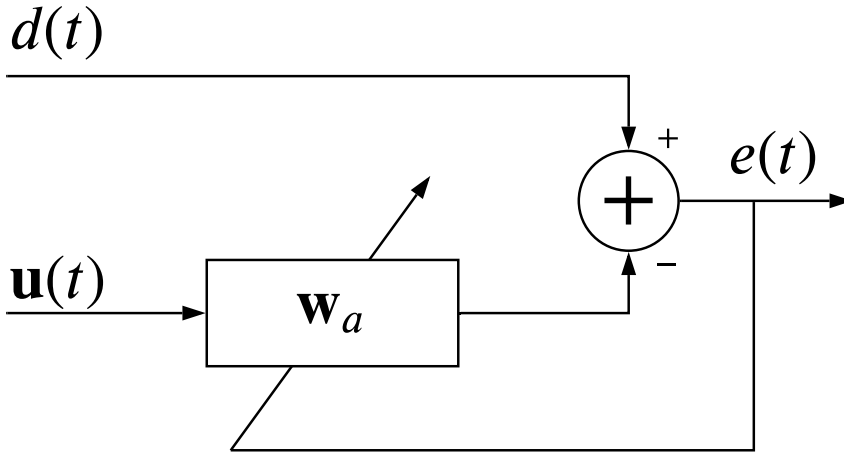


Figure 2.5 Generic adaptive filter.

Solution to (2.20) is

$$\mathbf{w}_b = (\mathbf{C}_b^H \mathbf{R}_x \mathbf{C}_b)^{-1} \mathbf{C}_b \mathbf{R}_x \mathbf{w}_s \quad (2.21)$$

The block diagram of GSC is shown on Figure 2.4. The upper branch is often referred to as *the steering branch*, hence the subscript "s" and lower branch as *the blocking branch*, hence the subscript "b". The use of subscript "a" will become apparent in the following discussions.

2.3. Adaptive Beamforming

The results given in section 2.2 expected that the statistics of received signal are known and exact \mathbf{R}_x can be obtained. In practical settings it obviously is unrealistic expectation and some mechanism to surpass this issue must be employed.

Assuming that signals are ergodic, there are two possible adaptive approaches: *block adaption* and *continuous adaptation*. Former uses a collection of array signal snapshots (i.e. signal blocks) to estimate the signal covariance matrix, the procedure is described in Section 1.3 and will not be repeated here.

In a continuously adaptive approach, array weights are adjusted as the data is sampled resulting weights to converge toward optimum solution.

When examining the structure of GSC shown on Figure 2.4 closer, one notices the resembles with the structure of generic adaptive filter in the interference cancellation setting shown on Figure 2.5. The following substitutions are needed:

$$d(t) = \mathbf{w}_s^H \mathbf{x}(t) \quad (2.22)$$

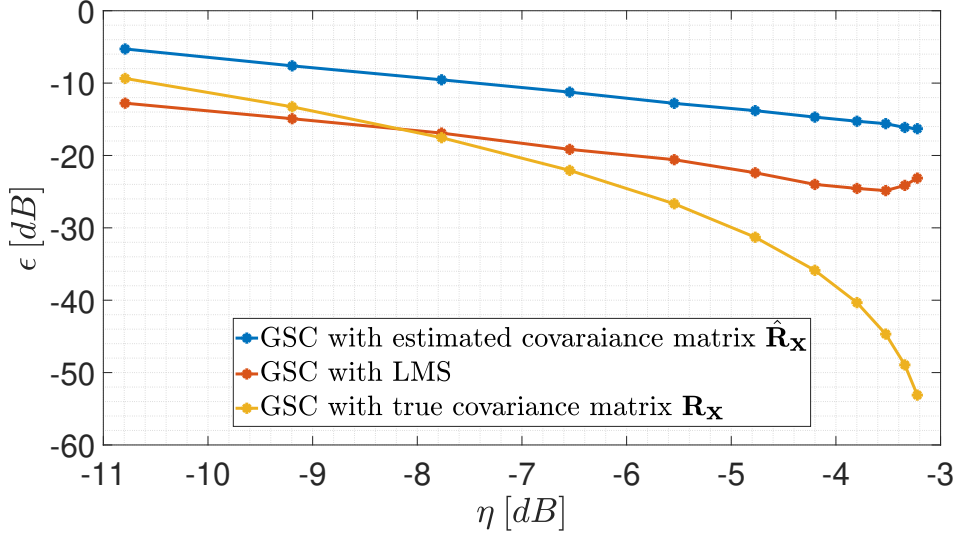


Figure 2.6 MSE of different GSC-s implementations.

and

$$\mathbf{u}(t) = \mathbf{C}_b^H \mathbf{x}(t). \quad (2.23)$$

The adaptive filter \mathbf{w}_a is controlled with the error signal $e(t)$, which is defined as

$$e(t) = d(t) - \mathbf{w}_a^H \mathbf{u}(t). \quad (2.24)$$

Obviously, there are countless possibilities for updating adaptive weights. For each use cases best suited should be chosen and [80] is an excellent guide for making that selection. In the current section, we limit ourselves to describing the *Least Mean Squares (LMS)* algorithm as it is widely used in the family of continuous adaption procedures. The weights are updated according to the following equation

$$\mathbf{w}_a(t+1) = \mathbf{w}_a(t) + \mu \mathbf{u}(t) e^*(t), \quad (2.25)$$

where μ is step size. One instantly notices that in the current case, "error signal" $e(t)$ is actually the array output signal $y(t)$.

On Figure 2.6 MSE of different GSC implementations is shown. In here exact knowledge about all the signal sources is assumed. Desired signal at $u_0 = -1$ with variance $\sigma_0^2 = 1$ and two interfering signals at $u_1 = -2$ and $u_2 = 1.5$ with unitary variances. Additive noise variance $\sigma_n^2 \in [0.1, 10]$. Having variances of interfering sources and noise, SINR η is between -3.2 dB and -10.8 dB. ULA with $M = 10$ is used for spatial filtering. The block size T for calculating $\hat{\mathbf{R}}_{\mathbf{x}}$ according to (1.33) is 100. In current set-up, the block adaptive algorithm

performs the worst in terms of the MSE. But, one can expect that by increasing the block size T , the covariance matrix estimate will be more accurate and this in turn will close the gap between block adaptive GSC (blue) and GSC using true covariance matrix (yellow). When comparing the continuously adaptive GSC (blue) with GSC using true covariance matrix, there is a significant difference in the MSE in good SINR situations, while in poor SINR cases the performance difference is not that significant. The subtle increase of the MSE in the low noise variance situations is caused by the fact that the noise no longer masks the interfering signals and they become more dominant in the array output.

2.4. Robust Beamforming

Thus far we have not assumed any modelling errors and we are counting on having perfect knowledge of array response to the desired signal. In real life this expectation is overly optimistic and some of the typical causes of the performance degradation are erroneous look direction, distorted antenna shape, uncertainties in signal propagation environment (e.g. multipath propagation) and so on. The performance degradation often materialises in a form of desired signal cancellation, where the array treats desired signal as a interference. We now turn our attention toward how to compensate against those issues or in other words, we will examine, how to make an array processor robust against imperfections in the signal transmission chain.

2.4.1. Robust Data Dependent Beamforming

To illustrate the data dependant beamformers sensitivity against model imperfections, a response of LCMV has been given on Figure 2.7 (blue). The graph attempts to capture the effect of mismatch between actual and expected DOA. The main drawback of data dependent beamformers is clearly visible – the model imperfections cause the severe suppression of desired signal as if it were the interfering signal. A multitude of different approaches to make array weight selection robust against these imperfections. Some of the most classical ones have been summarised in [78, 82] for example.

Probably the best known method is imposing a set of gain constraints for a small spread of angles around the nominal look direction, it is often referred to as *point mainbeam constraints*. An example of such beamformer has been shown on Figure 2.7 (red), where $u_0 = -1$ and we have defined constraint matrix $\mathbf{C} = [\mathbf{v}(u_0 - 0.075), \mathbf{v}(u_0 - 0.025), \mathbf{v}(u_0), \mathbf{v}(u_0 + 0.025), \mathbf{v}(u_0 + 0.075)]$ and the corresponding response vector $r = [1, 1, 1, 1, 1]^T$. Although this method is simple to implement, the downside of it is the fact that each additional constraint removes one degree of freedom available to reject undesired signals. We will illustrate the concept with an example.

Another example for making an array robust against imperfections is *eigenvalue threshold method* (yellow on Figure 2.7). First, the beamformer is

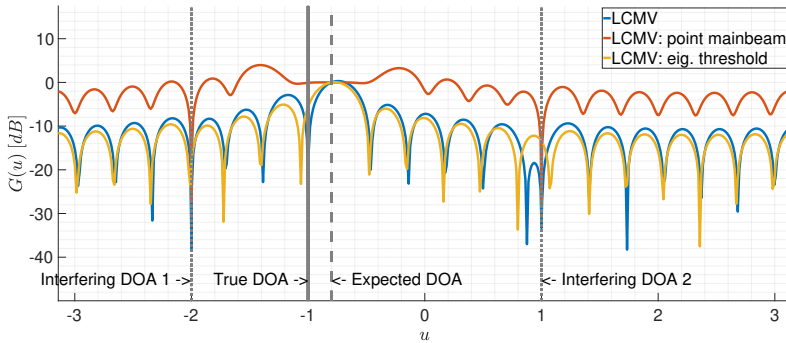


Figure 2.7 Array responses of several different data dependent beamformers.

computed as conventional LCMV. As a second step, covariance matrix \mathbf{R}_x will be modified so that no eigenvalue of it is less than a factor μ times the largest eigenvalue ($0 \leq \mu \leq 1$).

Let $\mathbf{U}\mathbf{D}\mathbf{U}^H$ denote eigenvalue decomposition of \mathbf{R}_x . Matrix \mathbf{D} diagonal elements contain eigenvalues in ascending order, that is $\lambda_1 \geq \lambda_2 \dots \geq \lambda_M$, then m -th eigenvalue will be chosen $\max(\mu\lambda_1, \lambda_m)$ giving us modified eigenvalue matrix \mathbf{D}_{thr} . Using latter, new covariance matrix will be calculated by $\mathbf{R}_{x,thr} = \mathbf{U}\mathbf{D}_{thr}\mathbf{U}^H$ and array weight selection continues as in case of conventional LCMV beamformer given by (2.13). The method works well if μ is chosen appropriately but unfortunately it is not clear how to efficiently choose it.

A thorough treatment of gaining control over efficient constraint selection, while taking into account prior knowledge about array model imperfections and not wasting valuable degrees of freedom can be found in [83]. Negative side effect of unambiguous constraint selection is the growth of computational complexity.

2.4.2. Robust Data Independent Beamforming

Although it is known that data independent beamformers are not as sensitive to erroneous array models as their data dependent siblings, some level of robustness is still needed as is illustrated in Figure 2.8. Blue graph gives an array response of A standard delay-and-sum beamformer. If a mistake has been made and the actual signal DOA falls into the nought of the array pattern, significant attenuation of desired signal will take place.

Data independent beamformer in general, as described by (2.6) - (2.9) gives a possibility to address the uncertainty by imposing additional constraints for a small spread of DOA-s around the expected DOA. The resulting beamformer is given Figure 2.7 with yellow. It can be seen that there is no cancellation of desired signal, but at the same time, the level sidelobes are rather high. As

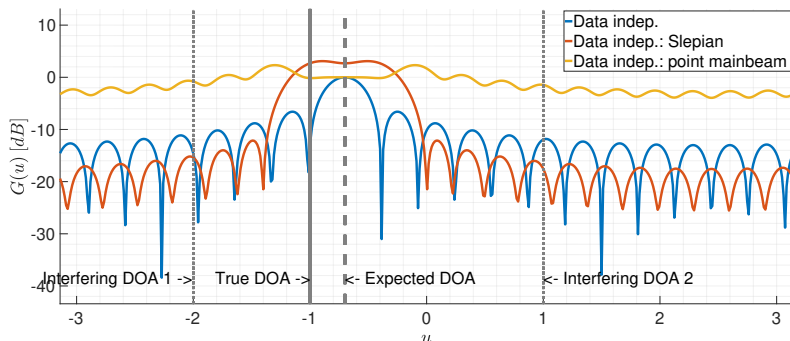


Figure 2.8 Responses of several different data independent beamformers.

data independent beamformers do not have automatic interference cancellation capabilities, it might become a problem.

Another possibility to widen the main beam is to use window functions. An example of that is shown in Figure 2.7 with red. Here, we have used Slepian functions to define window functions. As defined in [84], Slepian functions are sequences that provide maximal energy into a given angular region $[-\Delta u, \Delta u]$, $\Delta u < \pi$. In the simulations so called half time bandwidth product $M \times \Delta u = 3$ and $M = 20$.

2.4.3. Robust General Sidelobe Canceller

As discussed in Section 2.2.2, GSC provides a powerful framework for analysing and synthesising the antenna arrays. It is similarly true for developing robust array processing algorithms. GSC allows to take advantage of both data dependent and data independent beamforming techniques - former provides better interference suppression capabilities whereas latter allows simple and efficient constraint design. For example in [1, 85, 86] it is proposed to use Slepian sequences in steering and blocking branch to obtain robustness against erroneous DOA estimates. In papers presented in [Appendix A], [Appendix B] and [Appendix D] we have extended the theory into two dimensions and proposed to use the GSC with Slepian sequences in cases where line-of-sight propagation model is applicable.

2.5. Chapter Summary

In the current chapter, the different beamforming algorithms were presented. Author's contribution to the field is omitted, it can be found from the appendices of the thesis.

Both the *data independent* and the *data dependent* beamforming techniques were discussed. The difference between the two is in the way array weights are calculated. In former, the array response to arbitrary look direction is specified

and coefficients are used to approximate desired array response; in latter the array weights are calculated based on the transmitted signal statistics.

The general consensus is that the *data dependent* beamforming has superior performance in terms of achievable SINR-s, when compared with the *data independent* algorithms. The downside is that the former is more complex and is more sensitive to mismatches in the processing chain. This in turn can lead to a situation, where the desired signals will automatically be treated as an interference and will be suppressed.

Arrays can be made robust against those mismatches, methods for achieving it were also discussed in the chapter. Robustness against the mismatches is achieved through specifying a region angular, where signal suppression is forbidden. Both *data independent* and *data dependent* approaches provide suitable methods for that.

It was also argued that the GSC, which originates from the *data dependent* branch of beamforming algorithms, provides an excellent framework for discussing *data independent* beamforming too. The two dimensional implementation of a robust GSC is discussed in the [Appendix A], [Appendix B] and the [Appendix D]. The proposed methods allow to steer the array both in a horizontal and in a vertical direction. The algorithm maintains the lower complexity of *data independent* beamformers, while gaining transparency in controlling the angular region, where the signal suppression is not allowed.

3. Direction of Arrival Estimation

Similarly to Chapter 3 our task is here to motivate the work presented in the appendices. We do it by comparing different DOA estimation methods on a basic level to reveal their strengths and weaknesses.

The direction of arrival (DOA) estimation problem as well as classical solutions to the problem have been well described in [79, 87, 88, 89, 90, 91]. Person interested in the field in detail is encouraged to get acquainted with aforementioned references.

Based on [91], for example, DOA estimation algorithm can be divided into three categories:

- **beamforming methods** (as an example - minimum variance distortionless response (MVDR beamformer),
- **subspace methods** (as an example - MUSIC, ESPRIT),
- **parametric methods** (as an example - Maximum Likelihood (ML) estimator).

Before diving into the DOA estimation, let us motivate the usage of DOA estimation over other ways to localise a signal source.

It is well known that a large portion of mobile equipment have positioning capabilities. Obvious choice then would be to make use of this functionality and allow mobile nodes to determine its position and report it to the network (as is case with the ADS-B). Unfortunately, one cannot always rely solely on the mobile terminal self positioning capabilities, for example due to the security issues as was discussed in the introductory part of the thesis. Another reason might be a poor accuracy of the navigation equipment. For example according to [92] data source with horizontal radius of containment $R_C \leq 0.6$ nautical miles (NM) (1111.2 m) is allowed for aircraft manoeuvring on airport surfaces. One can imagine that uncertainty this large is not acceptable in practical settings. The intuition is backed up by [93], where the $R_C \leq 7.5$ meters is specified. In [94] authors analysed ADS-B usage and found that only a marginal part (ca 1% in 2016) of transponders fulfil latter requirement. Because of the unreliability, the ADS-B data with position accuracy category below a certain level is discarded from the sequential data processing.

So called “hybrid frameworks” have been proposed for example in [95, 96], where localisation uses different methods (e.g. array based DOA estimation and

TDOA based systems) simultaneously. Such systems are achieving superior position estimation accuracy when compared with using methods individually. But essentially, robust and reliable DOA estimation methods are still required.

Before moving on, let's recapitulate some of the assumptions used within the chapter. The ULA model is used as an array model with all of its implications described in Section 1.1.2. Signal, observed by an array at time instance t , is

$$\mathbf{x}_t(\mathbf{u}) = \mathbf{V}(\mathbf{u})\mathbf{s}(t) + \mathbf{n}(t), \quad (3.1)$$

where $\mathbf{V}(\mathbf{u})$ is a steering matrix containing steering vectors corresponding to all signals impinging the array. Vector $\mathbf{s}(t)$ contains signal samples from all sources at a time instance t .

Having T such observation ($t = 0, 1, \dots, T - 1$) our task is to reveal \mathbf{u} as effectively and efficiently as possible.

It is also worth a while to repeat some of the assumptions presented in Chapter 1 and are used later in the current chapter.

Source signals samples, congregated into vector $\mathbf{s}(t)$ and noise samples in $\mathbf{n}(t)$ are statistically independent, zero-mean random processes. Then, spatial covariance matrix is

$$\mathbf{R}_x = E[\mathbf{x}(t)\mathbf{x}^H(t)] = \mathbf{V}\mathbf{R}_s\mathbf{V}^H + \sigma_n^2\mathbf{I}, \quad (3.2)$$

with \mathbf{R}_s being a signal covariance matrix and. In practical settings signal covariance matrix \mathbf{R}_s and noise variance σ_n^2 are unknown meaning that the (3.2) can not be computed directly, it is therefore substituted with sample covariance matrix given by

$$\hat{\mathbf{R}}_x = \frac{1}{T} \mathbf{X}\mathbf{X}^H, \quad (3.3)$$

where $\mathbf{X} = [\mathbf{x}_0, \mathbf{x}_1, \dots, \mathbf{x}_{T-1}]$ is a $M \times T$ matrix containing T signal snapshots.

3.1. Beamforming DOA Estimation Techniques

The idea behind beamforming based techniques is to scan over the array look range and measure array output power P_y at all look angles. It is worth noting that here, *mean* power measured over time period T is meant and not the *instantaneous* power. The direction which results in the highest P_y yield the DOA estimate.

Array output power itself is

$$P_y(u) = \mathbf{w}^H(u)\mathbf{R}_x\mathbf{w}(u), \quad (3.4)$$

where $\mathbf{w}(u)$ is an array weight vector assuring that the array is steered toward u .

Obviously there are many ways available for selecting \mathbf{w} , some of those were described in Chapter 2. In the current section we present the MVDR

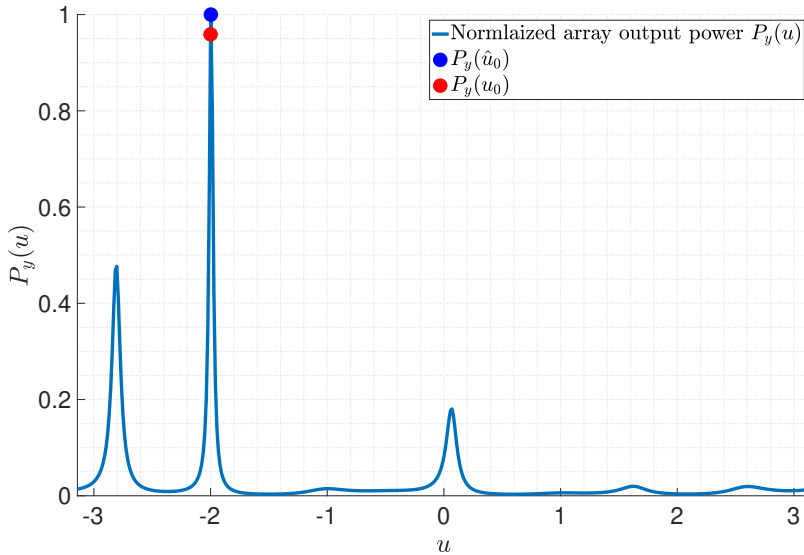


Figure 3.1 Beamformer normalised output $P_y(u)$ power at different scan angles u .

beamforming method (also often referred to as Capone method), which is a special case of LCMV beamformer presented in Section 2.2.1. We will follow the work presented in [87]. In case of MVDR, selecting weights is equivalent to solving a optimisation problem, which writes

$$\min_{\mathbf{w}} \mathbf{w}^H(u) \mathbf{R}_x \mathbf{w}(u) \quad s.t. \quad \mathbf{w}^H(u) \mathbf{v}(u) = 1, \quad (3.5)$$

where $\mathbf{v}(u)$ is a steering vector toward u . Solution to (3.5) is shown to be

$$\mathbf{w}(u) = \frac{\mathbf{R}_x^{-1} \mathbf{v}(u)}{\mathbf{v}^H(u) \mathbf{R}_x^{-1} \mathbf{v}(u)}. \quad (3.6)$$

Substituting (3.6) into (3.5) will yield

$$P_y(u) = \frac{1}{\mathbf{v}^H(u) \mathbf{R}_x^{-1} \mathbf{v}(u)} \quad (3.7)$$

An example of array output power $P_y(u)$ is shown on Figure 3.1. In here, signal from one source is impinging the array, the DOA is equal to -1 . One can witness that the true DOA aligns with the angle where the array output power is highest.

The performance of beamforming based DOA estimation method is examined later in the chapter, together with other methods discussed.

3.2. Subspace Based Methods

In current work we will limit ourselves to describing MUSIC (Multiple Signal Classification) and ESPRIT (Estimation of Signal Parameters via Rotational Invariance Techniques) algorithms. Due to their relatively low complexity and acceptable performance, these algorithms and their extension are most commonly used in a variety of different applications. The main drawback of subspace based methods is loss of resolution in case of low SNR and in small signal samples scenarios.

Subspace based methods DOA estimation methods rely on decomposition of covariance matrix. Having the assumptions given in the beginning of the chapter, decomposition procedure can be performed on covariance matrix \mathbf{R}_x

$$\mathbf{R}_x = \mathbf{U}\mathbf{D}\mathbf{U}^H \quad (3.8)$$

where \mathbf{D} is diagonal matrix containing M eigenvalues of \mathbf{R}_x and the columns of matrix \mathbf{U} are eigenvectors corresponding to eigenvalues in \mathbf{D} . We assume that the latter are in descending order, i.e. $\lambda_1 > \lambda_2 > \dots > \lambda_M > 0$. The eigenvector in \mathbf{U} can be portioned into signal eigenvectors matrix \mathbf{U}_s and noise eigenvectors \mathbf{U}_n

$$\mathbf{U} = [\mathbf{U}_s, \mathbf{U}_n], \quad (3.9)$$

where \mathbf{U}_s contains L first columns of \mathbf{U} and \mathbf{U}_n the remaining $M - L$ columns thus allowing us to define orthogonal projections onto signal and noise subspaces

$$\begin{aligned} \mathbf{\Pi} &= \mathbf{U}_s \mathbf{U}_s^H \\ \mathbf{\Pi}^\perp &= \mathbf{U}_n \mathbf{U}_n^H = \mathbf{I} - \mathbf{\Pi}. \end{aligned} \quad (3.10)$$

Thorough treatment of the subspace methods can be found in [82], where more aspects of the theory presented above is also given.

3.2.1. MUSIC

The MUSIC (Multiple Signal Classification) first introduced in [97], evoked a lot of interest for subspace based methods. In current work we follow the explanation provided in [79] where some other variants of MUSIC algorithms can be found.

The algorithm takes an advantage of the fact that noise eigenvectors in \mathbf{U}_n are orthogonal to steering vectors in \mathbf{V} , i.e.

$$\mathbf{U}_n^H \mathbf{v}(u) = 0, \quad u \in \{u_0, u_1, \dots, u_{L-1}\}. \quad (3.11)$$

Having that, MUSIC spatial pseudospectrum is defined as

$$P_y(u) = \frac{1}{\mathbf{v}(u)^H \mathbf{\Pi}^\perp \mathbf{v}(u)}. \quad (3.12)$$

Although, in MUSIC, P_y is merely a distance between noise and signal subspaces, it tends to have peaks around the true DOA as can be seen on Figure 3.2.

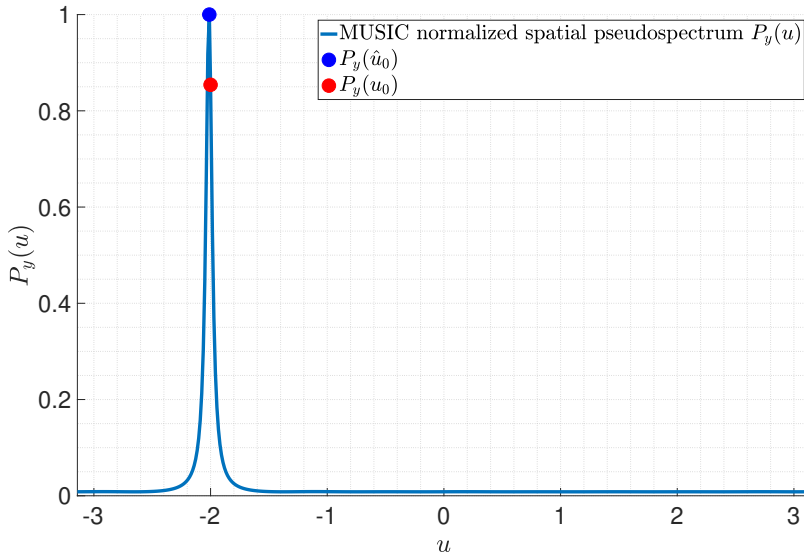


Figure 3.2 MUSIC normalised pseudospectrum, $P_y(u)$, at different scan angles u .

3.2.2. ESPRIT

The ESPRIT that is short for "Estimation of Signal Parameters via Rotational Invariance Techniques", was first introduced in [98]. In current work we follow discussions provided in [79] where other popular variants of the algorithm are also discussed.

The ESPRIT algorithm uses uniform arrays attribute of having a shift structure. Meaning, the steering matrix \mathbf{V} can be divided into sub-matrices

$$\mathbf{V} = \begin{bmatrix} \mathbf{V}_1 \\ \text{last row} \end{bmatrix} = \begin{bmatrix} \text{first row} \\ \mathbf{V}_2 \end{bmatrix} \quad (3.13)$$

Sub-matrices \mathbf{V}_1 and \mathbf{V}_2 are related by the following formula

$$\mathbf{V}_2 = \mathbf{V}_1 \mathbf{\Psi}, \quad (3.14)$$

where $\mathbf{\Psi} = \text{diag}[\exp(ju_0), \exp(ju_1), \dots, \exp(ju_{L-1})]$.

Analogously, the signal space eigenvector \mathbf{U}_s matrix can be partitioned into sub-matrices

$$\mathbf{U}_s = \begin{bmatrix} \mathbf{U}_{s,1} \\ \text{last row} \end{bmatrix} = \begin{bmatrix} \text{first row} \\ \mathbf{U}_{s,2} \end{bmatrix}. \quad (3.15)$$

Sub-matrices of (3.13) and (3.15) are related to each other

$$\mathbf{U}_{s,1} = \mathbf{V}_1 \mathbf{T} \quad \text{and} \quad \mathbf{U}_{s,2} = \mathbf{V}_2 \mathbf{T}, \quad (3.16)$$

where \mathbf{T} is a nuisance parameter and its content is irrelevant for current discussions.

Combing (3.14) and (3.16) yields

$$\mathbf{U}_{s,2} = \mathbf{V}_1 \mathbf{\Psi} \mathbf{T} \quad \text{and} \quad \mathbf{U}_{s,1} = \mathbf{T}^{-1} \mathbf{\Psi} \mathbf{T}, \quad (3.17)$$

which becomes

$$\mathbf{U}_{s,2} = \mathbf{U}_{s,1} \mathbf{T}^{-1} \mathbf{\Psi} \mathbf{T}. \quad (3.18)$$

Matrix $\mathbf{T}^{-1} \mathbf{\Psi} \mathbf{T}$ has the same eigenvalues as $\mathbf{\Psi}$, which are given by $[\exp(ju_0), \exp(ju_1), \dots, \exp(ju_{L-1})]$. From this, finding the DOA-s is a straightforward task of revealing the phase of each eigenvalue.

3.3. Parametric Methods

Parametric methods more fully exploit the underlying data model briefly described in the header of this chapter and bit more thoroughly in Chapter 1.

While making sacrifices in computational complexity, the parametric methods excel in estimation accuracy and robustness when compared with spectral methods described in the previous section in this chapter. The steep increase in complexity is resulted from the multidimensional search required to find an estimate.

We will strict ourselves with describing Maximum Likelihood (ML) technique as it is perhaps the most well known approach and most widely used among parametric estimations methods.

Although thorough overviews about the parametric methods can be found in many places (e.g. [79]), in current work we follow discussions provided in [99]. This applies to Maximum Likelihood and Maximum A Posteriori estimation method.

3.3.1. Maximum Likelihood Estimator

As usual, we assume that the array signal $\mathbf{x}(t)$ is a Gaussian random process. It is argued in the literature that even if this presumption does not hold, the ML derived using the assumption is still applicable to other scenarios and in case of having a large number of samples available, the estimate asymptotically approaches the true value.

First, we will define a parameter vector \mathbf{z} that incorporates all the unknown parameters we seek to find

$$\mathbf{z} = [\mathbf{u}, \sigma^2, \sigma_n^2]^T, \quad (3.19)$$

where \mathbf{u} contains DOA-s and σ^2 contains powers of all L signals captured in $\mathbf{x}(t)$ and σ_n^2 is the noise power. The length of \mathbf{z} is $2L + 1$.

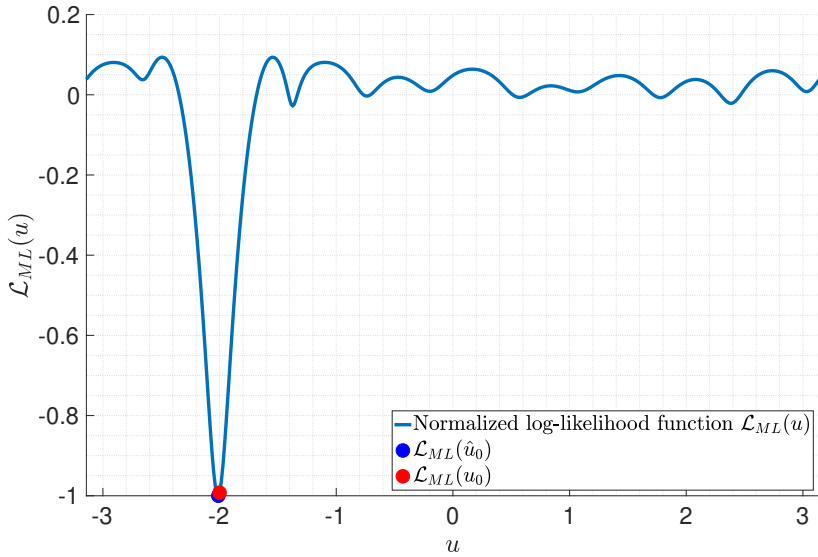


Figure 3.3 An example of data log-likelihood function.

As the name suggest, ML estimator seeks to find the mode of data likelihood function $p(\mathbf{x}(t)|\mathbf{z})$, which having the Gaussian assumption is given by multivariate normal distribution function

$$p(\mathbf{x}_t|\mathbf{z}) = (2\pi)^{M/2} \cdot (\det \mathbf{C}_x(\mathbf{z}))^{-1/2} \cdot \exp\left(-0.5 \text{Tr}\left(\hat{\mathbf{R}}_x \mathbf{C}_x^{-1}(\mathbf{z})\right)\right), \quad (3.20)$$

where $\hat{\mathbf{R}}_x = E[\mathbf{x}_t \mathbf{x}_t^H]$ and $\mathbf{C}_x(\mathbf{z})$ is parametric array covariance matrix given by

$$\mathbf{C}_x(\mathbf{z}) = \mathbf{V}(\mathbf{u}) \mathbf{R}_s(\sigma^2) \mathbf{V}^H(\mathbf{u}) + \sigma_n^2 \mathbf{I} \quad (3.21)$$

Common practice is to convert (3.20) into negative log-likelihood function $\mathcal{L}_{ML}(\mathbf{z})$

$$\mathcal{L}_{ML}(\mathbf{z}) = \ln \det \mathbf{C}_x(\mathbf{z}) + \text{Tr}\left(\hat{\mathbf{R}}_x \mathbf{C}_x^{-1}(\mathbf{z})\right) \quad (3.22)$$

and find $\hat{\mathbf{z}}$ that yields the smallest value of (3.22).

It is evident that the length of \mathbf{z} determines the computational complexity of the problem. Without looking into details, it can be assumed that the complexity varies by orders of magnitude, when compared with MUSIC or ESPRIT.

An example of a log-likelihood function graph is shown on Figure 3.3. Note that signal power σ_0^2 and noise powers σ_n^2 have been fixed in this example. In practical settings, one also needs to estimate those. Generally, it means that having signals from L sources aggregated into $\mathbf{x}(t)$, the problem is $2L + 1$ dimensional.

3.3.2. Maximum A Posteriori Estimator

The Maximum A Posteriori (MAP) estimator is the Bayesian counterpart to ML in classical estimation theory. When ML is seeking to find the mode of data likelihood function, then MAP seeks to find a mode of the posteriori PDF. Latter includes prior knowledge about the unknown parameter in addition to the data likelihood obtained from the observations. The fundamental difference between the classical and Bayesian estimation theory lies in how the unknown parameter is viewed. In the former, the parameter of interest (in this case signal DOA) is viewed as a deterministic opposed to Bayesian approach, where the parameter is considered to be random. Inherently, the Bayesian philosophy is more applicable estimating a direction of a mobile device. Indeed, one can hardly consider the movement of a person using a smartphone, car navigating through the city or an aircraft flying from London to Tokyo deterministic.

The well known Bayesian theorem states

$$p(\mathbf{z}|\mathbf{x}_t) = \frac{p(\mathbf{z})p(\mathbf{x}_t|\mathbf{z})}{p(\mathbf{x}_t)}, \quad (3.23)$$

where $p(\mathbf{z})$ is prior PDF, $p(\mathbf{x}_t)$ is the marginal likelihood and $p(\mathbf{x}_t|\mathbf{z})$ is data likelihood. Latter is defined the same way as in Section 3.3.1, the array signal vector \mathbf{x}_t is Gaussian. In MAP, the marginal likelihood is discarded as it does not depend on \mathbf{z} .

The prior PDF $p(\mathbf{z})$ is

$$p(\mathbf{z}) = p(\mathbf{u})p(\boldsymbol{\sigma}^2)p(\sigma_n^2). \quad (3.24)$$

Obviously one can hardly argue that there is universally any reason to favour one prior PDF over another. But *if* we have one target ($L = 1$) with its location distributed normally around some known value \bar{u}_0 and with known variance $\sigma_{\bar{u}_0}^2$ i.e.

$$u_0 \sim \mathcal{N}(\bar{u}_0, \sigma_{\bar{u}_0}^2), \quad (3.25)$$

and we use non-informative priors for $p(\sigma_0^2) = 1$ and $p(\sigma_n^2) = 1$ it can be shown that log posteriori PDF function is

$$\mathcal{L}(\mathbf{z}) = \frac{1}{\sigma_{\bar{u}_0}^2}(u - \bar{u}_0)^2 + \text{Tr}\left(\hat{\mathbf{R}}_{\mathbf{x}}\mathbf{C}_{\mathbf{x}}^{-1}(\mathbf{z})\right) \quad (3.26)$$

The task, of course, is to find a minima of this function. An example log posterior PDF for such case is shown on Figure. 3.4.

More through treatment of Bayesian DOA estimator and its potential practical use cases is given in paper presented in Appendix C.

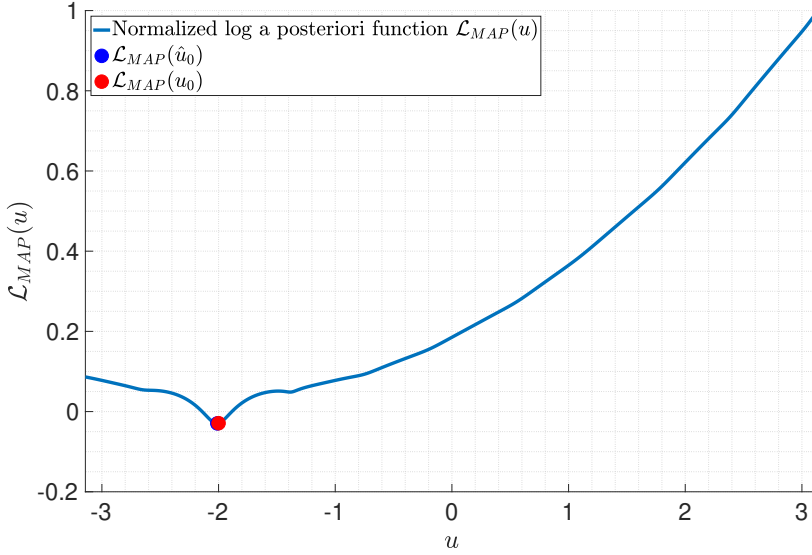


Figure 3.4 An example of a log posteriori PDF function

3.4. Performance Comparison

In this section we will compare the performance of the DOA estimation methods described in the chapter. We will examine two aspects of the algorithm performance. First, the DOA estimation accuracy dependence on the SNR and second, the dependence on angular distance between the signal sources, we will entitle them *noise trial* and *resolution trial* respectively. The simulation setup parameters have been given in Table 3.1. In both simulation trials we assume that the signal power σ_s^2 and noise power σ_n^2 is known and the algorithm's task is only to estimate DOAs of the arriving signals.

The performance of an DOA estimation algorithm is quantified and visualised using MSE, which in current chapter is given by

$$\epsilon = E[(\mathbf{u} - \hat{\mathbf{u}})^T(\mathbf{u} - \hat{\mathbf{u}})]. \quad (3.27)$$

The symbol $\hat{\mathbf{u}}$ indicates the estimated DOA value, whereas the variable without the "hat" symbol indicates true DOA.

The results of the *noise trial* are shown on Figure 3.5. Let us start by examining the performance of MAP estimators. There are two aspects that are important, first, the DOA estimation accuracy is rather stable over the range of SNR-s and second, the importance of the variance of the *a priori* PDF has on the estimator performance. These observations are in line with the intuition: prior knowledge will not allow estimators to make huge mistakes and the accurate prior knowledge about something will allow us to make better predictions about its true behaviour. While in some cases prior knowledge might work against us -

Table 3.1 DOA estimation algorithms comparison trial setup.

Parameter	Value
Array model	ULA
Array size	$M = 10$
Number of signal sources	$L = 2$
Number of signal snapshots	$T = 10$
SNR	noise trial : $\eta = -13 \text{ dB}, \dots, 10 \text{ dB}$ resolution trial : $\eta = 0 \text{ dB}$
Angular distance between targets	noise trial : $ \theta_1 - \theta_2 = 0.5 \text{ rad}$ resolution trial : $ \theta_1 - \theta_2 = 0.1 \text{ rad}, \dots, 1 \text{ rad}$
Monte Carlo iterations	1000

presumptions about something will not allow us to see something that is simply observable (in current case more accurate DOA in good SNR cases).

When looking at other algorithms, ML (red on the figure) algorithm outperforms others. It is clearly seen that in case of modes SNR ($\eta < 5 \text{ dB}$), MUSIC (violet) algorithm suffers dramatically from having a rather inaccurate covariance matrix \mathbf{R}_x resulting from having small number of signal samples ($T = 10$). The same applies for beamforming based DOA estimation algorithm (blue), the poor array covariance matrix estimates results make the algorithm virtually unusable. Seems that in the given conditions ESPRIT (yellow on the figure) achieves good balance between the algorithm complexity and estimation accuracy.

In conclusion, if one seeks stable estimation performance over a wider range of SNR or in poor SNR conditions MAP estimator should be favored (that is, when one has prior knowledge about the source location). If the application is deployed in the good SNR setting, one might consider other algorithms. Although ML generally outperforms others, the balance point between the complexity and performance will determine the most favourable algorithm.

On Figure 3.6 signal source resolution capabilities of different DOA estimation algorithms are examined.

MAP algorithm clearly outperforms other algorithms, retaining more or less stable MSE over the across angular distance range. Same could be said about the performance of ML estimator, but there is a 2 to 4 dB MSE difference compared with MAP and subtle decrease in performance with decreasing angular distance.

MUSIC and ESPRIT algorithms performance start degrading around the same angular distance. When comparing the degradation rate of the two, one notices that it is much steeper for MUSIC. DOA estimation MSE of the beamforming based DOA estimation is performing at a level, where it is unusable in practical

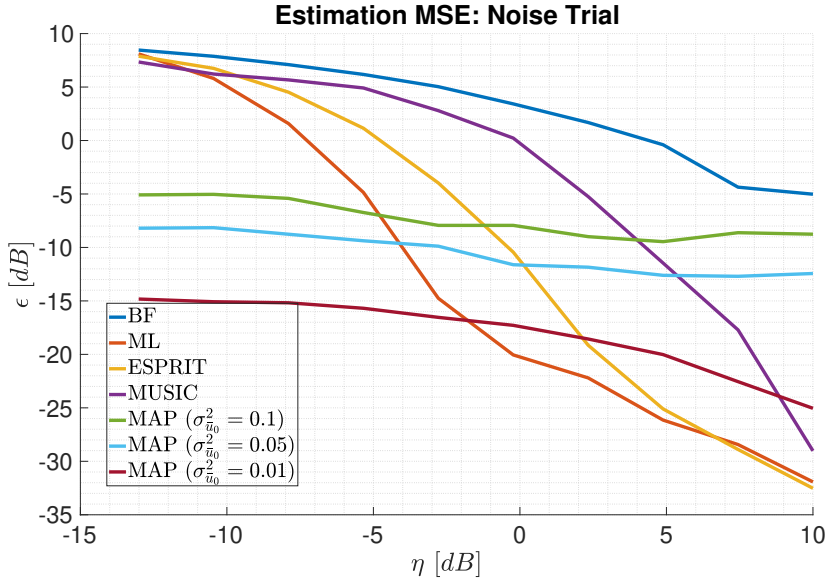


Figure 3.5 DOA estimate MSE for different algorithms.

settings. It is caused by the small number of signal snapshots used for calculating array covariance matrix \mathbf{R}_x .

The high MSE fluctuations in ML from one data point to another are caused by small signal block size T , when calculating covariance matrix. It seems not have major effect to other algorithms in that respect.

3.5. Chapter Summary

In this chapter, some of the commonly used DOA estimation algorithms were presented. The authors contributions to the field were omitted and were presented in the [Appendix C].

The DOA estimation methods discussed in the thesis were divided into three groups: *beamforming methods*, *subspace based methods* and *parametric methods*.

The general consensus is (and it was illustrated in current chapter), that although *parametric methods* perform better in terms of achievable estimation MSE, *subspace based methods* and *beamforming methods* are considerably less complex and should be implemented in favourable SNR and target angular resolution situations.

To achieve more consistent performance over a wider range of the SNR-s and the signal source angular distances, one could make use of prior knowledge about the target's predicted location. This approach is discussed in detail in the [Appendix C].

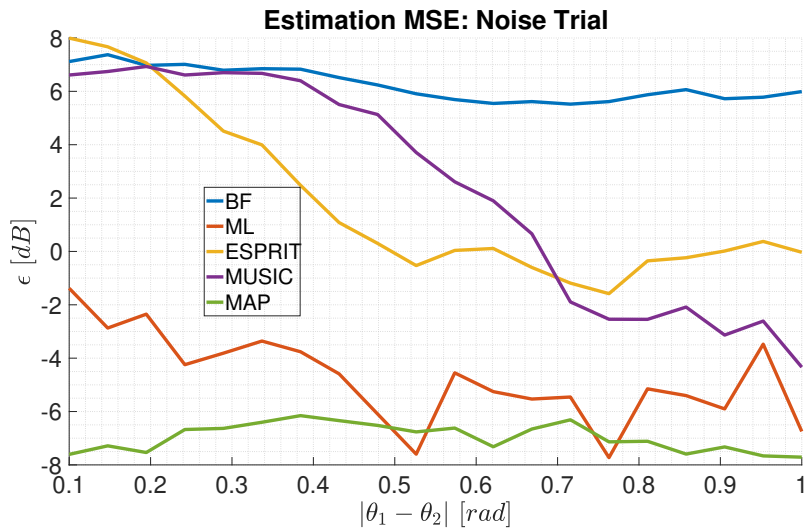


Figure 3.6 DOA estimate MSE for different signal source angular distances.

CONCLUSIONS

As array processing algorithms are key enablers in the future communication systems, it continues to be in the focus of the research community. In this thesis two main areas of the array processing: *beamforming* and *DOA estimation* were discussed.

The task of beamforming is to ensure sufficient SINR ratio in the receiver by employing means of spatial filtering. In broad terms beamformers can be divided into two categories: *data independent* and *data dependent*. Former specifies the desired array response to a signals travelling to/from some arbitrary direction. Latter chooses the array weights based on some signal statistics. Generally, while having higher computational complexity, the *data independent* achieves better interference suppression, when compared with the *data independent* beamformers.

Obviously some knowledge about the signal and signal source (e.g. DOA) is required in either case and inevitably there are mismatches between our knowledge and the actual situation. Even if nothing else, mobile devices cause some level of uncertainty in the DOA by just moving around. The mismatches, in turn, will cause beamformer performance degradation and the *data dependent* beamformers are more sensitive to these imperfections. Thankfully there are methods to avoid the issue. Usually, the uncertainty region around the expected DOA is specified, where signal suppression will be forbidden.

Work presented in the [Appendix A] and the [Appendix B] address the issue in the two dimensional arrays by utilising Slepian sequences to define the uncertainty region. Slepian sequences are well known for their ability to maximise the energy in specified (spatio-)spectral regions. The proposed beamformers are revealed as Generalized Sidelobe Cancellers (GSC) and use Slepian sequences with good energy concentration capabilities both in the steering and the blocking branch. The difference between the work presented in [Appendix A] and [Appendix B] is the shape of the uncertainty area: in former it is a rectangular and in latter, a disc. In both papers it has been shown, using numerical simulations, that the proposed approaches outperform traditional GSC.

The task of DOA estimation is accurately determine the arrival angle of the signal. It is generally acknowledged and was also shown in the thesis, that the parametric methods (e.g. Maximum Likelihood) have acceptable performance over the wider range of SNRs and the angular distances between the signal sources when compared with the subspace and the beamforming based

estimation methods. But, inevitably, there is a point, where ML estimation accuracy degrades sharply. Work presented in the [Appendix C] proposes a Maximum A Posteriori (MAP) estimator to increase the span of SNRs, where estimation accuracy is on acceptable level. In order to achieve it, signal source knowledge about its predicted position is used to achieve better consistency in the DOA estimation. The numerical simulations showed that in the case of large array covariance matrix mismatches, the MAP based approach significantly outperformed the ML and the MUSIC algorithms.

Future Work

The work presented in the appendices allow several directions to extend the work. In the following list are some of aspects that might be worthy of future study. By no means we consider the list to be exhaustive.

1. In [Appendix A] and [Appendix B] the uncertainty areas have been defined as a rectangle and a disc. In a complex scatter rich environment, however, one wants to define an arbitrary shaped beampattern with possible multiple peaks in different directions. This would allow it to utilise the full benefits of MIMO. Slepian sequences do allow that. One can expect that there will not be a closed form solution meaning extra care must be taken to control the computational complexity of the algorithm.
2. Work reported in [Appendix C] suggests that if the array covariance mismatch is large and the number of array elements is small, MAP estimator does provide consistent DOA estimation accuracy. As multi-channel coherent software defined radios are getting more affordable¹ the proposed estimator could be used in low cost ADS-B sensor. Incorporating these in crowd sourcing networks² would decrease the computation effort on the server side and increase the quality of gathered data.
3. In the MIMO system arguably one the most difficult tasks is to estimate the channel matrix containing the channel gains between transmit/receive antenna pairs. Work presented in [Appendix C] could be used to decrease the required effort and increase the channel matrix estimation accuracy.

¹E.g.: <https://othernet.is/products/kerberosdr-4x-coherent-rtl-sdr>

²E.g.: <https://opensky-network.org/>

REFERENCES

- [1] T. Trump, “A robust adaptive sensor array with slepian sequences,” in *2012 IEEE 7th Sensor Array and Multichannel Signal Processing Workshop (SAM)*, 2012, pp. 121–124.
- [2] O. L. Frost, “An algorithm for linearly constrained adaptive array processing,” *Proceedings of the IEEE*, vol. 60, no. 8, pp. 926–935, 1972.
- [3] R. O. Schmidt, “A signal subspace approach to multiple emitter location and spectral estimation.” Ph.D. dissertation, Stanford University, 1982.
- [4] (2020) Ericsson mobility report. Ericsson. [Online]. Available: <https://www.ericsson.com/4adc87/assets/local/mobility-report/documents/2020/november-2020-ericsson-mobility-report.pdf>
- [5] Z. Pi and F. Khan, “An introduction to millimeter-wave mobile broadband systems,” *IEEE Communications Magazine*, vol. 49, no. 6, pp. 101–107, 2011.
- [6] F. Boccardi, R. W. Heath, A. Lozano, T. L. Marzetta, and P. Popovski, “Five disruptive technology directions for 5g,” *IEEE Communications Magazine*, vol. 52, no. 2, pp. 74–80, 2014.
- [7] T. S. Rappaport, S. Sun, R. Mayzus, H. Zhao, Y. Azar, K. Wang, G. N. Wong, J. K. Schulz, M. Samimi, and F. Gutierrez, “Millimeter wave mobile communications for 5g cellular: It will work!” *IEEE Access*, vol. 1, pp. 335–349, 2013.
- [8] Wired Magazine, “The wired guide to 5g,” September 2020. [Online]. Available: <https://www.wired.com/story/wired-guide-5g/>
- [9] M. Giordani, M. Polese, A. Roy, D. Castor, and M. Zorzi, “A tutorial on beam management for 3gpp nr at mmwave frequencies,” *IEEE Communications Surveys Tutorials*, vol. 21, no. 1, pp. 173–196, 2019.
- [10] F. Rusek, D. Persson, B. K. Lau, E. G. Larsson, T. L. Marzetta, O. Edfors, and F. Tufvesson, “Scaling up mimo: Opportunities and challenges with very large arrays,” *IEEE Signal Processing Magazine*, vol. 30, no. 1, pp. 40–60, 2013.

- [11] E. G. Larsson, O. Edfors, F. Tufvesson, and T. L. Marzetta, “Massive mimo for next generation wireless systems,” *IEEE Communications Magazine*, vol. 52, no. 2, pp. 186–195, 2014.
- [12] G. Caire, N. Jindal, M. Kobayashi, and N. Ravindran, “Multiuser mimo achievable rates with downlink training and channel state feedback,” *IEEE Transactions on Information Theory*, vol. 56, no. 6, pp. 2845–2866, 2010.
- [13] A. Yang, Y. Jing, C. Xing, Z. Fei, and J. Kuang, “Performance analysis and location optimization for massive mimo systems with circularly distributed antennas,” *IEEE Transactions on Wireless Communications*, vol. 14, no. 10, pp. 5659–5671, 2015.
- [14] A. Puglielli, A. Townley, G. LaCaille, V. Milovanović, P. Lu, K. Trotskovsky, A. Whitcombe, N. Narevsky, G. Wright, T. Courtade, E. Alon, B. Nikolić, and A. M. Niknejad, “Design of energy- and cost-efficient massive mimo arrays,” *Proceedings of the IEEE*, vol. 104, no. 3, pp. 586–606, 2016.
- [15] M. Wang, F. Gao, S. Jin, and H. Lin, “An overview of enhanced massive mimo with array signal processing techniques,” *IEEE Journal of Selected Topics in Signal Processing*, vol. 13, no. 5, pp. 886–901, 2019.
- [16] J. Edwards, “Signal processing inspires network innovation: Signal processing is the key as researchers work to boost network speed and capacity [special reports],” *IEEE Signal Processing Magazine*, vol. 37, no. 1, pp. 16–23, 2020.
- [17] W. Saad, M. Bennis, and M. Chen, “A vision of 6g wireless systems: Applications, trends, technologies, and open research problems,” *IEEE Network*, vol. 34, no. 3, pp. 134–142, 2020.
- [18] M. Giordani, M. Polese, M. Mezzavilla, S. Rangan, and M. Zorzi, “Toward 6g networks: Use cases and technologies,” *IEEE Communications Magazine*, vol. 58, no. 3, pp. 55–61, 2020.
- [19] E. Calvanese Strinati, S. Barbarossa, J. L. Gonzalez-Jimenez, D. Ktenas, N. Cassiau, L. Maret, and C. Dehos, “6g: The next frontier: From holographic messaging to artificial intelligence using subterahertz and visible light communication,” *IEEE Vehicular Technology Magazine*, vol. 14, no. 3, pp. 42–50, 2019.
- [20] D. Tse and P. Viswanath, *Fundamentals of wireless communication*. Cambridge university press, 2005.
- [21] M. C. Stevens, *Secondary surveillance radar*. Artech House on Demand, 1988.

- [22] S. Kingsley and S. Quegan, *Understanding radar systems*. SciTech Publishing, 1999, vol. 2.
- [23] N. Petrochilos, G. Galati, and E. Piracci, “Array processing of SSR signals in the multilateration context, a decade survey,” in *2008 Tyrrhenian International Workshop on Digital Communications - Enhanced Surveillance of Aircraft and Vehicles*, 2008, pp. 1–5.
- [24] *ICAO Annex 10 - Aeronautical Telecommunications - Volume IV - Surveillance Radar and Collision Avoidance Systems*, 5th ed., International Civil Aviation Organisation, 2014.
- [25] E. Chang, R. Hu, D. Lai, R. Li, Q. Scott, and T. Tyan, “The story of mode S: An air traffic control data-link technology,” *Cambridge, MA: Massachusetts Institute of Technology*, vol. 15, 2000. [Online]. Available: <http://web.mit.edu/6.933/www/Fall2000/mode-s/index.html>
- [26] X. Olive, A. Tanner, M. Strohmeier, M. Schäfer, M. Feridun, A. Tart, I. Martinovic, and V. Lenders, “Opensky report 2020: Analysing in-flight emergencies using big data,” in *2020 AIAA/IEEE 39th Digital Avionics Systems Conference (DASC)*, 2020, pp. 1–10.
- [27] Eurocontrol, “European aviation in 2040: Challenges of growth. annex1: Flight forecast to 2040,” 2018. [Online]. Available: https://www.eurocontrol.int/sites/default/files/2019-07/challenges-of-growth-2018-annex1_0.pdf
- [28] Eurocontrol, “Eurocontrol five-year forecast 2020-2024 european flight movements and service units three scenarios for recovery from covid-19,” 2020. [Online]. Available: <https://www.eurocontrol.int/sites/default/files/2020-11/eurocontrol-five-year-forecast-europe-2020-2024.pdf>
- [29] M. Strohmeier, M. Schäfer, V. Lenders, and I. Martinovic, “Realities and challenges of nextgen air traffic management: the case of ADS-B,” *IEEE Communications Magazine*, vol. 52, no. 5, pp. 111–118, 2014.
- [30] R. E. Boisvert and V. A. Orlando, “ADS-mode S system overview,” in *[1993 Proceedings] AIAA/IEEE Digital Avionics Systems Conference*, 1993, pp. 104–109.
- [31] A. Costin and A. Francillon, “Ghost in the air (traffic): On insecurity of ADS-B protocol and practical attacks on ADS-B devices,” *black hat USA*, pp. 1–12, 2012. [Online]. Available: https://www.researchgate.net/publication/267557712_Ghost_in_the_AirTraffic_On_insecurity_of_ADS-B_protocol_and_practical_attacks_on_ADS-B_devices

- [32] D. McCallie, J. Butts, and R. Mills, "Security analysis of the ads-b implementation in the next generation air transportation system," *International Journal of Critical Infrastructure Protection*, vol. 4, no. 2, pp. 78–87, 2011.
- [33] M. Leonardi, E. Piracci, and G. Galati, "Ads-b vulnerability to low cost jammers: Risk assessment and possible solutions," in *2014 Tyrrhenian International Workshop on Digital Communications - Enhanced Surveillance of Aircraft and Vehicles (TIWDC/ESAV)*, 2014, pp. 41–46.
- [34] L. Purton, H. Abbass, and S. Alam, "Identification of ads-b system vulnerabilities and threats," in *Australian Transport Research Forum, Canberra*, 2010, pp. 1–16. [Online]. Available: https://www.researchgate.net/publication/267957938_Identification_of_ADS-B_System_Vulnerabilities_and_Threats
- [35] A. D. Zeitlin and R. C. Strain, "Augmenting ads-b with traffic information service-broadcast," in *Proceedings. The 21st Digital Avionics Systems Conference*, vol. 1, 2002, pp. 3D2–3D2.
- [36] Inkyu Kim, "The ads-b operational test using vdl mode 4 and uat surveillance data," in *2007 IEEE/AIAA 26th Digital Avionics Systems Conference*, 2007, pp. 4.D.5–1–4.D.5–1.
- [37] V. A. Orlando, G. H. Knittel, and R. E. Boisvert, "Gps-squitter: system concept, performance, and development program," *The Lincoln Laboratory Journal*, vol. 7, no. 2, pp. 271–294, 1994. [Online]. Available: <http://citeseerx.ist.psu.edu/viewdoc/download?doi=10.1.1.229.2612&rep=rep1&type=pdf>
- [38] Council of European Union, "Commission implementing regulation (eu) no 1207/2011," 2011. [Online]. Available: <https://eur-lex.europa.eu/legal-content/EN/TXT/?uri=CELEX%3A32011R1207>
- [39] European Union Aviation Safety Agency, "Acceptable means of compliance and guidance material to commission implementing regulation (eu) no 1207/2011," 2020. [Online]. Available: https://www.easa.europa.eu/sites/default/files/dfu/annex_to_ed_decision_2020-014-r.pdf
- [40] P. Park and C. Tomlin, "Performance evaluation and optimization of communication infrastructure for the next generation air transportation system," *IEEE Transactions on Parallel and Distributed Systems*, vol. 26, no. 4, pp. 1106–1116, 2015.
- [41] G. Jacovitti, "Performance analysis of monopulse receivers for secondary surveillance radar," *IEEE Transactions on Aerospace and Electronic Systems*, vol. AES-19, no. 6, pp. 884–897, 1983.

- [42] J. Tol and P. van Genderen, "Ssr reply separation using array signal processing methods," in *Radar 97 (Conf. Publ. No. 449)*, 1997, pp. 793–796.
- [43] A. van der Veen and J. Tol, "Separation of zero/constant modulus signals," in *1997 IEEE International Conference on Acoustics, Speech, and Signal Processing*, vol. 5, 1997, pp. 3445–3448 vol.5.
- [44] N. Petrochilos and A. van der Veen, "Algebraic algorithms to separate overlapping secondary surveillance radar replies," *IEEE Transactions on Signal Processing*, vol. 55, no. 7, pp. 3746–3759, 2007.
- [45] M. Leonardi, E. Piracci, and G. Galati, "Ads-b jamming mitigation: a solution based on a multichannel receiver," *IEEE Aerospace and Electronic Systems Magazine*, vol. 32, no. 11, pp. 44–51, 2017.
- [46] Y. A. Nijssure, G. Kaddoum, G. Gagnon, F. Gagnon, C. Yuen, and R. Mahapatra, "Adaptive air-to-ground secure communication system based on ads-b and wide-area multilateration," *IEEE Transactions on Vehicular Technology*, vol. 65, no. 5, pp. 3150–3165, 2016.
- [47] W. Wang, R. Wu, and J. Liang, "Ads-b signal separation based on blind adaptive beamforming," *IEEE Transactions on Vehicular Technology*, vol. 68, no. 7, pp. 6547–6556, 2019.
- [48] C. Reck, M. S. Reuther, A. Jasch, and L. . Schmidt, "Independent surveillance broadcast — ads-b receivers with doa estimation," in *2011 Tyrrhenian International Workshop on Digital Communications - Enhanced Surveillance of Aircraft and Vehicles*, 2011, pp. 219–222.
- [49] J. Naganawa, H. Tajima, H. Miyazaki, T. Koga, and C. Chomel, "Ads-b anti-spoofing performance of monopulse technique with sector antennas," in *2017 IEEE Conference on Antenna Measurements Applications (CAMA)*, 2017, pp. 87–90.
- [50] C. Reck, U. Berold, and L. . Schmidt, "High precision doa estimation of ssr transponder signals," in *2010 IEEE International Conference on Wireless Information Technology and Systems*, 2010, pp. 1–4.
- [51] A. Sipe and J. Moore, "Air traffic functions in the nextgen and sesar airspace," in *2009 IEEE/AIAA 28th Digital Avionics Systems Conference*, 2009, pp. 2.A.6–1–2.A.6–7.
- [52] N. Peinecke and A. Kuenz, "Deconflicting the urban drone airspace," in *2017 IEEE/AIAA 36th Digital Avionics Systems Conference (DASC)*, 2017, pp. 1–6.

- [53] P. Kopardekar, *Unmanned aerial system (UAS) traffic management (UTM): Enabling low-altitude airspace and UAS operations*. National Aeronautics and Space Administration, Ames Research Center, 2014. [Online]. Available: <https://ntrs.nasa.gov/api/citations/20140013436/downloads/20140013436.pdf>
- [54] S. J. Undertaking, *European drones outlook study. Unlocking the value for Europe*. Publications Office of the EU, 2016. [Online]. Available: <https://op.europa.eu/en/publication-detail/-/publication/93d90664-28b3-11e7-ab65-01aa75ed71a1>
- [55] M. J. Marcus, “5g/weather satellite 24 ghz spectrum disagreement: Anatomy of a spectrum policy issue,” *IEEE Wireless Communications*, vol. 26, no. 4, pp. 2–3, 2019.
- [56] P. Kasemir, N. Sutton, M. Radway, B. Jeong, T. Brown, and D. S. Filipovič, “Wideband analog and digital beamforming,” in *2009 9th International Conference on Telecommunication in Modern Satellite, Cable, and Broadcasting Services*, 2009, pp. 372–375.
- [57] H. Asplund, D. Astely, P. von Butovitsch, T. Chapman, M. Frenne, F. Ghasemzadeh, M. Hagström, B. Hogan, G. Jöngren, J. Karlsson *et al.*, *Advanced Antenna Systems for 5G Network Deployments: Bridging the Gap Between Theory and Practice*. Academic Press, 2020.
- [58] X. Huang, Y. J. Guo, and J. D. Bunton, “A hybrid adaptive antenna array,” *IEEE Transactions on Wireless Communications*, vol. 9, no. 5, pp. 1770–1779, 2010.
- [59] S. Chuang, W. Wu, and Y. Liu, “High-resolution aoa estimation for hybrid antenna arrays,” *IEEE Transactions on Antennas and Propagation*, vol. 63, no. 7, pp. 2955–2968, 2015.
- [60] F. Sohrabi and W. Yu, “Hybrid digital and analog beamforming design for large-scale antenna arrays,” *IEEE Journal of Selected Topics in Signal Processing*, vol. 10, no. 3, pp. 501–513, 2016.
- [61] N. Garcia, H. Wymeersch, E. G. Ström, and D. Slock, “Location-aided mm-wave channel estimation for vehicular communication,” in *2016 IEEE 17th International Workshop on Signal Processing Advances in Wireless Communications (SPAWC)*, 2016, pp. 1–5.
- [62] A. Shahmansoori, G. E. Garcia, G. Destino, G. Seco-Granados, and H. Wymeersch, “Position and orientation estimation through millimeter-wave mimo in 5g systems,” *IEEE Transactions on Wireless Communications*, vol. 17, no. 3, pp. 1822–1835, 2018.

- [63] Z. Ni, J. A. Zhang, K. Yang, F. Gao, and J. An, "Estimation of multiple angle-of-arrivals with localized hybrid subarrays for millimeter wave systems," *IEEE Transactions on Communications*, vol. 68, no. 3, pp. 1897–1910, 2020.
- [64] M. S. Sim, Y. Lim, S. H. Park, L. Dai, and C. Chae, "Deep learning-based mmwave beam selection for 5g nr/6g with sub-6 ghz channel information: Algorithms and prototype validation," *IEEE Access*, vol. 8, pp. 51 634–51 646, 2020.
- [65] H. Jafarkhani, *Space-time coding: theory and practice*. Cambridge university press, 2005.
- [66] Q. H. Spencer, A. L. Swindlehurst, and M. Haardt, "Zero-forcing methods for downlink spatial multiplexing in multiuser mimo channels," *IEEE Transactions on Signal Processing*, vol. 52, no. 2, pp. 461–471, 2004.
- [67] L. Jiang and H. Jafarkhani, "Multi-user analog beamforming in millimeter wave mimo systems based on path angle information," *IEEE Transactions on Wireless Communications*, vol. 18, no. 1, pp. 608–619, 2019.
- [68] A. Alkhateeb, O. El Ayach, G. Leus, and R. W. Heath, "Hybrid precoding for millimeter wave cellular systems with partial channel knowledge," in *2013 Information Theory and Applications Workshop (ITA)*, 2013, pp. 1–5.
- [69] O. E. Ayach, S. Rajagopal, S. Abu-Surra, Z. Pi, and R. W. Heath, "Spatially sparse precoding in millimeter wave mimo systems," *IEEE Transactions on Wireless Communications*, vol. 13, no. 3, pp. 1499–1513, 2014.
- [70] S. Han, C. I. Z. Xu, and C. Rowell, "Large-scale antenna systems with hybrid analog and digital beamforming for millimeter wave 5g," *IEEE Communications Magazine*, vol. 53, no. 1, pp. 186–194, 2015.
- [71] W. Roh, J. Seol, J. Park, B. Lee, J. Lee, Y. Kim, J. Cho, K. Cheun, and F. Aryanfar, "Millimeter-wave beamforming as an enabling technology for 5g cellular communications: theoretical feasibility and prototype results," *IEEE Communications Magazine*, vol. 52, no. 2, pp. 106–113, 2014.
- [72] M. Bengtsson and B. Ottersten, *Optimal and suboptimal transmit beamforming*. CRC press, 2001.
- [73] D. Gesbert, M. Kountouris, R. W. Heath, C. Chae, and T. Salzer, "Shifting the mimo paradigm," *IEEE Signal Processing Magazine*, vol. 24, no. 5, pp. 36–46, 2007.
- [74] A. Alkhateeb, J. Mo, N. Gonzalez-Prelcic, and R. W. Heath, "Mimo precoding and combining solutions for millimeter-wave systems," *IEEE Communications Magazine*, vol. 52, no. 12, pp. 122–131, 2014.

- [75] F. Rashid-Farrokhi, K. J. R. Liu, and L. Tassiulas, "Transmit beamforming and power control for cellular wireless systems," *IEEE Journal on Selected Areas in Communications*, vol. 16, no. 8, pp. 1437–1450, 1998.
- [76] C. Farsakh and J. A. Nossek, "Spatial covariance based downlink beamforming in an sdma mobile radio system," *IEEE Transactions on Communications*, vol. 46, no. 11, pp. 1497–1506, 1998.
- [77] A. B. Gershman, N. D. Sidiropoulos, S. Shahbazpanahi, M. Bengtsson, and B. Ottersten, "Convex optimization-based beamforming," *IEEE Signal Processing Magazine*, vol. 27, no. 3, pp. 62–75, 2010.
- [78] B. D. Van Veen and K. M. Buckley, "Beamforming: a versatile approach to spatial filtering," *IEEE ASSP Magazine*, vol. 5, no. 2, pp. 4–24, 1988.
- [79] H. L. Van Trees, *Optimum array processing: Part IV of detection, estimation, and modulation theory*. John Wiley & Sons, 2004.
- [80] S. S. Haykin, *Adaptive filter theory*. Pearson Education Limited, 2005.
- [81] L. Griffiths and C. Jim, "An alternative approach to linearly constrained adaptive beamforming," *IEEE Transactions on Antennas and Propagation*, vol. 30, no. 1, pp. 27–34, 1982.
- [82] H. L. Van Trees, *Optimum array processing: Part IV of detection, estimation, and modulation theory*. John Wiley & Sons, 2004.
- [83] J. Li and P. Stoica, *Robust adaptive beamforming*. Wiley Online Library, 2006.
- [84] P. Stoica, R. L. Moses *et al.*, *Spectral analysis of signals*. Pearson Prentice Hall Upper Saddle River, NJ, 2005.
- [85] J. R. Guerci, "Theory and application of covariance matrix tapers for robust adaptive beamforming," *IEEE Transactions on Signal Processing*, vol. 47, no. 4, pp. 977–985, 1999.
- [86] Huixia He and S. Kraut, "A partially adaptive beamforming with slepian-based quiescent response," in *IEEE/SP 13th Workshop on Statistical Signal Processing, 2005*, 2005, pp. 301–306.
- [87] H. Krim and M. Viberg, "Two decades of array signal processing research: the parametric approach," *IEEE Signal Processing Magazine*, vol. 13, no. 4, pp. 67–94, 1996.
- [88] A. H. Sayed, A. Tarighat, and N. Khajehnouri, "Network-based wireless location: challenges faced in developing techniques for accurate wireless location information," *IEEE Signal Processing Magazine*, vol. 22, no. 4, pp. 24–40, 2005.

- [89] C. Vasanelli, F. Roos, A. Dürr, J. Schlichenmaier, P. Hügler, B. Meinecke, M. Steiner, and C. Waldschmidt, “Calibration and direction-of-arrival estimation of millimeter-wave radars: A practical introduction,” *IEEE Antennas and Propagation Magazine*, pp. 0–0, 2020.
- [90] S. Chandran, *Advances in direction-of-arrival estimation*. Artech House Boston, 2006.
- [91] P.-J. Chung, M. Viberg, and J. Yu, “Chapter 14 - doa estimation methods and algorithms,” in *Academic Press Library in Signal Processing: Volume 3*, ser. Academic Press Library in Signal Processing, A. M. Zoubir, M. Viberg, R. Chellappa, and S. Theodoridis, Eds. Elsevier, 2014, vol. 3, pp. 599 – 650. [Online]. Available: <http://www.sciencedirect.com/science/article/pii/B978012411597200014X>
- [92] R. F. SC-186, *Minimum Operational Performance Standards (MOPS) for 1090 MHz Extended Squitter Automatic Dependent Surveillance-Broadcast (ADS-B) and Traffic Information Services-Broadcast (TIS-B)*. RTCA, Incorporated, 2011.
- [93] O. de l’aviation civile internationale, *Advanced Surface Movement Guidance and Control Systems (A-SMGCS) Manual*. ICAO, 2004.
- [94] M. Schafer, M. Strohmeier, M. Smith, M. Fuchs, R. Pinheiro, V. Lenders, and I. Martinovic, “Opensky report 2016: Facts and figures on sdr mode s and ads-b usage,” in *2016 IEEE/AIAA 35th Digital Avionics Systems Conference (DASC)*, 2016, pp. 1–9.
- [95] J. Chen and A. Abedi, “A hybrid framework for radio localization in broadband wireless systems,” in *2010 IEEE Global Telecommunications Conference GLOBECOM 2010*, 2010, pp. 1–6.
- [96] T. Sanchez, R. C. Hincapie, and C. Gomez, “Performance study of localization techniques: hybrid vs. non hybrid tdoa/doa,” in *2018 IEEE-APS Topical Conference on Antennas and Propagation in Wireless Communications (APWC)*, 2018, pp. 957–960.
- [97] G. Bienvenu and L. Kopp, “Adaptivity to background noise spatial coherence for high resolution passive methods,” in *ICASSP ’80. IEEE International Conference on Acoustics, Speech, and Signal Processing*, vol. 5, 1980, pp. 307–310.
- [98] A. Paulraj, R. Roy, and T. Kailath, “A subspace rotation approach to signal parameter estimation,” *Proceedings of the IEEE*, vol. 74, no. 7, pp. 1044–1046, 1986.
- [99] S. M. Kay, *Fundamentals of statistical signal processing, Volume I: Estimation Theory*. Prentice Hall PTR, 2015, vol. 1.

ABSTRACT

Some Novel Algorithms for Processing Sensor Array Output Signals

Array processing is still very much in the focus of the research community as its methods are the key enablers for achieving the objectives of modern communication systems. As an example two use cases can be looked at.

Firstly, the 5G networks, that by the year of 2026 must be able to serve up to 45GB per month smartphone subscriptions. A point worth noting is that the number given does not include other types of services such as Fixed Wireless Access (a service providing internet connection to households), IoT and automotive related services and so on. One can imagine the aggregated capacity and throughput required from the 5G network will be enormous by today's standards. General consensus is that to satisfy these requirements space division multiplexing (SDM) together with frequency and time domain multiplexing must be employed. The SDM is achievable only if the transceiver is able to transmit/receive signal to/from desired direction meaning that effective and efficient beamforming methods are needed. On the other hand, in order to steer the antenna main beam to the right direction, one must know where the desired direction is. Meaning that consistently accurate DOA estimation algorithms are needed. In turn, the beamforming must allow some level of mismatch between the estimated and actual DOA.

As a second example let us take a look at modern air surveillance systems. The system is divided into layers, each layer containing one air surveillance technology. Usually the layers are set in orderly fashion, where the bottom layers are more essential than the upper layers. Two of the bottom layer air surveillance technologies (namely ADS-B and SSR [Mode S]) use the same communication system that utilises only one 1090MHz narrow band channel. With ever increasing air traffic growth and with new actors (e.g. drones) coming into play, the channel is about to reach its capacity limit. Lack of security measures which with relatively small effort allows to halt the system is also adding to the already considerable list of problems. Again, array processing can be used to mitigate most of the concerns. Beamforming does allow spatial filtering to increase the 1090Mhz channel capacity whereas efficient DOA estimation algorithms help to determine the desired direction.

The thesis provides an overview about the beamforming and DOA estimation algorithms most commonly used today.

In the chapter dedicated to beamforming *data independent* and *data dependent* beamforming algorithms are described. Former specifies desired array response to signals travelling to/from some arbitrary direction. Latter chooses array weights based on some signal statistics. Generally, while having higher computational complexity, data independent achieves better interference suppression, when compared with data dependent beamformers. The negative effect of DOA estimation error is also examined, motivating the need for robust beamforming. Work presented on [Appendix A] and [Appendix B] address the issue in two dimensional arrays by utilising Slepian sequences to define the uncertainty region. Slepian sequences are well known for their ability to maximise the energy in specified (spatio)-spectral regions. The proposed beamformers are revealed as Generalized Sidelobe Cancellers (GSC) and use Slepian sequences with good energy concentration capabilities both in steering and the blocking branch. The difference between the work presented in [Appendix A] and [Appendix B] is the shape of the uncertainty area: in former it is rectangular and in latter, a disc. In both papers it has been shown, using numerical simulations, that the proposed approaches outperform traditional GSC.

In chapter dedicated to DOA estimation beamforming based, subspaces based and parametric DOA estimation algorithms are described. With the cost of higher computational complexity the parametric methods achieve acceptable levels of accuracy over a wider range of SNRs. Parametric methods are also shown to have better resolution capabilities. Work [Appendix C] proposes a Maximum A Posteriori (MAP) estimator to increase the span of SNRs, where estimation accuracy is in acceptable level. In order to achieve it, signal source knowledge about its position is used to achieve better consistency in DOA estimation. The numerical simulations showed that in case of large array covariance matrix mismatch, MAP based approach significantly outperformed ML and MUSIC algorithms.

KOKKUVÕTE

Uudsed algoritmid antennivõre väljundsignaali töötlemiseks

Antennivõred mängivad tänapäevastes sidesüsteemides võtmerolli ja on seetõttu jätkuvalt teadlaste huviorbiidis. Väite tõestuseks vaadeldgem kahte erinevat näidet.

Esmalt viienda põlvkonna mobiilne sidesüsteem (lühendatult 5G). Erinevad uuringud näitavad, et aastaks 2026 on nutitelefoni kasutaja igakuine tarbitav andmemaht kasvanud kuni 45GB-ni. Tasub märkimist, et see number ei sisalda endas teisi 5G pakutavaid teenused nagu näiteks juhtmeta koduinternet, erinevad värvvõrgu teenused või transpordiga seotud lahendused. Võib ainult ette kujutada, millised nõudmised erinevad teenused võrgu mahule ja läbilaskevõimele. Põhimõtteliselt ainus võimalus nõudmiste täitmiseks on kasutusele võtta ruumiline tihendamine. Seda siis lisaks juba eelnevates mobiilside põlvkondades kasutuses olevates aja- ja sagedusvalla tihendamisele. Ruumiline tihendamine eeldab, et saatja on võimeline signaali edastama ainult soovitud suunas, kasutusele tuleb võtta tõhusalt toimivad elektroonsed antenni juhtimise meetodid. Selleks, et teada, mis suunas antenni juhtida on omakorda tarvis signaali allika suuna määramise meetodeid. Loomulikult käib iga hinnanguga kaasas teatav määramatus ja loomulikult peab antenni juhtimine selle määramatusega toime tulema.

Teise näitena vaadeldgem õhuseire süsteemi. Laias laastus on see jagatud kihtideks, kus iga kiht hõlmab endas ühte õhuseire tehnoloogiat. Üldiselt on nii, et kihid on jagatud paigutatud tähtsuse järjekorras - alumised kihid on olulisemad ja ülemised kihid ohutuse seisukohast vähemolulised. Seiresüsteemi kaks alumist kihti (ADS-B and SSR [Mode S]) kasutavad sama sideprotokollit, mis omakorda kasutab ainult ühte 1090MHz asuvat kitsaribalist kanalit. Järjest kasvava lennuliikluse tihedusega ja lisanduvate õhuruumi kasutajatega (näiteks droonid) kanal ei suuda enam lisanduvat andmeliiklust teenindada ja lihtsalt öeldes, saab täis. Probleemide nimekirja pikendab veelgi õhuseire süsteemi puudulik turvalisus. Põhimõtteliselt saab kõiki eeltoodud probleeme leevendada antennivõrede laialdasema kasutusele võtuga. Antenni elektroonne juhtimine võimaldab ruumiliste filtreerimist suurendades seeläbi kanali mahtuvust. Tõhusaid signaali allika suuna määramise meetodeid on jällegi tarvis soovitud suuna määramiseks tarvis.

Käesolevas töös antakse ülevaade laialt levinumatest antenni juhtimise ja signaali allika suuna määramise meetodites.

Antenni juhtimise algoritmid saab jagada kahte suurde kategooriasse: signaali karakteristikutest sõltuvaid ja nendest sõltumatuid meetodid. Esimesse kategooriasse kuuluvate meetodite puhul konstrueeritakse antenni suunadiagrammi maksimaalne võimendus mingisse soovitud suunda signaali omadustest sõltumatult. Teisel juhul üritatakse saavutada sama tulemus, aga siin puhul võetakse arvesse signaali eeldatavaid karakteristikuid ja tulemus on mingis kindlas mõttes optimaalne selle konkreetse signaali tarvis. Üldiselt ollakse konsensusel ja töös on seda ka näidatud, et signaali karakteristikutest sõltuvad antennivõre juhtimise meetodid suudavad segavaid signaale mõju antennivõre väljundsignaalis paremini elimineerida. Samas on need kõiksugu ebakõladele (näiteks signaali allika suuna määramise vea) suhtes tundlikumad. Käesoleva töö lisades [Lisa A] and [Lisa B] esitatud artiklid pakuvad välja antennivõre juhtimise algoritmid, mis kasutavad Slepiani jadasid. Slepiani jasad on tuntud selle poolest, et olles näiteks ruumiliselt piiratud (antennil on lõplikud mõõtmed) kontsentreeruvad nad võimalikult suure hulga energiat määratud ruumiossa. [Lisa A] toodud töös on selle ruumiosa kontuur nelinurkne, [Lisa B] ringikujuline. Mõlemas töö raames tehtud simulatsioonid näitavad, et esitatud meetodid suudavad segavaid signaale tõhusalt kõrvaldada.

Signaali allika suuna määramise algoritmidele pühendatud peatükis vaadeldakse antennijuhtimise algoritmidel baseeruvaid, antennivõre alamruumi algoritmide baseeruvaid ja parameetrilise hindamise algoritmidele baseeruvaid meetodeid. Üldiselt ollakse ühel meelel ja seda on näidatud ka antud töös, et parameetrilised meetodid on täpsemad laiemas signaal-müra suhte vahemikus kui teised vaadeldud meetodid. Samuti on need võimelised lähestiku asuvaid signaali allikaid tõhusamalt eristama. [Lisa C] toodud töös esitatakse suurima *a posteriori* tõepära meetod, mis suudab suurima tõepära meetodiga võrreldes laiemas signaal-müra suhte vahemikus täpset signaali allika suunainfot esitada. Selleks kombineerib pakutud meetod omavahel signaali allika enda asukoha kohta info kokku antenni võre poolt leitud suuna hinnanguga. Töös toodud simulatsioonid näitavad, et juhul kui antennivõres on suhteliselt vähe elemente ja antennivõre kovariatsioonimaatriks on ebatäpne, suudab suurima *a posteriori* tõepära meetod teistest vaadeldud meetoditest signaali allika suunda täpsemini hinnata.

APPENDIX A

Two Dimensional Robust Beamforming for Air-Ground Communication System

A. Tart and T. Trump, 2014 Integrated Communications, Navigation and Surveillance Conference (ICNS) Conference Proceedings, Herndon, VA, USA, 2014, pp. B2-1-B2-8, doi: 10.1109/ICNSurv.2014.6819978.

TWO DIMENSIONAL ROBUST BEAMFORMING FOR AIR-GROUND COMMUNICATION SYSTEM

Allan Tart and Tõnu Trump, Tallinn University of Technology, Department of Radio and Communication Engineering, Ehitajate tee 5, Tallinn, 19086, Estonia

Abstract

This paper investigates a robust adaptive beamforming technique for two dimensional antenna array. Robustness is needed against imperfect knowledge of desired signal direction of arrival as well as against other errors. Erroneous estimation of source direction is especially true in air surveillance systems because aircraft are moving in high speed. Need for two dimensional antenna arrays is also substantial as aircraft are often at the same azimuth but at different elevation angles relative to ground system. Proposed algorithm is based on Generalized Sidelobe Canceller and uses Discrete Prolate Spheroidal Window or often referred to as Slepian window function. Only Slepian's corresponding to large spectral concentration are used in both steering and blocking branches.

1 Introduction

In air surveillance domain robust adaptive beamforming has got a great potential. The systems have no channel access control mechanism and only 1090MHz frequency band is used. Consequently there is a substantial number of colliding (garbled) messages [1]. Usually mechanically rotated or omnidirectional antennas are used in today's air surveillance systems. Instead, adaptive beamformers could be used to separate colliding messages and to reduce RF pollution. Degarbling of signals based on blind source separation has been proposed earlier (for example in [2]). The biggest drawback of these algorithms is that they are vulnerable against multipath propagation of signals. One has to take this into account when designing surveillance system for airport environment [3]. The problem with ordinary adaptive antenna array is that if the direction to the useful source is not known exactly, the beamformer easily takes the source to be the interferer and starts suppressing it. In this paper we propose a Robust Generalized Sidelobe Canceller where certain error in estimation of direction of arrival is allowed.

A number of different beamforming techniques has been described in [4]. In this paper we will use Discrete Prolate Spheroidal Windows (DPSW, also often referred to as Slepian sequences) to gain robustness against errors in direction of arrival estimates and other imperfections. The Slepian sequences have been used in beamforming contexts earlier ([5]). In this paper we will extend the theory to two dimensional case. It allows us to steer the main beam of antenna not only in horizontal but also in vertical plane. We do so because aircraft are often located at the same azimuth, but different heights. By using two dimensional antenna arrays we gain extra robustness against overlapping signals in space. Using adaptive beamforming will allow a more efficient use of frequency band by allowing communicating with a number of aircraft at the same frequency without interfering with each other.

The results of this paper are the bases for proposing a novel air-ground communication system architecture for exchanging CNS (Communication, Navigation and Surveillance) related data between areal and ground based systems. Next steps will be proposing a best suited Direction of Arrival (DOA) estimation algorithm and distributed beamforming algorithm for wireless sensor networks. Latter will eliminate the need for Central Processing Station (CPS) and by that enhance the reliability of overall system.

In this paper we assume the sensor array to be a 2D narrow band linear array. We propose a robust version of the two dimensional Generalized Sidelobe Canceller. To achieve robustness against imperfections of array calibration, errors in knowledge of direction of arrival of the desired signal, antenna coupling etc. we have used Slepian window functions in both the steering and blocking branches of the algorithm. The steering and blocking branches have been directed in opposite directions.

Throughout the paper the italic, bold face lower case and bold face upper case letters will be used for scalars, column vectors and matrices respectively. The

superscript T denotes transposition of a matrix, superscript H Hermitian transposition of a matrix and superscript $*$ stands for conjugate of a complex number. The symbol \otimes stands for Hadamard multiplication of two matrices and $\text{vec}(\cdot)$ represents vectorization of a matrix. Column vector consisting of all ones is denoted as $\mathbf{1} = [1,1,1,1]^T$, I denote identity matrix. Trace of a matrix is written as $\text{Tr}(\cdot)$.

2 Slepian Sequences

Let \mathbf{A} represent a $m \times n$ steering matrix toward angle (Φ_{AZ}, Φ_{EL})

$$A_{m,n} = [e^{i(m-1)\Phi_{AZ}} e^{i(n-1)\Phi_{EL}}] \quad (1)$$

In (1) Φ_{AZ} and Φ_{EL} denote respectively horizontal and vertical electrical angle of incidence of a planar wave impinging a linear sensor array, measured with respect to the normal to the array. Indexes $m = 1, \dots, M$ and $n = 1, \dots, N$ express the number of antenna elements in array on horizontal and vertical directions.

Discrete prolate spheroidal window, with size $M \times N$ and elements in matrix B , that for given angular region $D = [(-\varphi_{AZ}, \varphi_{AZ}), (-\varphi_{EL}, \varphi_{EL})]$ provides the maximal concentration of energy so that the spectral consecration

$$\lambda = \frac{\iint_D \|\mathbf{1}^T [B e A(\Phi_{AZ}, \Phi_{EL})] \mathbf{1}\|^2 d\Phi_{EL} d\Phi_{AZ}}{\iint_G \|\mathbf{1}^T [B e A(\Phi_{AZ}, \Phi_{EL})] \mathbf{1}\|^2 d\Phi_{EL} d\Phi_{AZ}} \quad (2)$$

is maximal. In the above $G = [(-\pi, \pi), (-\pi, \pi)]$

In what follows we drop explicit arguments Φ_{AZ} and Φ_{EL} , if they are not necessary to avoid confusion.

Let us normalize the total power in the denominator of ((2)) to unity. We then need to maximize

$$\lambda = \iint_D \|\mathbf{1}^T [B e A] \mathbf{1}\|^2 d\Phi_{EL} d\Phi_{AZ} \quad (3)$$

It has been shown in [6] that

$$y^H (S e V) x = \text{Tr}[(y I)^H S (x I) V^T] \quad (4)$$

where S and V are arbitrary matrices; x and y arbitrary column vectors with respectful lengths. Taking into account equation ((4)) we can write

$$\mathbf{1}^T [B e A] \mathbf{1} = \text{Tr}(B A^T) \quad (5)$$

It can be shown that trace of a matrix product can be written as follows

$$\text{Tr}(B A^T) = \text{Tr}(B^T A) = \text{vec}(B^T) \text{vec}(A) \quad (6)$$

We now can write ((3)) as follows

$$\begin{aligned} \lambda &= \iint_D \text{vec}(B)^T \text{vec}(A) \text{vec}(A)^T \text{vec}(B) d\Phi_{EL} d\Phi_{AZ} \\ &= \text{vec}(B)^T \iint_D \text{vec}(A) \text{vec}(A)^T d\Phi_{EL} d\Phi_{AZ} \text{vec}(B) \\ &= b^T \mathcal{A} b \end{aligned} \quad (7)$$

where $\mathcal{A} = \iint_D \text{vec}(A) \text{vec}(A)^T d\Phi_{EL} d\Phi_{AZ}$ is a $MN \times MN$ square matrix and b is a vectorized version of B . What reveals from ((7)) is that the discrete prolate spheroidal windows can be represented as orthonormal eigenvectors of matrix \mathcal{A} . It has been shown in [7] that the matrix \mathcal{A} is positive-definite and it is evident that the maximum value of (2) is 1. Thus all eigenvalues of \mathcal{A} lie between 0 and 1 and show how well given eigenvector can concentrate energy to the angular region D .

We now show how one can calculate matrix \mathcal{A} . Steering matrix A can be written as

$$A = [a_1, a_2, \dots, a_N] \quad (8)$$

where $a_n = [e^{i(m-1)\Phi_{AZ}} e^{i(n-1)\Phi_{EL}}]$ is a column vector. Square of vectorized matrix A can be represented as

$$\begin{aligned} \text{vec}(A) \text{vec}(A)^T &= \\ \begin{bmatrix} a_1 a_1^T & a_1 a_2^T & \dots & a_1 a_N^T \\ a_2 a_1^T & a_2 a_2^T & \dots & a_2 a_N^T \\ \vdots & \vdots & \ddots & \vdots \\ a_N a_1^T & a_N a_2^T & \dots & a_N a_N^T \end{bmatrix} \end{aligned} \quad (9)$$

One can see that $\text{vec}(A) \text{vec}(A)^T$ is consistent of N^2 square matrices with size $M \times M$. To be able to find each element of \mathcal{A} we first need to calculate $\iint_D (a_k a_l^T)_{u,v} d\Phi_{EL} d\Phi_{AZ}$

$$\begin{aligned} &\iint_D (a_k a_l^T)_{u,v} d\Phi_{EL} d\Phi_{AZ} \\ &= \iint_D e^{i(u+v-2)\Phi_{AZ}} e^{i(k+l-2)\Phi_{EL}} d\Phi_{EL} d\Phi_{AZ} \\ &= 4 \frac{\sin(\varphi_{AZ}(u+v-2)) \sin(\varphi_{EL}(k+l-2))}{u+v-2} \frac{1}{k+l-2} \end{aligned} \quad (10)$$

where $(l, k) = 1, \dots, N$ indicates a specific product of vectors in (9) and $(u, v) = 1, \dots, M$ marks each element in outcome matrix of a vector product.

3 Adaptive General Sidelobe Canceller

In this section we describe the theory of operations of Adaptive General Sidelobe Canceller (AGSC). We will use the AGSC as referents to be compared with the proposed Robust Adaptive General Sidelobe Canceller. The block diagram of AGSC is shown on Figure 1.

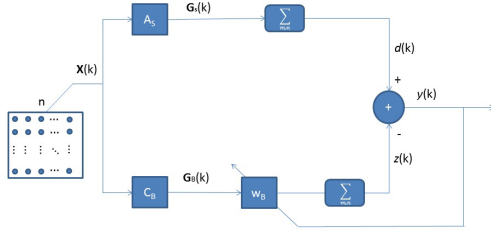


Figure 1. Block Diagram of Two Dimensional Adaptive General Sidelobe Canceller

The Adaptive General Sidelobe Canceller consists of steering and blocking branch. The goal of steering branch is to allow the signal from desired sources pass through the branch unimpeded. Output of steering branch $d(k)$ can be written as

$$d(n) = 1(A_s eX(k))1 \quad (11)$$

where A_s in equation is a steering matrix toward desired source and $X(k)$ is a signal impinging antenna array at time instance k and is given with equation ((12)).

$$X(k) = \sum_{d=1}^D A^{(d)} s_d(k) + V(k) \quad (12)$$

where D is a number of a sources, $s_d(k)$ is a d -th emitter signal at time instance k , $V(k)$ is an additive zero mean Gaussian noise. $A^{(d)}$ is an antenna steering matrix for d -th source with elements $A_{m,n}^{(d)} = [e^{i(m-1)\Phi_{d,AZ}} e^{i(n-1)\Phi_{d,EL}}]$.

An example of the response of a steering branch is shown on Figure 2. The values shown are in decibels.

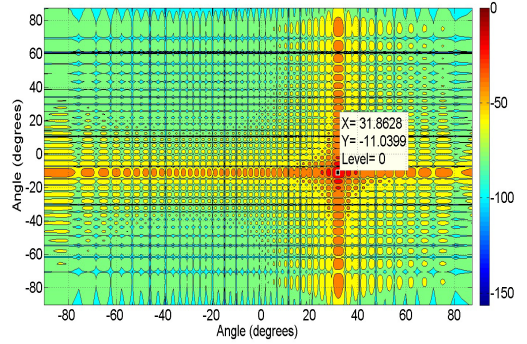


Figure 2. An Example of the Response of a Steering Branch

The goal of the blocking branch is to be prevented signal from desired source from passing trough. The output of blocking branch is given by

$$z(k) = w_b G_B 1 \quad (13)$$

where w_b is a weight vector updated by Normalized Least Mean Square rule but other adaptive algorithms may be used instead. G_B is calculated as follows

$$G_B = C_U X(k) C_V \quad (14)$$

The matrices C_U and C_V are subtracted from the steering matrix toward desired source A_s as follows.

We are using singular value decomposition of a A_s as proposed in [8] so that

$$A_s = USV^H \quad (15)$$

where U is a $M \times M$ matrix containing orthonormal eigenvectors of $A_s A_s^H$, V is a $N \times N$ matrix consistent of orthonormal eigenvectors of $A_s^H A_s$. S , with size $M \times N$, contains the singular values of A_s in its diagonal in descending order. Singular values of a matrix essentially are the square roots of the eigenvalues of both $A_s A_s^H$ and $A_s^H A_s$.

We can write U and V as follows

$$U = [u_1, u_2, \dots, u_M] \\ V = [v_1, v_2, \dots, v_N] \quad (16)$$

where u_n and v_m are column vectors with lengths M and N respectively.

The matrices C_U and C_V in equation (14) are formed as

$$\begin{aligned} C_U &= [u_2, u_3, \dots, u_M] \\ C_V &= [v_2, v_3, \dots, v_N] \end{aligned} \quad (17)$$

One can note that we have discarded the first columns from matrices U and V in equation (16). By doing so we assure that the signal from desired source will not pass through the blocking branch whereas signals from all other sources do. An example of the response of a blocking branch is shown on Figure 3. The values shown are in decibels.

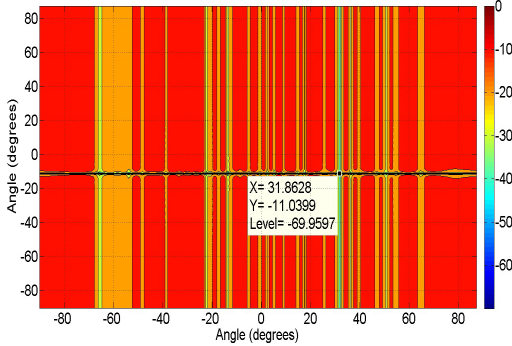


Figure 3. An Example of the Response of a Blocking Branch

The output of Adaptive General Sidelobe canceller can be written as

$$y(k) = d(k) - z(k) \quad (18)$$

where $d(k)$ and $z(k)$ are the outputs of steering and blocking branch at the k -th time instance respectively.

4 A Robust Adaptive Generalized Sidelobe Canceller for Two Dimensional Antenna Array

In this section we are giving theory of operations of the robust adaptive generalized sidelobe canceller for two dimensional antenna array as shown in Figure 4.

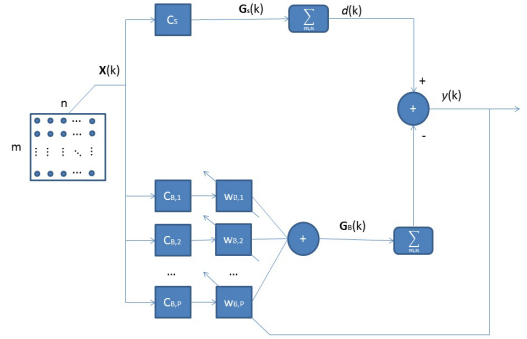


Figure 4. Block Diagram of Robust Generalized Sidelobe Canceller for 2D Antenna Array

Beamformer consists two branches. The upper branch directs the antenna beam toward the desired source and the lower branch blocks the signal from desired source.

The window steering matrix C_s is given by

$$C_s = A_s^{(0)}(\varphi_{0,AZ}, \varphi_{0,EL})eB_s, \quad (19)$$

where $A_s^{(0)}(\varphi_{0,AZ}, \varphi_{0,EL})$ is a steering matrix toward desired source and B_s is a Slepian window used.

One has to bare in mind that the bandwidth of Slepian window should be chosen relatively narrow for assuring good noise suppression but wide enough for taking into account the errors of direction of arrival estimations. Response of steering branch, G_s , toward angle $(2^\circ, 2^\circ)$ with one Slepian window is shown on Figure 5. The values shown are in decibels.

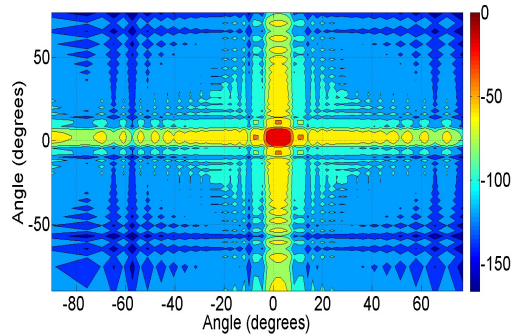


Figure 5. Response of Steering Branch G_s

The desired signal output on the upper branch is given by

$$d(k) = 1^T G_s(k) \mathbf{1}. \quad (20)$$

where,

$$G_s(k) = C_s eX(k) \quad (21)$$

The window blocking matrices $C_{b,p}$ are given by

$$C_{b,p} = A_b^{(0)}(\varphi_{0,AZ}, \varphi_{0,EL}) eB_{b,p} \quad (22)$$

where $B_{b,p}$ stand for p -th broadband Slepian windows, $p = 1P$ and P stands for the total number of Slepian windows used. The need for multiple Slepian window functions to be used in the blocking branch arises from the fact that the number of interfering sources that can be suppressed is limited with the number of Slepian window functions used in the algorithm.

Matrix $A_b^{(0)}(\varphi_{0,AZ}, \varphi_{0,EL})$ is given by

$$A_b^{(0)}(\varphi_{0,AZ}, \varphi_{0,EL}) = [e^{i(m-1)(\varphi_{0,AZ}+\pi)} e^{i(n-1)(\varphi_{0,EL}+\pi)}] \quad (23)$$

Idea is to achieve contrary to A_s so that the output of blocking branch will not contain any components of a signal from desired source.

Matrix $G_B(k)$ is formed as

$$G_B(k) = \sum_{p=1}^P w_{b,p} C_{b,p} eX(k), \quad (24)$$

where coefficients $w_{b,p}$ are updated using Normalized Least Mean Squares rule. It must be noted that any other adaptive scheme can be used instead. Output of blocking branch is shown on Figure 6. The values shown are in decibels

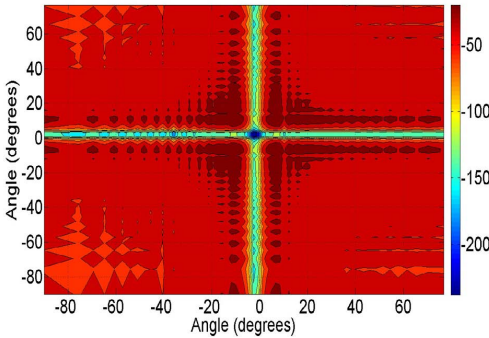


Figure 6. Response of Blocking Branch G_b

The output signal $y(k)$ of whole algorithm is given by

$$y(k) = d(k) - 1^T G_B(k) 1. \quad (25)$$

The eigenvalues of Slepian window functions used in the example in this section are shown in Figure 7. It is evident that window functions used are good in concentrating energy into the specified angular region. Eigenvalue of a steering Slepian is shown with \circ and eigenvalues used in blocking branch with $*$.

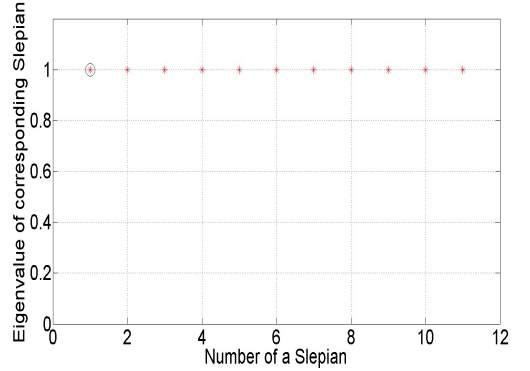


Figure 7. Eigenvalues of Used Slepian Window Functions

5 Simulation Results

In our first simulation example we are using a 32×32 planar antenna array consisting antenna elements with uniform spacing of half wave length and directed toward the array broadside. The source of desired signal is supposed to be at $(-23^\circ, -51^\circ)$ but actually is located at $(-25^\circ, -49^\circ)$ The power of desired signal is set to be unity, There are two interferes at $(60^\circ, 40^\circ)$ and $(-60^\circ, -10^\circ)$ with powers $P_{I,1} = 100$ and $P_{I,2} = 400$ respectively. At all the antenna elements there is also independent Gaussian noise present with power $\sigma_v^2 = 1$.

In the steering branch we use one Slepian window function and seven in blocking branch. We have chosen them so that the eigenvalue $\lambda = 1$ for all the window functions used shown on Figure 8. The eigenvalue of a steering Slepian is shown with \circ and eigenvalues used in blocking branch with $*$.

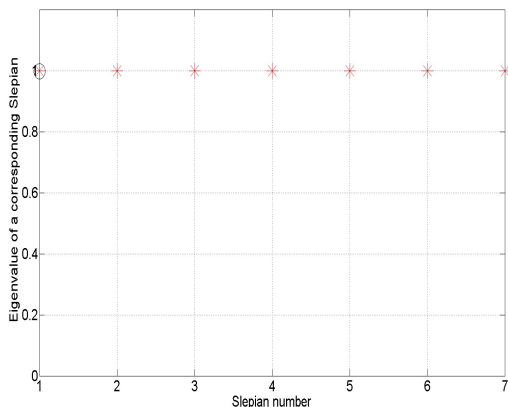


Figure 8. Eigenvalues of Slepian Window Functions (Direction of the Desired Source $(-25^\circ, -49^\circ)$)

The steady state antenna pattern is shown on Figure 9. The values shown are in decibels. One can see that at angles $(-25^\circ, -49^\circ)$ the gain of an antenna is about 3 dB below the maximum gain which is located at $(-23^\circ, -51^\circ)$. Whereas in the directions of the interferes the gain of a antenna is more than -101 dB for first and more than -91 dB for second interfering signal source.

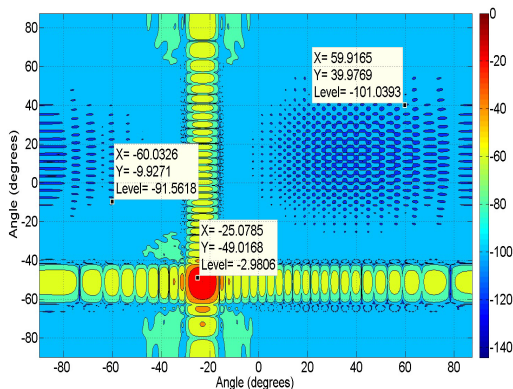


Figure 9. Antenna Pattern of the Proposed Sidelobe Canceller (Direction of the Desired Source $(-25^\circ, -49^\circ)$)

Evolution of the magnitudes of NLMS filter coefficients, used in the blocking branch, are shown on Figure 10. As there are virtually no components of desired signal in the blocking branch, the NLMS filter is supposed to suppress as much of interfering signal and noise as possible. We can see from the Figure 10 that the system under view achieves its steady state after 5000 iterations.

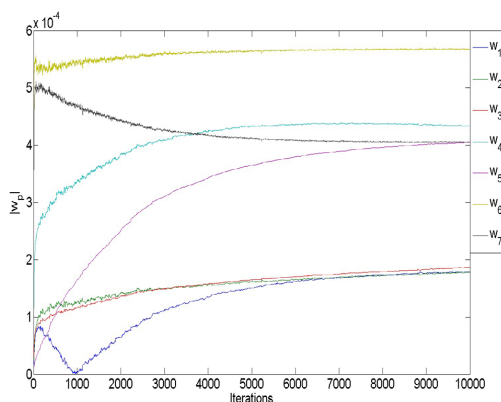


Figure 10. Evolution of NLMS Filter Coefficients Magnitudes (Direction of the Desired Source $(-25^\circ, -49^\circ)$)

In our second example the desired signal source is located at $(30^\circ, -11^\circ)$ whereas it is expected to be at $(33^\circ, -9^\circ)$. The power of a signal is again set to unity. The interferes in this example are located at $(-25^\circ, -40^\circ)$ and $(0^\circ, 0^\circ)$ and powers of interferes has been increased to $P_{I,1} = 1400$ and $P_{I,2} = 1100$ respectively. As in first example, there is an independent Gaussian noise present at all the antenna elements with power $\sigma_v^2 = 1$.

We are using 48×32 planar antenna array consisting antenna elements with uniform spacing of half wave length and directed toward the array broadside. We have chosen six Slepian window functions from different set for given example. But we have chosen them so that the eigenvalues remain $\lambda = 1$ as shown on Figure 11. The eigenvalue of a steering Slepian is shown with \circ and eigenvalues used in blocking branch with $*$.

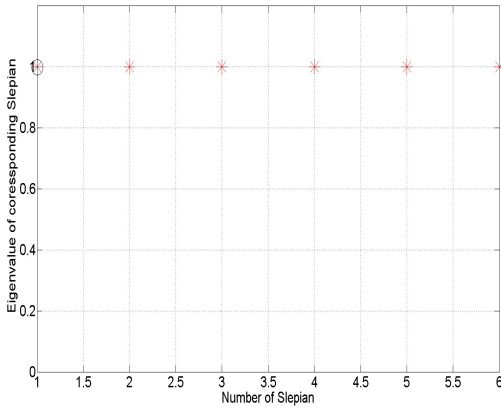


Figure 11. Eigenvalues of Slepian window functions (direction of the desired source $(30^\circ, -11^\circ)$;))

The antenna pattern in this example is given on Figure 12. The values shown are in decibels. As one can see, the gain on actual desired source direction is less than -3 dB below the maximum gain at $(30^\circ, -11^\circ)$. The antenna gains in the directions of the interfering sources are -75 dB and -114 dB below maximum. Due to the fact that we have used more antenna elements in horizontal plane than in vertical, one can notice slightly lower sidelobes in horizontal plane.

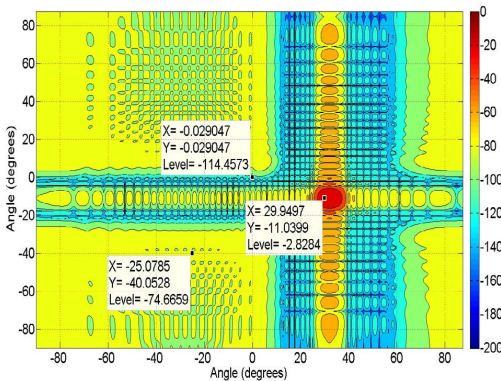


Figure 12. Antenna Pattern of the Proposed Sidelobe Canceller (Direction of the Desired Source $(30^\circ, -11^\circ)$)

As in first example, we are interested in the evolution of NLMS filter coefficients used in the blocking branch. They are shown on Figure 13. One can see that the system achieves its steady state after 500 steps. Higher fluctuation of the coefficients is explained with higher interfering signals powers.

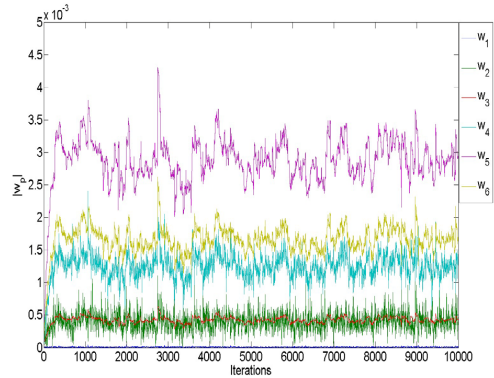


Figure 13. Evolution of NLMS Filter Coefficients Magnitudes (Direction of the Desired Source $(30^\circ, -11^\circ)$)

In the third example, the signal and antenna parameters are exactly the same as in the second example. The desired source is located at $(30^\circ, -11^\circ)$ whereas it is expected to be at $(33^\circ, -9^\circ)$. The power of a signal is set to unity. The interferes are located at $(-25^\circ, -40^\circ)$ and $(0^\circ, 0^\circ)$ and powers of interferes are $P_{I,1} = 1400$ and $P_{I,2} = 1100$ respectively. There is an independent Gaussian noise present at all the antenna elements with power $\sigma_v^2 = 1$. Planar antenna array consists 48×32 equally spaced elements which are directed toward antenna broadside.

The evolution of the first six filter coefficients, used in the AGSC, are shown on the Figure 14. It implies that the steady state antenna pattern is achieved approximately after 500 steps. The steady state antenna pattern of Adaptive General Sidelobe Canceller is shown on Figure 15. The values shown are in decibels. One can see that although, the in the direction of the interferes the antenna gain is low (-54 dB and -62 dB), it is also low at the actual direction of desired source (-24 dB). It clearly shows that performance of the Generalized Sidelobe Canceller is easily impacted by the erroneous estimate of the direction of arrival.

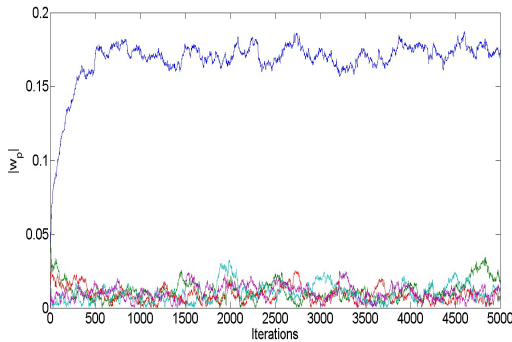


Figure 14. Evolution of First Six Coefficients Magnitudes of the NLMS Filter Used in the AGSC (Direction of the Desired Source ($30^\circ, -11^\circ$)).

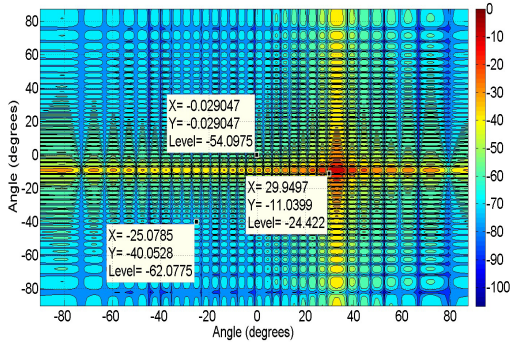


Figure 15. Antenna Pattern of the Adaptive Sidelobe Canceller (Direction of the Desired Source ($30^\circ, -11^\circ$)).

6 Conclusions

In this paper we propose a Robust Generalized Sidelobe Canceller using Slepian window functions that can be used in air-ground communications system. We have extended the theory to two dimensions so that 2D antenna arrays may be used for gaining extra robustness.

The theoretical results have been confirmed by simulation results. It has been shown that in imperfect knowledge of the direction of the desired source, the proposed sidelobe canceller suppresses the signal only 3 dB, whereas the interfering signals will be suppressed -75 dB minimally. Under the same conditions the General Sidelobe Canceller suppresses signal from the desired source more than -24 dB

showing clearly the advantages of proposed robustified sidelobe canceller.

The proposed algorithm is a bases for proposing a novel communication system using distributed beamforming algorithm.

References

- [1] M. C. Stevens, *Secondary Surveillance Radar*. Artech House, 1988.
- [2] N. Petrochilos, G. Galati, and E. Piracci, "Separation of Ssr Signals by Array Processing in Multilateration Systems," in *IEEE Transactions on Aerospace and Electronic Systems*, vol. VOL. 45, no. NO. 3, July 2009, pp. 965–982.
- [3] C. Reck, M. S. Reuther, U. Berold, and L. Schmidt, "Spatial filtering and Equalization for Ssr Signal Detection in a Multipath Environment," in *Microwave Conference (GeMIC)*, 2011, pp. 1–4.
- [4] J. Li and P. Stoica, Eds., *Robust Adaptive Beamforming*. John Wiley and Sons Inc, 2006.
- [5] T. Trump, "A Robust Adaptive Sensor Array with Slepian Sequences," in *Sensor Array and Multichannel Signal Processing Workshop (SAM), 2012 IEEE 7th*, 2012.
- [6] R. A. Horn and C. R. Johnson, *Topics in Matrix Analysis*. Cambridge University Press, 1991.
- [7] D. Slepian, "Prolate Spheroidal Wave Functions, Fourier Analysis and Uncertainty -v: The discrete case," *The Bell System Technical Journal*, pp. 1372–1430, May-June 1978.
- [8] B. D. Van Veen and K. M. Buckley, "Beamforming: A Versatile Approach to Spatial Filtering," *IEEE ASSP Magazine*, pp. 4–24, April 1988.

Acknowledgements

This research was supported by the Estonian Doctoral School in Information and Communication Technology.

*2014 Integrated Communications Navigation and Surveillance (ICNS) Conference
April 8-10, 2014*

APPENDIX B

Addressing Security Issues in ADS-B with Robust Two Dimensional Generalized Sidelobe Canceller

A. Tart and T. Trump, 2017 22nd International Conference on Digital Signal Processing (DSP), London, UK, 2017, pp. 1-5, doi: 10.1109/ICDSP.2017.8096046.

Addressing Security Issues in ADS-B with Robust Two Dimensional Generalized Sidelobe Canceller

Allan Tart
Thomas Johann Seebeck Department of Electronics
Tallinn University of Technology
Tallinn, Estonia
Email: allan.tart@ttu.ee

Tõnu Trump
Virgostell OÜ
Tallinn, Estonia
Email: tonu.trump@gmail.com

Abstract—One of the main reasons why ADS-B (Automatic Dependant Surveillance - Broadcast) has not been accepted as main source of surveillance information for Air Traffic Control (ATC) systems is its relative vulnerability against false target position reports. To remediate the issue, today's systems usually have independent surveillance system verifying the correctness of the ADS-B messages. This will make the overall air surveillance system complex and expensive. A thorough overview about the ADS-B security issues and possible realistic solutions are given in [1]. We will propose an alternative solution based on two dimensional beamforming algorithm. It will be based on Robust Generalized Sidelobe Canceller which uses Slepian sequences to address this problem. Potential other applications of proposed algorithm is Massive MIMO or any other communication system that needs simultaneous data transmission between spatially segregated nodes.

I. INTRODUCTION

Array signal processing has played an important role in many diverse applications for decades. Areas where it has been implemented ranges from seismology and medical diagnosis to radar and communication systems. Due to new emerging technologies (just to give an example: Massive MIMO), array processing still is an exciting topic among signal processing research community. In parallel with new technologies, usage of array processing algorithms has risen into focus also in more traditional communication systems. One example being in civil Air Traffic Control (ATC) air-ground communication systems (for example in [2], [3] and [4])

In this paper we are focusing on beamforming, one of the tasks of array processing. In broad terms, beamformers can be classified as *data-independent* and *data-dependant*. It is generally acknowledged that data-dependant or *adaptive* beamformers can have better resolution and interferer rejection capabilities than the data-dependant. But, at the same time, latter are more sensitive to the erroneous direction of arrival (DOA) estimates, array calibration errors and other imperfections.

Much effort has been put into studying robust beamformers against these imperfections. Among other popular approaches (we encourage interested reader to turn to [5] for examples), several authors have proposed algorithms based on Slepian sequences (often also referred to as Discrete Prolate Spheroidal Sequences (DPSS)) - for example in [6], [7] and [8]. Distinctive feature of DPSS-s is their capability to concentrate energy within a specified band of spatial frequencies while

also being limited in spatial domain. Due to the fact that sources often are located at the same azimuth but at different elevation angles, two dimensional antenna arrays will allow better discrimination between desired and interfering signals. We will find two dimensional Slepian sequences that could be used in Uniform Rectangular Array (URA), where the spectral region we want the maximal energy concentration will be circular. In a sense, the work presented in current paper is a continuation to the work proposed in [9], where GSC using Slepian sequences with rectangular band-limitation were used. The source actual location is within a circular area rather than in rectangular area, meaning we expect circular band-limitation to be better suited for the given application.

In the last section of this article we will show that the proposed algorithm is capable to receive desired ADS-B message and suppress spitefully injected fake target message. Due to the relative openness of ADS-B message transmission protocol, 1090ES, the vulnerability to false target injection forbids the usage of ADS-B as sole means of surveillance in Air Traffic Control.

Throughout the remainder of this paper italic, bold face lower case and bold face upper case letters will be used for scalars, column vectors and matrices respectively. The superscript T denotes transposition of a matrix, superscript H Hermitian transposition of a matrix and superscript $*$ stands for conjugate of a complex number. The symbol \odot stands for Hadamard and \otimes for Kronecker product of two matrices; $\text{vec}(\cdot)$ represents vectorization of a matrix. Column vector consisting of all ones is denoted as $\mathbf{1} = [1, 1, 1, \dots, 1]^T$, \mathbf{I} denote identity matrix. Trace of a matrix is written as $\text{Tr}(\cdot)$. We will use $\|\cdot\|$ to denote L_2 norm of a vector.

II. TWO DIMENSIONAL SLEPIAN SEQUENCES

We will consider a planar array lying on $x-y$ plane with uniform rectangular grid. The array consists of $M \times N$ isotropic sensors with the distance d between consequent elements. The position of each element can be described by a vector:

$$\mathbf{p}_{m,n} = d \begin{bmatrix} m \\ n \end{bmatrix} \quad (1)$$

where $m = 0, 1, \dots, M-1$ and $n = 0, 1, \dots, N-1$.

Plane wave impinging an array from elevation angle θ and azimuth angle ϕ at discrete time instance t will produce a signal s on m, n -th sensor:

$$\begin{aligned}
s(\mathbf{p}_{m,n}, t) &= a(t)e^{-i(\omega t + \mathbf{k}^T \mathbf{p}_{m,n})} \\
&= a(t)e^{-i\omega t} e^{-i\mathbf{k}^T \mathbf{p}_{m,n}} \\
&= \alpha(t)e^{-i\mathbf{k}^T \mathbf{p}_{m,n}}, \tag{2}
\end{aligned}$$

where $a(t)$ is an amplitude of a signal, $\alpha(t) = a(t)e^{-i\omega t}$, ω is a temporal frequency, \mathbf{k} is a wavenumber vector:

$$\mathbf{k} = -\frac{2\pi}{\nu} \begin{bmatrix} \sin \theta \cos \phi \\ \sin \theta \sin \phi \end{bmatrix} = -\frac{2\pi}{\nu} \begin{bmatrix} u_x \\ u_y \end{bmatrix} \tag{3}$$

where ν is a wavelength of the signal s and tied with temporal frequency ω as follows: $\nu = \frac{\omega}{c}$, with c being a speed of light. After substituting (1) and (3) into (2) latter becomes:

$$\begin{aligned}
s(\mathbf{p}_{m,n}, t) &= \alpha(t)e^{-i\frac{2\pi d}{\nu}(m \sin \theta \cos \phi + n \sin \theta \sin \phi)} \\
&= \alpha(t)e^{-i\frac{2\pi d}{\nu}(mu_x + nu_y)} \tag{4}
\end{aligned}$$

As the notation using u_x and u_y to define \mathbf{k} in (3) and (4) is more convenient, we will not be making explicit reference to targets actual direction θ and ϕ in the reminder of this article.

One can note that both u_x and u_y can take values between -1 and 1 . We will denote the set containing all possible values of u_x and u_y with Ω .

Based on (4) we can construct a signal matrix $\mathbf{S}(t)$, its m, n -th value is equal to:

$$[\mathbf{S}(t)]_{m,n} = a(t)e^{-i\omega t} [\mathbf{V}(u_x, u_y)]_{m,n} \tag{5}$$

where \mathbf{V} can be expressed with equation:

$$[\mathbf{V}(u_x, u_y)]_{m,n} = e^{-i\frac{2\pi d}{\nu}(mu_x + nu_y)} \tag{6}$$

For ease of notation, we have dropped explicit references to \mathbf{p} in (5), (6) and in what follows.

To simplify our calculations, we will stack the columns of matrices $\mathbf{S}(t)$ and $\mathbf{V}(u_x, u_y)$, as a result we will get $MN \times 1$ vectors:

$$\mathbf{s}(t) = \text{vec}(\mathbf{S}(t)) \quad \text{and} \quad \mathbf{v}(u_x, u_y) = \text{vec}(\mathbf{V}(u_x, u_y)) \tag{7}$$

We will refer to these vectors as *signal vector* and *steeringvector* respectively; (5) will take the following form:

$$\mathbf{s}(t) = \alpha(t)\mathbf{v}(u_x, u_y), \tag{8}$$

Having revealed *steeringvector* \mathbf{v} we can define *beam pattern* \mathcal{B} :

$$\mathcal{B}(u_x, u_y) = \mathbf{w}^H \mathbf{v}(u_x, u_y) \tag{9}$$

and *power pattern* \mathcal{P} :

$$\mathcal{P}(u_x, u_y) = \|\mathcal{B}(u_x, u_y)\|^2 \tag{10}$$

$$= \mathbf{w}^H \mathbf{v}(u_x, u_y) \mathbf{v}^H(u_x, u_y) \mathbf{w} \tag{11}$$

$$= \mathbf{w}^H \mathbf{D} \mathbf{w} \tag{12}$$

Vector \mathbf{w} in (9) and (11) contains array coefficients and the matrix \mathbf{D} is a matrix with size $MN \times MN$ and its (g, h) -th element is defined as follows:

$$[\mathbf{D}]_{g,h} = e^{-i\frac{2\pi d}{\nu}(u_x(m-o) + u_y(n-p))} \tag{13}$$

where $g = m + Mn + 1$ and $h = o + Mp + 1$, with $(m, o) = 0, 1, \dots, M-1$ and $(n, p) = 0, 1, \dots, N-1$.

Our task is to find \mathbf{w} so that it maximizes the power pattern in given direction u_x and u_y .

Due to the fact, that in our application, the position of the target is changing rapidly, it is beneficial to robustify the array. Instead of defining one direction, we should define an area \mathcal{K} , where we will expect the target to be i.e. $\{u_x, u_y\} \in \mathcal{K}$. It is evident that \mathcal{K} is as subset of Ω , i.e. $\mathcal{K} \subseteq \Omega$. Meaning that we need to maximize the following relation:

$$\lambda = \frac{\int_{\mathcal{K}} \mathcal{P}(u_x, u_y) du_x du_y}{\int_{\Omega} \mathcal{P}(u_x, u_y) du_x du_y}, \tag{14}$$

After normalizing the total power in the denominator of (14) to unity we then need to maximize

$$\lambda = \int_{\mathcal{K}} \mathcal{P}(u_x, u_y) du_x du_y \tag{15}$$

Although \mathcal{K} can be shaped arbitrarily as shown in [10], we will define \mathcal{K} as a disc on Cartesian plane with radius K , meaning

$$\|\mathbf{k}\|^2 \leq K^2 \tag{16}$$

To simplify the calculations we will change from Cartesian to polar coordinates:

$$\begin{bmatrix} u_x \\ u_y \end{bmatrix} = \begin{bmatrix} k \cos(\psi) \\ k \sin(\psi) \end{bmatrix} \tag{17}$$

(15) takes the following form:

$$\lambda = \int_0^K k dk \int_0^{2\pi} \mathcal{P}(k, \psi) d\psi \tag{18}$$

$$= \mathbf{w}^H \left(\int_0^K k dk \int_0^{2\pi} \mathbf{D} d\psi \right) \mathbf{w} \tag{19}$$

$$= \mathbf{w}^H \mathbf{Z} \mathbf{w} \tag{20}$$

where we have made the substitution:

$$\mathbf{Z} = \int_0^K k dk \int_0^{2\pi} \mathbf{D} d\psi \tag{21}$$

It reveals from (20) that the weight vector \mathbf{w} is the eigenvector of \mathbf{Z} and the value λ is the corresponding eigenvalue. The (g, h) -th value of \mathbf{Z} is given by

$$[\mathbf{Z}]_{g,h} = \int_0^K k dk \int_0^{2\pi} e^{-i\frac{2\pi d}{\nu} k (\cos(\psi)(m-o) + \sin(\psi)(n-p))} d\psi \tag{22}$$

$$= K \cdot \frac{J_1(K \sqrt{(m-o)^2 + (n-p)^2})}{\sqrt{(m-o)^2 + (n-p)^2}} \tag{23}$$

where $J_\alpha(x)$ is a α -order Bessel function of the first kind. \mathbf{Z} is a positive definite kernel matrix with Hermitian symmetry. Values of λ are between $0..1$ and it shows how well the corresponding eigenvector \mathbf{w} concentrates power into specified

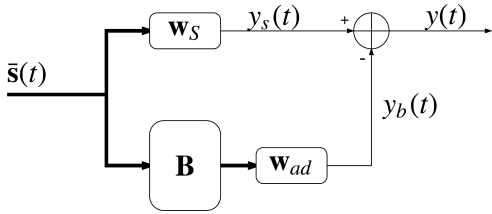


Fig. 1. Structure of Generalized Sidelobe Canceller.

region \mathcal{K} . To emphasize Slepian sequences dependence on the specified are \mathcal{K} we will denote it by $\mathbf{w}(\mathcal{K})$ in the remainder of the article.

Another useful feature of eigenvectors is that they are orthogonal. This is especially important in the following discussion, where we will apply two dimensional Slepian sequences in the General Sidelobe Canceller.

III. ROBUST GENERALIZED SIDELOBE CANCELLER WITH SLEPIAN SEQUENCES

In this section we will give an overview about the General Sidelobe Canceller using Slepian sequences. We will refer to it as S-GSC.

In practical situations we have a collection of signals from different directions impinging the array. From the compilation of signals $\bar{\mathbf{s}}$ our task is to extract signal of our interest \mathbf{s}_d :

$$\bar{\mathbf{s}}(t) = \mathbf{s}_d(t) + \sum_{l=1}^L \mathbf{s}_l(t) + \boldsymbol{\eta} \quad (24)$$

where \mathbf{s}_l is a l -th interfering signal from total of L interfering signals and $\boldsymbol{\eta}$ is an additive noise. Both \mathbf{s}_d and \mathbf{s}_l are defined by (8).

The signal is feed into the S-GSC shown on Fig. 1, where it is directed into two branches: upper *steering branch* and lower *blocking branch*.

The task of a steering branch is to direct the beam toward desired source whereas the task of blocking branch is to block the signal from the desired source.

We will begin by defining the signal path in the steering bath. The output signal $y_s(t)$ is given by:

$$y_s(t) = \mathbf{w}_s^H \bar{\mathbf{s}}(t) \quad (25)$$

The steering branch weight vector is given by

$$\mathbf{w}_s = \mathbf{w}(\mathcal{K}_d) \odot \mathbf{v}_d \quad (26)$$

In (26), $\mathbf{w}(\mathcal{K}_d)$ denotes the Slepian sequence which corresponds to the largest eigenvalue. The variable \mathcal{K}_d denotes the area where we wish to concentrate the power pattern of the array. In the steering branch it should be relatively narrow. Vector \mathbf{v}_d is the steering vector toward desired source.

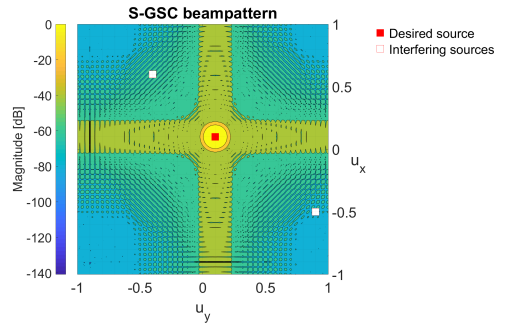


Fig. 2. Example of GSC beam pattern with Slepian Sequences.

Blocking branch output signal is given by

$$y_b(t) = \mathbf{w}_{ad}^H (\mathbf{B}^H \bar{\mathbf{s}}(t)) \quad (27)$$

In (27) \mathbf{B} is so called *blocking matrix*. It is given by the following equation

$$\mathbf{B} = \mathbf{W}_b(\mathcal{K}_{db}) \odot \mathbf{v}_{db} \quad (28)$$

where $\mathbf{W}_b(\mathcal{K}_{db})$ is $MN \times \mathcal{N}_c$ matrix containing relatively broadband Slepian sequences. The steering vector \mathbf{v}_{db} is directed toward the opposite location as compared to the Slepian in the steering branch.

$$\mathbf{v}_{db} = \text{vec}(\mathbf{V}_{db}), \quad (29)$$

where the m, n -th element of \mathbf{V}_{db} is given by the equation:

$$[\mathbf{V}_{db}]_{m,n} = e^{-i \frac{2\pi d}{\nu} (m(u_x^{(d)}+1) + n(u_y^{(d)}+1))} \quad (30)$$

The steering branch output signal $y_s(t)$ and the blocking matrix output $\mathbf{y}_b(t) = \mathbf{B}^H \bar{\mathbf{s}}(t)$ can be used as the input and desired signals respectively in any adaptive algorithm to select the blocking weights \mathbf{w}_{ad} . In the context of current paper, we are using NLMS (Normalized Least Mean Squares) adaptive algorithm. GSC output signal $y(t)$ and adaptive filter \mathbf{w}_{ad} update is given by:

$$y(t) = y_s(t) - y_b(t) \quad (31)$$

$$P(t+1) = \gamma P(t) + (1-\gamma) \mathbf{y}_b^H(t) \mathbf{y}_b(t) \quad (32)$$

$$\mathbf{w}_{ad}(t+1) = \mathbf{w}_{ad}(t) + \frac{\beta}{P(t+1)} \mathbf{y}_b(t) y^*(t) \quad (33)$$

We have complemented standard NLMS filter with (32), which will protect the adoption step size from taking extreme values due to rapidly varying signal values. In all our simulations the "forgetting factor" $\gamma = 0.95$ and the adoption step size $\beta = 0.000001$.

To analyze the performance of proposed algorithm we will compare desired signal recovery performance in case of various SINR-s. Beamforming algorithms under review are S-GSC algorithm proposed in section III and Robust Linearly Constrained Minimum Variance (R-LCMV) beamformer.

We will confine to stating the R-LCMV beamformer optimization problem and present the solution. A profound theory

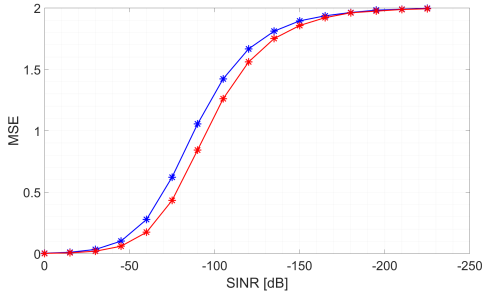


Fig. 3. Mean Square Error dependence on SINR. (R-LCMV with blue and S-GSC with red)

can be found in [11] or any other textbook dealing with beamforming problems.

The LCMV optimization problem is:

$$\begin{aligned} & \text{minimize} && \hat{\mathbf{w}}^H \mathbf{R}_{\bar{\mathbf{s}}} \hat{\mathbf{w}} \\ & \text{subject to} && \hat{\mathbf{w}}^H \mathbf{C} = \mathbf{c}^H, \end{aligned} \quad (34)$$

where $\hat{\mathbf{w}}$ is a spatial filter vector, $\mathbf{R}_{\bar{\mathbf{s}}}$ is a autocorrelation matrix of signal $\bar{\mathbf{s}}$ given by (24), matrix \mathbf{C} is a constraint matrix and vector \mathbf{c} is a response vector.

The solution to the optimization problem given by (34) is shown to be:

$$\hat{\mathbf{w}}^H = \mathbf{c}^H [\mathbf{C}^H \mathbf{R}_{\bar{\mathbf{s}}}^{-1} \mathbf{C}]^{-1} \mathbf{C}^H \mathbf{R}_{\bar{\mathbf{s}}}^{-1} \quad (35)$$

Beamformers capability to recover desired signal will be measured by means of Mean Square Error (MSE) which will found as follows:

$$\varepsilon_{ys} = \frac{1}{T} \sum_{t=0}^T (y(t) - s_d(t))^2, \quad (36)$$

where $y(t)$ is beamformers output signal, $s_d(t)$ is desired signal, t is discrete time instance and T is time period under review in current simulation $T = 10000$. Input signal is The size of an array is 50×50 .

We have conducted one hundred independent simulations for each value of SINR. During given simulation campaign there are two interfering signals present with random locations. All signals are modelled as random normally distributed processes. The averaged result are presented on Fig. 3. Blue line represents the performance of R-LCMV algorithm and red line represents the performance of S-GSC algorithm. It is evident that the S-GSC outperforms R-LCMV beamformer.

IV. SUPPRESSING UNDESIRE ADS-B MESSAGES

Thorough ADS-B system analysis has been given in [12], where authors focus primarily on the systems security aspects and point out several potential problems of the surveillance system. The biggest weakness of ADS-B lies in the RF communication link between airborne transponder and ground based receiver. Due to the openness of 1090ES protocol it is relatively easy to inject fake target reports into the system and

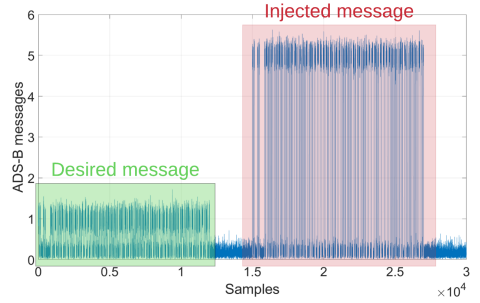


Fig. 4. Injected target message (red) and true target ADS-B message (green)

as consequence cripple air traffic control system. We will show that the proposed beamforming algorithm could potentially mitigate concerns risen.

Profound overview about the standardized surveillance systems including ADS-B using 1090ES communication technology can be found in [13] and [14]. In the context of our simulations we will look at ADS-B message as pulse train $a(t)$, with nominal pulse lengths either 0.5 (a "short" pulse) or 1 (a "long" pulse) with spaces between pulses. For the most part of the message, the positions of long and short pulses are considered random.

The simulation setup is shown on Fig. 4. There are two trailing 1090ES messages: first message is transmitted by true target and we wish to receive it. The latter message is injected with the purpose to jam the system and our aim is to suppress it. Due to the fact that the signals originate from different geographical regions, the task is easily achievable. The signal received from the AWGN (Additive White Gaussian Noise) channel with SNR $20dB$, the amplitude of desired message is 1 and the amplitude of undesired message is 5.

Actual array elements positions are normally distributed with variance $\sigma_{\text{URA}}^2 = 10^{-4}$ around their expected positions. We have factored in extra noise originating from array itself. It is modeled as an additive random Gaussian noise with variance $\sigma_{\text{th}}^2 = 0.01$.

ADS-B receiver is using 50×50 URA with S-GSC proposed in section III. The beam pattern and source locations are shown on Fig. 5. We draw readers attention to the fact that we have simulated mismatch between expected and actual sources positions.

We have chosen to use 80 Slepian sequences in the blocking branch because the energy concentration capabilities of the following DPSS-s will drop dramatically. It is worth mentioning that similar results can be obtained by using much smaller number of Slepian's in the blocking branch. But, as finding the optimal number of DPSS-s in blocking branch is not the goal of this article, we will restrain to using all the Slepian sequences witch eigenvalues are close to 1.

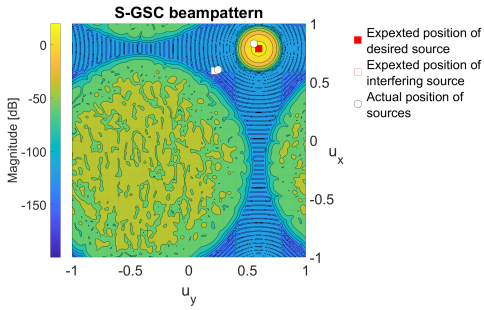


Fig. 5. S-GSC beam pattern with sources expected and actual locations.

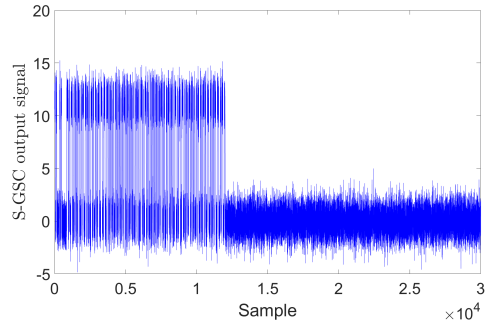


Fig. 7. S-GSC output signal.

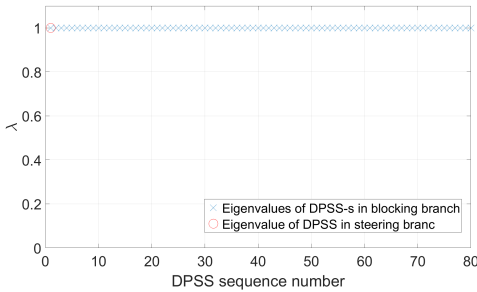


Fig. 6. Eigenvalues of used Slepian sequences.

The corresponding eigenvalues and the eigenvalue of the Slepian sequence used in steering branch is shown on Fig. 6. All the eigenvalues are close to one, meaning the energy concentration capabilities of the DPSS-s used are rather good. Confirmation of a good performance of a energy concentration to specified region can be seen on Fig. 5 – the sidelobes are much lower than the mainlobe.

The S-GSC output signal is shown on Fig. 7. One can see that we have successfully suppressed the undesired signal and the noise masks it. In the same time the desired signal is present and could easily be decoded in the following processing steps.

V. CONCLUSIONS

In this article we have proposed Robust General Sidelobe Canceller for Uniform Rectangular Array, that uses two dimensional Slepian sequences with circular spectral limitation (S-GSC). We have shown that our proposed algorithm outperforms Robust Linearly Constrained Minimum Variance (R-LCMV) beamformer in a sense that S-GSC can recover better than R-LCMV algorithm.

In the last section we have shown that proposed algorithm can suppress spitefully injected ADS-B message while amplifying message from true target.

REFERENCES

[1] M. Strohmeier, V. Lenders, and I. Martinovic, "On the security of the automatic dependent surveillance-broadcast protocol," *IEEE Communications Surveys & Tutorials*, vol. 17, no. 2, pp. 1066–1087, 2015.

[2] Y. A. Nijsure, G. Kaddoum, G. Gagnon, F. Gagnon, C. Yuen, and R. Mahapatra, "Adaptive air-to-ground secure communication system based on ads-b and wide-area multilateration," *IEEE Transactions on Vehicular Technology*, vol. 65, no. 5, pp. 3150–3165, 2016.

[3] N. Petrochilos, G. Galati, and E. Piracci, "Separation of sss signals by array processing in multilateration systems," *IEEE Transactions on Aerospace and Electronic Systems*, vol. 45, no. 3, pp. 965–982, 2009.

[4] M. Leonardi, E. Piracci, and G. Galati, "Ads-b vulnerability to low cost jammers: Risk assessment and possible solutions," in *Digital Communications-Enhanced Surveillance of Aircraft and Vehicles (TI-WDC/ESAV), 2014 Tyrrhenian International Workshop on*. IEEE, 2014, pp. 41–46.

[5] J. Li and P. Stoica, *Robust adaptive beamforming*. John Wiley & Sons, 2005, vol. 88.

[6] T. Trump, "A robust adaptive sensor array with slepian sequences," in *Sensor Array and Multichannel Signal Processing Workshop (SAM), 2012 IEEE 7th*, 2012.

[7] J. R. Guerci, "Theory and application of covariance matrix tapers for robust adaptive beamforming," *IEEE Transactions on Signal Processing*, vol. 47, no. 4, pp. 977–985, 1999.

[8] H. He and S. Kraut, "A partially adaptive beamforming with slepian-based quiescent response," in *IEEE/SP 13th Workshop on Statistical Signal Processing, 2005*. IEEE, 2005, pp. 301–306.

[9] A. Tart and T. Trump, "Robust adaptive beamforming for air surveillance system using 2d antenna array," *Proceedings of the Tyrrhenian International Workshop on Digital Communications: Enhanced Surveillance of Aircraft and Vehicles*, pp. 129 – 134, 09 2014.

[10] F. J. Simons and D. V. Wang, "Spatiospectral concentration in the cartesian plane," *GEM-International Journal on Geomathematics*, vol. 2, no. 1, pp. 1–36, 2011.

[11] H. L. Van Trees, *Optimum Array Processing*. John Wiley and Sons Inc, 2002.

[12] M. Strohmeier, M. Schafer, V. Lenders, and I. Martinovic, "Realities and challenges of nextgen air traffic management: the case of ads-b," *IEEE Communications Magazine*, vol. 52, no. 5, pp. 111–118, 2014.

[13] *Aeronautical Surveillance Manual*, First edition ed., International Civil Aviation Organization (ICAO), 2010.

[14] ICAO, *ICAO Annex 10: Aeronautical Telecommunications . Volume 4: Surveillance and Collision Avoidance Systems*, 4th ed. ICAO, 2007.

APPENDIX C

Position Report Enhancement Using Bayesian Estimator

A. Tart and T. Trump, in IEEE Aerospace and Electronic Systems Magazine, vol. 36, no. 1, pp. 4-13, 1 Jan. 2021, doi: 10.1109/MAES.2020.3015604.

Position Report Enhancement Using Bayesian Estimator

Allan Tart, OpenSky Network
Tõnu Trump, Virgostell OÜ

INTRODUCTION

Efficient direction-of-arrival (DOA) estimation is an appealing feature for many practical systems. For example, knowledge of DOA of the received signals can be exploited for source localization as well as for fast beamforming of the receiver antenna. We will give two such examples: automatic dependent surveillance—broadcast (ADS-B), an air surveillance system in air traffic management [1], and 5G, a next generation wireless communication technology [2].

Let us first turn our attention to ADS-B. It is an air surveillance system, where, along with other relevant information, aircraft broadcasts periodically its own position reports. The system works at a carrier frequency, which is equal to 1090 MHz (wavelength $\lambda \approx 0.3$ m), thus setting limitations on a viable physical size of the antenna array and, therefore, the number of elements in an array.

According to the work in [3], the data source with horizontal radius of containment $R_C \leq 0.6$ NM (1111.2 m) is allowed for aircraft maneuvering on an airport surface. One can imagine that uncertainty this large is not acceptable in practical settings. The intuition is backed up in [4], where $R_C \leq 7.5$ m is specified. In [5], Schafer *et al.* analyzed ADS-B usage and found that only a marginal part (ca. 1% in 2016) of transponders fulfill later requirements. Because of the unreliability, the ADS-B data with position accuracy category below a certain level are discarded from the sequential data processing. Instead, time difference-of-arrival (TDOA)-based surveillance systems are usually used for target localization. It relies on a spatially

distributed receiver network, where measured difference of signal time of arrival to individual receivers is exploited. Practical TDOA networks rely on the fact that the user is within a coverage of at least four base stations. This means that in complex propagation environments such as airports, the receiver network must be dense, leading to high lifecycle cost.

One could expect that over time, the percentage of compatible ADS-B transponders will rise significantly, although there will always be aircraft not fulfilling the requirements—for example, due to malfunctioning equipment. That, in turn, would forbid implementing “ADS-B only” surveillance systems.

In this article, we will show that by having target self-reported prior knowledge about the location, we can enhance report accuracy even within the case of small antenna array. This potentially can be used to reduce the number of ADS-B receivers for covering a given airport while containing the individual receiver physical antenna array size and complexity. Furthermore, we argue that ADS-B position reports, regardless of the navigation uncertainty category, are still a valuable source of information for building prior knowledge about the target location.

Next, we discuss fifth generation mobile communication (5G). Here, one of the performance enhancers is space domain multiplexing (SDM) [2]. A greatly simplified explanation of SDM is that the base station (often referred to as “gNB”) can exchange information with spatially distributed devices simultaneously. Such a system is often referred to as multiuser MIMO (MU-MIMO). When paired with emerging usage of millimeter wave (mmW), extremely high data rates can be achieved in 5G [6]. One of the performance boosters is the possibility of employing large-scale antenna arrays [7]. Later, in turn, through the use of sophisticated beamforming techniques, will allow highly directional data transmission channels to be established between transmitter-receiver pairs. It is highlighted in [8] that, due to attributes of mmW propagation (high attenuation in the environment), the control tasks, such as initial access and beam tracking, should

Authors' current address: Allan Tart is with the OpenSky Network, Burgdorf, Switzerland (e-mail: tart@opensky-network.org); Tõnu Trump is with the Virgostell OÜ, Tallinn, Estonia (e-mail: tonu.trump@gmail.com)

Manuscript received January 20, 2020, revised July 22, 2020; accepted July 27, 2020, and ready for publication August 7, 2020.

Review handled by Giancarmine Fasano.
0885-8985/21/\$26.00 © 2021 IEEE



Credit: Image licensed by Ingram Publishing

exploit antenna gains (in contrast to LTE, these tasks are carried out using an omnidirectional antenna pattern).

To be able to carry out the indicated tasks, channel state information (CSI) is needed. Much research today focuses on improving CSI estimation efficiency. As pointed out in [9], in addition to channel gain, channel matrix contains information about DOA; so being able to retrieve knowledge about transmitter location efficiently will reduce the CSI estimation effort.

A variety of different methods for estimating node positions exists in both theory and practice. Among others, TDOA-based techniques must be mentioned, which rely on spatially distributed receiver networks, where the feature, which transmitted the signal arrives in different times to receivers, is exploited. Practical TDOA networks rely on the fact that the user is within a coverage of at least four base stations. This means that in complex propagation environments with a high number of obstacles, the receiver network needs to be dense, leading to high life-cycle cost. In the 5G scenario, where potentially both source and sink need to be aware of each other's locations [8], TDOA-based systems will need extra synchronization between network nodes, adding more complexity into the system.

So called “hybrid frameworks” have been proposed, for example, in [10] and [11], where localization uses different methods (e.g., array-based DOA estimation and TDOA-based systems) simultaneously. Such systems can achieve superior position estimation accuracy when compared with using the methods individually. We see the algorithm proposed in this article as a complement to the described frameworks. Indeed, an effective and efficient DOA estimation algorithm will only improve overall hybrid system performance.

A multitude of array-based DOA estimation algorithms also exist. Based on the work in [12], for example, these can be categorized as follows:

- *beamforming methods* [e.g., maximum variance distortionless response (MVDR) beamformer];
- *subspace methods* (e.g., MUSIC);
- *parametric methods* [e.g., maximum likelihood (ML) estimator].

It is argued in [12] that one of the disadvantages of *beamforming methods* is shown to be its poor resolution performance. Whereas for *subspace methods*, such as MUSIC, the limiting factor is handling the coherence of received signals. Multipath propagation effect will result in non-orthogonal eigenvectors of the array covariance matrix, which in return will cause significant decline of algorithm performance. Another weak point of subspace methods is that it transforms a multidimensional problem into one dimension—meaning, subspace methods are capable of estimating only one parameter at a time (DOA in the given case). In the MU-MIMO case, as discussed earlier, full CSI is needed, meaning other methods need to be employed in parallel, speaking in favor of *parametric methods*. With the ML estimator as a representative example of the class of estimators, the threshold phenomenon, as described in [12] and [13], might exhibit a major problem in practical situations. The behavior of the threshold phenomenon results in sharp degradation of the estimator in the case of exceeding a certain parameter—such as SNR or resolution of targets.

In order to overcome the above-mentioned issues, arrays with a high number of antenna elements could be used. As discussed earlier, using mmW provides good opportunities for that, and a short wavelength allows us to pack antenna elements close to each while restraining the physical size of the array. In the case of ADS-B, with working frequency 1090 MHz, increasing the number of antenna elements to a comparable level with mmW systems is not viable due to the consequent physical size of an array. As discussed, for example, in [7], [8], [14]–[20] even in case mmW systems, implementing classical array processing algorithms is not a straightforward task. The problem here is twofold: computational complexity and cost- and power-consumption efficiency.

The computational complexity increases rapidly with increasing number of antenna elements. In [8], [18]–[20], different ways for reducing the complexity are proposed. They start with having a set of “predefined beams,” and the transmitter is said to be in the direction of the beam, which has the highest SNR.

With the higher number of antenna elements, the number of predefined beams increase as does the search space. Aforementioned papers propose different mechanisms to reduce the search space. For example, they make use of compressive sensing algorithms or, similar to our approach, use transmitters awareness of its location. Although the search space decreases, the array weight matrix size still needs to be high for acceptable DOA estimation accuracy.

Then, problems arise from the fact that ideally it would be possible to steer the phase of each antenna element individually, meaning each element should have its own RF chain. As argued in [7], [15]–[17], this is not efficient in terms of implementation cost and power consumption. Instead, using fewer number of RF chains is proposed in the aforementioned papers. This technique is referred to as using “hybrid arrays.” Different DOA estimation algorithms have been implemented in hybrid arrays with sufficient quality, but the solution complexity still remains high due to the array matrix size.

In this article, a maximum *a posteriori* (MAP) DOA estimation algorithm is proposed. Prior knowledge about the target location is obtained from the target itself. Indeed, the majority of receivers can determine their own position, for example, by using global navigation satellite system (GNSS). Several other possible means are discussed in [21]. In principle, the system would work in the following way:

- 1) the transmitter positions itself and transmits position data together with expected accuracy info to the receiving end;
- 2) the receiver uses the antenna array to estimate the DOA of the transmitter;
- 3) in postprocessing, the receiver DOA estimate and location information from the transmitter are combined together to produce an enhanced position report.

The scenarios of interest are illustrated in Figure 1 (ADS-B) and Figure 2 (5G).

In the ADS-B scenario, the proposed enhancement would work in the following way (see Figure 1): using any available navigational aid (usually GNSS, i.e., GPS or in some cases, ground-based systems such as VOR/DME) the aircraft determines its position and broadcasts it together with a figure of merit. The ADS-B ground station receives it and estimates the signal DOA using an antenna array. The aircraft self-declared position and ground station estimate will be combined in an optimal way to produce an enhanced position report. The enhanced position report will be delivered to the air traffic control center, where further processing will take place.

In the 5G scenario, the system enhancement (see Figure 2) works similar to ADS-B: MT uses any means available for mobile positioning (either GNSS or wireless network-based systems) and reports its location to gNB. Base station uses an array to estimate DOA of the received

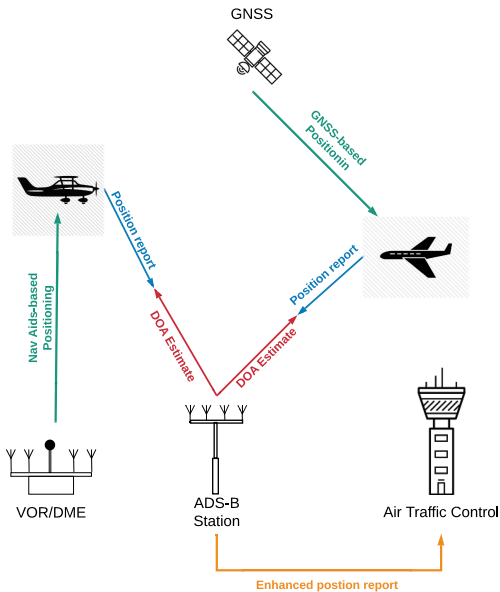


Figure 1. Target position report enhancement in ADS-B.

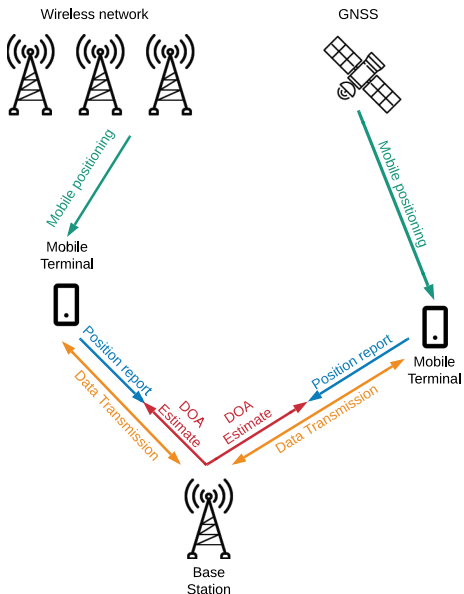


Figure 2. Mobile terminal (MT) positioning enhancement in 5G network.

signal and the two will be combined together to produce an enhanced DOA estimate. Then beamforming will take place and data transmission between MT and gNB can start.

In deriving the MAP estimator, we assume that target declared DOA follows a normal distribution with known variance and uninformative priors for signal and noise power. Although the algorithm is capable of estimating DOA, signal, and noise power, giving full information necessary to derive CSI, in this article, only DOA estimation capabilities are looked at.

We will show that by combining declared parameters and parameters derived from received signal will result in performance improvement in case of small number of array elements and large array covariance matrix error values, when comparing with ML and MUSIC algorithms.

Work presented in this article is mainly based on [13], [22], and [23]. Throughout the article, italic, bold lower case, and bold upper case letters will be used for scalars, column vectors, and matrices, respectively. The superscript T denotes transposition of a matrix, and superscript H denotes the Hermitian transposition of a matrix. Identity matrix is denoted as \mathbf{I} ; trace of a matrix is written as $\text{Tr}(\cdot)$. We will use $|\cdot|$ to denote L_1 norm of a vector and $\|\cdot\|$ to denote L_2 norm of a vector and $\|\cdot\|_F$ to denote Frobenius norm of a matrix. Subscripts o and p generally denote o, p th element of given matrix. The size of a matrix is arbitrary and will be specified where appropriate. Symbol \propto is used to indicate that expression on the right-hand side is proportional to the variable on the left hand.

PROBLEM STATEMENT

Let us consider the situation, where we have Q point sources, transmitting narrow-band signals $\bar{s}_q(t)$, with $q = 1, \dots, Q$. It is assumed that the number of targets Q is known. Throughout the article, the discrete signal model is used, i.e., $\bar{s}_q(t)$ denotes signal \bar{s} , transmitted by q th source at integer valued time index t . We can represent the signals from all the sources in a vector form in the following way: $\bar{\mathbf{s}}_t = [\bar{s}_1(t), \dots, \bar{s}_q(t), \dots, \bar{s}_Q(t)]^T$. In the context of this work, it is assumed that mean value of $\bar{s}_q(t)$ is zero, i.e., $E[\bar{s}_q(t)] = 0$, power of q th signal is $\bar{\sigma}_q^2 = E[\bar{s}_q^2(t)]$ and source signal covariance matrix is defined as $\mathbf{C}_s = E[\bar{\mathbf{s}}_t \bar{\mathbf{s}}_t^H]$. As the source signals are independent, \mathbf{C}_s is a diagonal matrix with nonzero elements only on the main diagonal, which are equal to respective signal power, i.e., $\text{diag}(\mathbf{C}_s) = \bar{\boldsymbol{\sigma}}_s^2 = [\bar{\sigma}_1^2, \dots, \bar{\sigma}_q^2, \dots, \bar{\sigma}_Q^2]$.

The content of messages forwarded by q th source is the target's declared position and some parameter describing an accuracy of the transmitted position report. These

parameters can be used to deduce the targets declared DOA $\varphi_{D,q}$ and its variance $\sigma_{\Delta,q}^2$.

Before moving forward, attention must be drawn to the fact that without an explicit reference *electrical* DOA θ is used instead of the *actual* DOA φ . The relation between these two is $\theta = \pi \sin(\varphi)$.

The declared DOA $\theta_{D,q}$ and the true DOA $\bar{\theta}_q$ differ from each other by Δ_q —meaning $\bar{\theta}_q = \theta_{D,q} + \Delta_q$. For convenience of the notation, we will gather parameters into vectors and reveal relation between declared and actual DOAs in the following way:

$$\bar{\boldsymbol{\theta}} = \boldsymbol{\theta}_D + \boldsymbol{\Delta} \quad (1)$$

where $\boldsymbol{\theta}_D = [\theta_{D,1}, \dots, \theta_{D,q}, \dots, \theta_{D,Q}]^T$, $\bar{\boldsymbol{\theta}} = [\bar{\theta}_1, \dots, \bar{\theta}_q, \dots, \bar{\theta}_Q]^T$, and $\boldsymbol{\Delta} = [\Delta_1, \dots, \Delta_q, \dots, \Delta_Q]^T$. Variances of declared DOAs are also gathered into vector $\boldsymbol{\sigma}_\Delta^2$, i.e., $\boldsymbol{\sigma}_\Delta^2 = [\sigma_{\Delta,1}^2, \dots, \sigma_{\Delta,q}^2, \dots, \sigma_{\Delta,Q}^2]^T$.

The target position is derived from well-established navigation system (e.g., GPS) and according to the work in [24], it is appropriate to assume that true DOA is distributed normally, i.e., $\bar{\boldsymbol{\theta}} \sim \mathcal{N}(\boldsymbol{\theta}_D, \mathbf{C}_D)$.

The uniform linear array containing M omnidirectional antenna elements is used to receive the signal. The steering vector \mathbf{v} for q th source is given by

$$\mathbf{v}(\bar{\theta}_q) = \begin{bmatrix} 1 \\ \exp(j\bar{\theta}_q) \\ \vdots \\ \exp(jm\bar{\theta}_q) \\ \vdots \\ \exp(j(M-1)\bar{\theta}_q) \end{bmatrix}. \quad (2)$$

For the sake of simplifying the notations, steering vectors are gathered into matrix $\mathbf{V}_{\bar{\boldsymbol{\theta}}}$

$$\mathbf{V}_{\bar{\boldsymbol{\theta}}} = [\mathbf{v}(\bar{\theta}_1), \mathbf{v}(\bar{\theta}_2), \dots, \mathbf{v}(\bar{\theta}_q), \dots, \mathbf{v}(\bar{\theta}_Q)]. \quad (3)$$

Having $\bar{\mathbf{s}}_t$ and $\mathbf{V}_{\bar{\boldsymbol{\theta}}}$, the snapshot of received signal \mathbf{x}_t on different antennas can be unveiled

$$\mathbf{x}_t = \mathbf{V}_{\bar{\boldsymbol{\theta}}} \bar{\mathbf{s}}_t + \mathbf{n}_t. \quad (4)$$

Noise vector is defined as $\mathbf{n}_t = [n_1, \dots, n_m, \dots, n_M]^T$ and it captures the distortions at time instance t resulted by the array imperfections and additive noise from transmission chain. Elements in \mathbf{n}_t are independent, normally distributed with mean $\mu_n = 0$ and variance $\bar{\sigma}_n^2$.

The probability density function (pdf) of \mathbf{x}_t follows the multivariate normal distribution, i.e., $\mathbf{x}_t \sim \mathcal{N}(\mathbf{0}, \mathbf{C}_x)$, where \mathbf{C}_x , data covariance matrix, is unknown. In general, the relationship between \mathbf{C}_x , steering matrix $\mathbf{V}_{\bar{\boldsymbol{\theta}}}$, signal covariance matrix $\boldsymbol{\sigma}^2$, and noise variance $\bar{\sigma}_n^2$ is

$$\mathbf{C}_x = \mathbf{V}_{\bar{\boldsymbol{\theta}}} \mathbf{C}_s \mathbf{V}_{\bar{\boldsymbol{\theta}}}^H + \bar{\sigma}_n^2 \mathbf{I}. \quad (5)$$

In short, the task in hand is to find $\bar{\theta}$ while having array signal samples \mathbf{x}_t and θ_D together with their respective PDF-s.

The unknown parameters $\bar{\theta}$, $\bar{\sigma}^2$, and $\bar{\sigma}_n^2$ are gathered into vector $\bar{\mathbf{a}}$ in the following way:

$$\bar{\mathbf{a}} = \begin{bmatrix} \bar{\theta} \\ \bar{\sigma}^2 \\ \bar{\sigma}_n^2 \end{bmatrix}. \quad (6)$$

After reformulating the problem, our task now is to find estimate $\hat{\mathbf{a}}$, which is as close to $\bar{\mathbf{a}}$ as possible.

MAP ESTIMATOR

In this section, the MAP estimator for finding the target DOA, received signal, and noise powers is found.

Let us proceed by giving a well-known Bayesian equation for *a posteriori* pdf

$$p(\mathbf{a}|\mathbf{x}_t) = \frac{p(\mathbf{a})p(\mathbf{x}_t|\mathbf{a})}{p(\mathbf{x}_t)}. \quad (7)$$

The unknown \mathbf{a} vector is given by

$$\mathbf{a} = \begin{bmatrix} \theta \\ \sigma_s^2 \\ \sigma_n^2 \end{bmatrix}. \quad (8)$$

Let us continue by revealing different terms of (7). First, our focus is set on prior pdf $p(\mathbf{a})$

$$p(\mathbf{a}) = p(\theta)p(\sigma_s^2)p(\sigma_n^2). \quad (9)$$

In the current treatment, noninformative priors for signal and noise variances are used. That is, $p(\sigma_s^2) = 1$ and $p(\sigma_n^2) = 1$, yielding $p(\mathbf{a}) = p(\theta)$.

As argued in [24] and pointed out earlier, it is a sensible assumption that the prior pdf of DOA is multivariate Gaussian

$$p(\theta) = (2\pi)^{-Q/2} \det(\mathbf{C}_D)^{-1/2} \cdot \exp(-0.5(\theta - \theta_D)^T \mathbf{C}_D^{-1}(\theta - \theta_D)) \quad (10)$$

and data likelihood function is

$$\begin{aligned} p(\mathbf{x}_t|\mathbf{a}) &= \\ &= (2\pi)^{-M/2} \det(\mathbf{C}_x)^{-1/2} \\ &\quad \cdot \exp(-0.5\mathbf{x}_t^H \mathbf{C}_x^{-1} \mathbf{x}_t) \\ &= (2\pi)^{-M/2} \det(\mathbf{C}_x)^{-1/2} \\ &\quad \cdot \exp(-0.5\text{Tr}(\mathbf{R}_x \mathbf{C}_x^{-1})) \end{aligned} \quad (11)$$

where we have defined $\mathbf{R}_x = E[\mathbf{x}_t \mathbf{x}_t^H]$. The marginal likelihood $p(\mathbf{x}_t)$ is given by

$$p(\mathbf{x}_t) = \int_{\mathcal{A}} p(\theta)p(\mathbf{x}_t|\mathbf{a})d\mathbf{a} \quad (12)$$

where \mathcal{A} is the domain of \mathbf{a} . In the context of the MAP estimator, marginal likelihood function does not play any role and, therefore, is discarded from the following computations.

Having the above, the MAP estimator is defined as the following optimization problem:

$$\hat{\mathbf{a}} = \arg \max_{\mathbf{a}} [\ln p(\theta) + \ln p(\mathbf{x}_t|\mathbf{a})]. \quad (13)$$

To get a DOA estimate, we need to solve the following equation:

$$E[d \ln p(\theta) + d \ln p(\mathbf{x}_t|\mathbf{a})] = 0. \quad (14)$$

For simplifying the notations, we will reformulate the task by discarding terms in log-likelihood expressions that do not depend on \mathbf{a} . We will be left with the following:

$$\ln p(\theta) \propto \lambda(\theta) = (\theta - \theta_D)^T \mathbf{C}_D^{-1}(\theta - \theta_D) \quad (15)$$

and

$$\ln p(\mathbf{x}_t|\mathbf{a}) \propto \kappa(\mathbf{a}) = \ln \det(\mathbf{C}_x) + \text{Tr}(\mathbf{R}_x \mathbf{C}_x^{-1}). \quad (16)$$

The problem now writes

$$\hat{\mathbf{a}} = \arg \min_{\mathbf{a}} [\lambda(\mathbf{a}) + \kappa(\mathbf{a})]. \quad (17)$$

A set of example criterion functions for variety of SNR-s is shown in Figure 3. Here, signal and noise powers have been fixed and only DOA is used as a variable to illustrate $\lambda(\mathbf{a}) + \kappa(\mathbf{a})$.

The graph illustrates $\lambda(\mathbf{a}) + \kappa(\mathbf{a})$ dependence on SNR—higher SNR shifts global minimum toward true DOA and in case of low-SNR global minimum moves closer to declared DOA. This is in line with the results given in [13], [22], and [23]. It must be noted that for this purpose in Figure 3, true covariance matrix \mathbf{C}_x as defined in (5) is used.

MINIMA OF THE CRITERION FUNCTION

For finding the criterion function minimum, the grid search would be a viable choice in case of only DOA for one target is to be estimated. In current case, the number of unknown variables in $2Q + 1$, this will make it unwieldy. Therefore, we are using a gradient-based

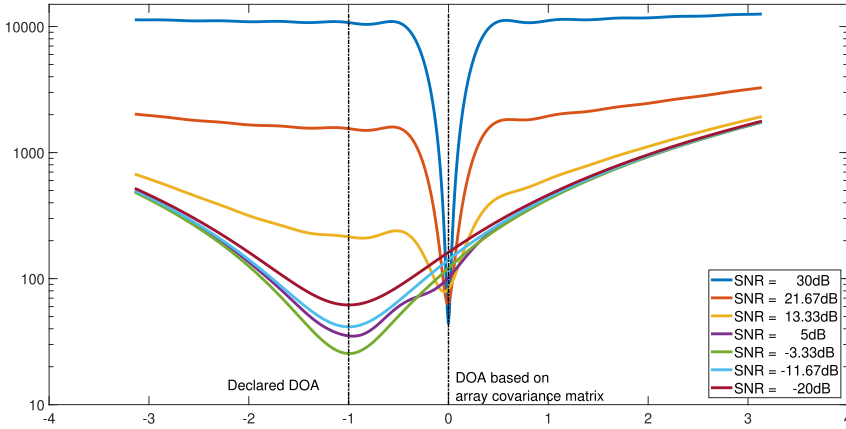


Figure 3.

Set of criterion functions in case of different SNR-s. True covariance matrix \mathbf{C}_x is used.

algorithm, namely *Newton's method*, which is widely used for solving similar problems.

Using the gradient-based method for finding criteria function minima means that the estimator is defined as a solution to the following system of equations:

$$d\lambda(\mathbf{a}) + d\kappa(\mathbf{a}) = 0. \quad (18)$$

The first step in revealing the estimator is finding the partial derivatives of λ

$$\frac{\partial \lambda}{\partial \theta} = -\mathbf{C}_D^{-1}(\boldsymbol{\theta} - \boldsymbol{\theta}_D) \quad (19)$$

$$\frac{\partial \lambda}{\partial \sigma_s^2} = 0 \quad (20)$$

$$\frac{\partial \lambda}{\partial \sigma_n^2} = 0. \quad (21)$$

Next, moving on to finding $d\kappa$. According to the work in [25], the derivatives of addends of (16) are given by

$$d \ln \det(\mathbf{C}_x) = \text{Tr}(\mathbf{C}_x^{-1} d\mathbf{C}_x) \quad (22)$$

and

$$d \text{Tr}(\mathbf{R}_x \mathbf{C}_x^{-1}) = -\text{Tr}(\mathbf{C}_x^{-1} \mathbf{R}_x \mathbf{C}_x^{-1} d\mathbf{C}_x). \quad (23)$$

Next, partial derivatives of covariance matrix \mathbf{C}_x . First, $\frac{\partial}{\partial \theta} \mathbf{C}_x$ will give Q equations, where, in general, the individual elements are given by

$$[\tilde{\mathbf{C}}_{\theta,q}]_{o,p} = \frac{\partial}{\partial \theta_q} [\mathbf{C}_x]_{o,p} = j\sigma_q^2(p-o)\exp(j(p-o)\theta_q). \quad (24)$$

Second, $\frac{\partial}{\partial \sigma^2} \mathbf{C}_x$ will also give Q equations, where, in general, the individual elements are given by

$$[\tilde{\mathbf{C}}_{\sigma,q}]_{o,p} = \frac{\partial}{\partial \sigma_q^2} [\mathbf{C}_x]_{o,p} = \exp(j(p-o)\theta_q). \quad (25)$$

In (24) and (25), $(o,p) = 1, \dots, Q$. Finally, $\frac{\partial}{\partial \sigma_n^2} \mathbf{C}_x$ will give

$$\frac{\partial}{\partial \sigma_n^2} \mathbf{C}_x = \mathbf{I}. \quad (26)$$

As a next step, an equation system is constructed. Starting with vector yielding from $\frac{\partial}{\partial \theta}(\lambda + \kappa)$

$$c_q(\mathbf{a}) = -\text{Tr}(\mathbf{C}_x^{-1} \mathbf{R}_x \mathbf{C}_x^{-1} \tilde{\mathbf{C}}_{\theta,q}) + \frac{2}{\sigma_{\Delta,q}^2}(\theta_q - \theta_{D,q}). \quad (27)$$

Gathering equations into vector $\mathbf{c}(\mathbf{a})$ yields

$$\mathbf{c}(\mathbf{a}) = [c_1, \dots, c_q, \dots, c_Q]^T. \quad (28)$$

Next, equations from $\frac{\partial}{\partial \sigma_s^2}(\lambda + \kappa)$:

$$d_q(\mathbf{a}) = -\text{Tr}(\mathbf{C}_x^{-1} \mathbf{R}_x \mathbf{C}_x^{-1} \tilde{\mathbf{C}}_{\sigma,q}) + \text{Tr}(\mathbf{C}_x^{-1} \tilde{\mathbf{C}}_{\sigma,q}). \quad (29)$$

Gathering equations into vector $\mathbf{d}(\mathbf{a})$ yields

$$\mathbf{d}(\mathbf{a}) = [d_1, \dots, d_q, \dots, d_Q]^T. \quad (30)$$

And finally, the equation from $\frac{\partial}{\partial \sigma_n^2}(\lambda + \kappa)$

$$g(\mathbf{a}) = -\text{Tr}(\mathbf{C}_x^{-1} \mathbf{R}_x \mathbf{C}_x^{-1}) + \text{Tr}(\mathbf{C}_x^{-1}). \quad (31)$$

We can arrange vectors from (28), (30), and (31) together into vector $\mathbf{f}(\mathbf{a})$ in the following way:

$$\mathbf{f}(\mathbf{a}) = \begin{bmatrix} \mathbf{c}(\mathbf{a}) \\ \mathbf{d}(\mathbf{a}) \\ g(\mathbf{a}) \end{bmatrix}. \quad (32)$$

This will give us a system with $2Q + 1$ equations, which needs to be solved for finding estimate $\hat{\mathbf{a}}$

$$\mathbf{f}(\hat{\mathbf{a}}) \approx \mathbf{0}. \quad (33)$$

Equation (33) does not have closed form analytic solution, and therefore, a numerical method need be employed. We will again turn to Newton's method for finding the roots, but any other method might potentially be used.

NEWTON'S METHOD

As Newton's method is well known, following the work in [26], we will merely give the approximation update rule

$$\hat{\mathbf{a}}_{i+1} = \hat{\mathbf{a}}_i - \mu \mathbf{J}^{-1} \mathbf{f}(\hat{\mathbf{a}}_i) \quad (34)$$

where i is a iteration index and \mathbf{J} is $(2Q + 1) \times (2Q + 1)$ Jacobian matrix and its o, p th element is given by

$$[\mathbf{J}]_{o,p} = \frac{\partial f_o(\hat{\mathbf{a}})}{\partial \hat{a}_p}. \quad (35)$$

The step size in (34) will determine a stopping criteria— L_1 norm of a step-size vector must be smaller than η

$$|\mu \mathbf{J}^{-1} \mathbf{f}(\hat{\mathbf{a}}_i)| < \eta. \quad (36)$$

In (35), the partial derivatives are found numerically

$$\frac{\partial f_o(\hat{\mathbf{a}})}{\partial \hat{a}_p} = \frac{f_o(\Delta \mathbf{a}_p^+) - f_o(\Delta \mathbf{a}_p^-)}{2h_p} \quad (37)$$

where $\Delta \mathbf{a}_p^+$ and $\Delta \mathbf{a}_p^-$ are versions of $\hat{\mathbf{a}}$, where p th element has changed by h_p and $-h_p$, respectively, i.e.,

$$\Delta \mathbf{a}_p^+ : [\hat{\mathbf{a}}]_p = a_p + h_p \quad \Delta \mathbf{a}_p^- : [\hat{\mathbf{a}}]_p = a_p - h_p.$$

Initial guess \mathbf{a}_0 . It is well known that the choice of a good starting point in Newton's method is crucial. If badly selected, one of two things might happen: a) the solution will not converge or b) solution converges to local

extreme point. To avoid this phenomenon, P starting points are chosen, so we will have $2Q + 1 \times P$ matrix \mathbf{A} containing starting points

$$\mathbf{A} = [\mathbf{a}_{0,1}, \dots, \mathbf{a}_{0,p}, \dots, \mathbf{a}_{0,P}] \quad (38)$$

where $\mathbf{a}_{0,p} = \mathbf{a}_{0,1} + \mathbf{w}$, with $\mathbf{w} \sim \mathcal{N}(\mathbf{0}, \mathbf{C}_w)$. Covariance matrix \mathbf{C}_w is diagonal matrix $\mathbf{C}_w = \text{diag}[\alpha \sigma_\Delta^2, \mathbf{1}, \mathbf{1}]$ with size $2Q + 1 \times 2Q + 1$ and parameter $\alpha \geq 1$ will assure sufficiently large search area around the initial guess to assure algorithm convergence.

At convergence, the one yielding minimum value of $\lambda + \kappa$ will be taken as a solution. If none of the solutions converge (i.e., $\det(\mathbf{J}) \rightarrow 0$) for all starting points in \mathbf{A} , estimated DOA will be set N/A .

ROOT MUSIC AND ML ESTIMATOR

In this section, a short overview of Root MUSIC and ML is given. We will use those popular DOA estimation algorithms later as baseline to the purposed MAP estimator.

ROOT MUSIC

In this article, we will confine ourselves to giving the results presented in [13].

The first step is to perform a eigendecomposition of $\hat{\mathbf{R}}_x$ yielding

$$\hat{\mathbf{R}}_x = \Phi \mathcal{V} \Phi^{-1} \quad (39)$$

where $\mathcal{V} = \text{diag}[v_1, \dots, v_M]$ is a diagonal matrix containing eigenvalues and $\Phi = [\phi_1, \dots, \phi_M]$ corresponding eigenvectors of $\hat{\mathbf{R}}_x$. Assuming that eigenvalues in \mathcal{V} are aligned in an ascending order, first $M - Q$ eigenvalues can be referred to as noise subspace eigenvalues and last Q columns in Φ as signal-subspace eigenvectors. Noise subspace is defined as \mathbf{U}_n

$$\mathbf{U}_n = [\phi_1, \phi_2, \dots, \phi_{M-Q}]. \quad (40)$$

Having (40), we can define so called null-space spectrum function $\mathcal{F}(\theta)$

$$\mathcal{F}(\theta) = \frac{1}{\mathbf{v}^H(\theta) (\mathbf{U}_n \mathbf{U}_n^H) \mathbf{v}(\theta)}. \quad (41)$$

Defining $\mathbf{U} = \mathbf{U}_n \mathbf{U}_n^H$, we can rewrite (41)

$$\begin{aligned} \mathbf{v}^H(\theta) \mathbf{U} \mathbf{v}(\theta) &= \sum_{o=0}^{M-1} \sum_{p=0}^{M-1} u_{o,p} \exp(j(p-o)\theta) \\ &= \sum_{l=-M+1}^{M-1} U_l \exp(jl\theta) \end{aligned} \quad (42)$$

where U_l is the sum of the elements of along the l th diagonal of \mathbf{U} .

Table 1.

Simulation Parameters	
Parameter	Value
<i>Target and Array Parameters:</i>	
Array size	$M = 5$
Number of signal samples	$T = 1, 2, 3, \dots, 25$
Number of targets	$Q = 2$
True signal power	$\overline{\sigma_s^2} = [1, 1]^T$
True noise power	$\sigma_n^2 = (0.5, 1, 2)$
True DOA	$\overline{\theta} = [1.5, 1.3]^T$
Declared DOAs for targets	$\theta_D \sim \mathcal{N}(\overline{\theta}, \text{diag}(\sigma_\Delta^2))$
Variance of declared DOA	$\sigma_\Delta^2 = [0.05, 0.05]$
<i>Newton Method Parameters:</i>	
Step size guard	$\mu = 0.0625$
Stopping criteria	$\eta = 10^{-5}$
Max number of iterations	10 000
Number of initial starting points	$P = 30$
Search area parameter	$\alpha = 5$
Numerical derivative step size	$h = 0.01$

The Q roots of (42), which lie closest to unit circle, correspond to desired DOAs. In current setup, all roots are computed and the ones inside the unit circle, whose magnitude is closest to 1, will choose to find the DOAs.

Note that $\mathcal{F}(\theta)$ is one-dimensional function and we no longer need to search over $2Q + 1$ dimensional space.

ML ESTIMATOR

MAP and ML estimators are rather similar. The difference between the two is the absence of *a priori* knowledge about the unknown variables in ML. We, therefore, can state that the ML estimate is the solution to the following minimization problem:

$$\hat{\mathbf{a}}_{ml} = \arg \min_{\mathbf{a}} [\kappa(\mathbf{a})] \quad (43)$$

which will be found by solving

$$d\kappa(\mathbf{a}) = 0. \quad (44)$$

Similar to the MAP estimator, Newton's method will be used for finding the roots of $\kappa(\mathbf{a})$. For that, the

following equation system needs to be solved:

$$\tilde{\mathbf{f}}(\mathbf{a}) = \begin{bmatrix} \tilde{\mathbf{c}}(\mathbf{a}) \\ \mathbf{d}(\mathbf{a}) \\ g(\mathbf{a}) \end{bmatrix}. \quad (45)$$

Vectors $\mathbf{d}(\mathbf{a})$ and variable $g(\mathbf{a})$ are given by (29)–(31).

$\tilde{\mathbf{c}}(\mathbf{a})$ is given by the following:

$$\tilde{c}_q(\mathbf{a}) = -\text{Tr}(\mathbf{C}_x^{-1} \mathbf{R}_x \mathbf{C}_x^{-1} \tilde{\mathbf{C}}_{\theta, \mathbf{a}}) \quad (46)$$

and

$$\tilde{\mathbf{c}}(\mathbf{a}) = [\tilde{c}_1, \dots, \tilde{c}_q, \dots, \tilde{c}_Q]^T. \quad (47)$$

The minima of $\mathbf{f}(\tilde{\mathbf{a}})$ is found by using Newton's method, as described earlier.

SIMULATION TRIALS

In this section, the results of numerical simulation trials of the proposed algorithm are given. Together with the proposed estimator, the results for other popular estimation schemes are provided. This includes MUSIC and ML algorithms.

As the target DOA is the principle variable we are interested in, the estimators capability to reveal signal and noise powers is neglected. The estimators performance is presented as the average MSE of both DOAs, i.e., $\frac{1}{2} \sum_{q=1}^2 \|\hat{\theta}_q - \theta_q\|_2^2$

We will look at the case where number of array elements M and the number of signal samples for estimating the array covariance matrix \mathbf{R}_x is small. Potentially it will allow us to use less complex receivers for DOA estimation. The list parameter values used in the simulation trials are given in Table 1.

In the simulations, the sample covariance matrix $\hat{\mathbf{R}}$ is used to find $\mathbf{R}_x = E[\mathbf{x}\mathbf{x}^H]$. Former is defined by the following equation:

$$\hat{\mathbf{R}}_x = \frac{1}{T} \mathbf{X}\mathbf{X}^H \quad (48)$$

where $\mathbf{X} = [\mathbf{x}_0, \dots, \mathbf{x}_t, \dots, \mathbf{x}_T]$ is a $M \times T$ matrix containing T snapshots of signal received signal \mathbf{x} .

In this article, Frobenius norm $\|\hat{\mathbf{R}} - \mathbf{R}\|_F$ is used to measure the difference between the two matrices. The Frobenius norm dependence on signal samples and SNR is shown in Figure 4.

In current simulation trial, the sample covariance matrix is constructed by drawing random samples following the Wishart pdf with the following parameters $\mathcal{W}_M(\mathbf{C}_x, T)$. By doing so, we avoid explicitly generating \mathbf{X} . Justification of doing so is given in [13].

The simulation results are shown in Figure 5. It is evident that in case of extremely unfavorable situation of

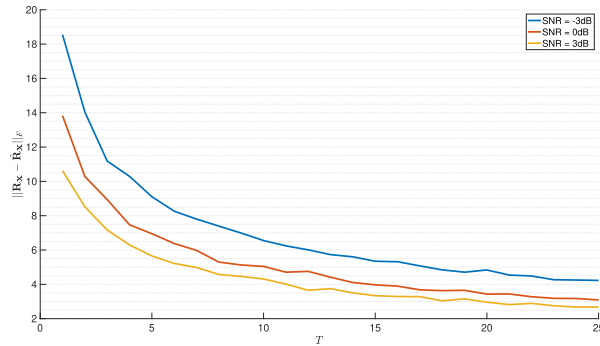


Figure 4.
 $\|\hat{\mathbf{R}} - \mathbf{R}\|_F$ dependence on number of signal samples T and SNR.

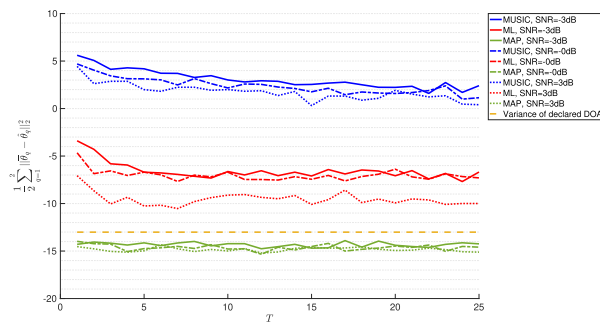


Figure 5.
 MSE dependence on number of signal samples T .

having small array size (five elements) and large sample covariance matrix error (varying from about 2.5 dB up to about 19 dB), the MAP estimator is the only one capable of improving the prior knowledge. In case of the declared variance being -13 dB, the MAP estimate is capable improving the declared position estimate by 2 dB in case SNR = 3 dB.

CONCLUSION

In this article, the target position report enhancement algorithm was proposed. The algorithm is based on the MAP estimator and uses the target position report as a prior knowledge. The proposed method was compared with other popular estimation algorithms, namely with the ML and MUSIC algorithms. In the case of the extremely unfavorable situation of having small array size and large sample covariance matrix error, MAP is the only algorithm capable of improving the prior knowledge about the target position. Hence, using the MAP estimator, we can loosen the requirements on the receiver hardware by means of lowering the number of array elements and allowing a higher receiver noise figure.

REFERENCES

- [1] M. Strohmeier, M. Schäfer, V. Lenders, and I. Martinovic, "Realities and challenges of nextgen air traffic management: The case of ADS-B," *IEEE Commun. Mag.*, vol. 52, no. 5, pp. 111–118, May 2014.
- [2] F. Boccardi, R. W. Heath, A. Lozano, T. L. Marzetta, and P. Popovski, "Five disruptive technology directions for 5G," *IEEE Commun. Mag.*, vol. 52, no. 2, pp. 74–80, Feb. 2014.
- [3] *Minimum Operational Performance Standards (MOPS) for 1090 MHz Extended Squitter Automatic Dependent Surveillance-Broadcast (ADS-B) and Traffic Information Services-Broadcast (TIS-B)*, R.F.SC-186, RTCA, Inc., Washington, DC, USA, 2011.
- [4] Organization de L'Aviation Civile Internationale, *Advanced Surface Movement Guidance and Control Systems (A-SMGCS) Manual*, ICAO, Montreal, QC, Canada, 2004.
- [5] M. Schäfer *et al.*, "OpenSky report 2016: Facts and figures on SSR mode S and ADS-B usage," in *Proc. IEEE/AIAA 35th Digit. Avionics Syst. Conf.*, 2016, pp. 1–9.
- [6] T. S. Rappaport *et al.*, "Millimeter wave mobile communications for 5G cellular: It will work!" *IEEE Access*, vol. 1, pp. 335–349, 2013.

- [7] A. Puglielli *et al.*, “Design of energy- and cost-efficient massive MIMO arrays,” *Proc. IEEE*, vol. 104, no. 3, pp. 586–606, Mar. 2016.
- [8] M. Giordani, M. Polese, A. Roy, D. Castor, and M. Zorzi, “A tutorial on beam management for 3GPP NR at mmWave frequencies,” *IEEE Commun. Surv. Tut.*, vol. 21, no. 1, pp. 173–196, Jan.–Mar. 2019.
- [9] D. Tse and P. Viswanath, *Fundamentals of Wireless Communication*. Cambridge, U.K.: Cambridge Univ. Press, 2005.
- [10] J. Chen and A. Abedi, “A hybrid framework for radio localization in broadband wireless systems,” in *Proc. IEEE Global Telecommun. Conf.*, 2010, pp. 1–6.
- [11] T. Sanchez, R. C. Hincapie, and C. Gomez, “Performance study of localization techniques: Hybrid vs. non hybrid TDOA/DOA,” in *Proc. IEEE-APS Topical Conf. Antennas Propag. Wireless Commun.*, 2018, pp. 957–960.
- [12] P.-J. Chung, M. Viberg, and J. Yu, “DOA estimation methods and algorithms,” in *Academic Press Library in Signal Processing: Volume 3: Array and Statistical Signal Processing*, A. M. Zoubir, M. Viberg, R. Chellappa, and S. Theodoridis, Eds. Amsterdam, The Netherlands: Elsevier, 2014, ch. 14, pp. 599–650. [Online]. Available: <http://www.sciencedirect.com/science/article/pii/B978012411597200014X>
- [13] H. L. Van Trees, *Optimum Array Processing: Part IV of Detection, Estimation, and Modulation Theory*. Hoboken, NJ, USA: Wiley, 2004.
- [14] M. Wang, F. Gao, S. Jin, and H. Lin, “An overview of enhanced massive MIMO with array signal processing techniques,” *IEEE J. Sel. Topics Signal Process.*, vol. 13, no. 5, pp. 886–901, Sep. 2019.
- [15] F. Sohrabi and W. Yu, “Hybrid digital and analog beamforming design for large-scale antenna arrays,” *IEEE J. Sel. Topics Signal Process.*, vol. 10, no. 3, pp. 501–513, Apr. 2016.
- [16] Z. Ni, J. A. Zhang, K. Yang, F. Gao, and J. An, “Estimation of multiple angle-of-arrivals with localized hybrid subarrays for millimeter wave systems,” *IEEE Trans. Commun.*, vol. 68, no. 3, pp. 1897–1910, Mar. 2020.
- [17] S. Chuang, W. Wu, and Y. Liu, “High-resolution AoA estimation for hybrid antenna arrays,” *IEEE Trans. Antennas Propag.*, vol. 63, no. 7, pp. 2955–2968, Jul. 2015.
- [18] A. Shahmansoori, G. E. Garcia, G. Destino, G. Seco-Granados, and H. Wymeersch, “Position and orientation estimation through millimeter-wave MIMO in 5G systems,” *IEEE Trans. Wireless Commun.*, vol. 17, no. 3, pp. 1822–1835, Mar. 2018.
- [19] N. Garcia, H. Wymeersch, E. G. Ström, and D. Slock, “Location-aided mm-Wave channel estimation for vehicular communication,” in *Proc. IEEE 17th Int. Workshop Signal Process. Adv. Wireless Commun.*, 2016, pp. 1–5.
- [20] M. S. Sim, Y. Lim, S. H. Park, L. Dai, and C. Chae, “Deep learning-based mmwave beam selection for 5G NR/6G with sub-6 GHz channel information: Algorithms and prototype validation,” *IEEE Access*, vol. 8, pp. 51634–51646, 2020.
- [21] R. Di Taranto, S. Muppirisetty, R. Raulefs, D. Slock, T. Svensson, and H. Wymeersch, “Location-aware communications for 5G networks: How location information can improve scalability, latency, and robustness of 5G,” *IEEE Signal Process. Mag.*, vol. 31, no. 6, pp. 102–112, Nov. 2014.
- [22] S. M. Kay, *Fundamentals of Statistical Signal Processing: Estimation Theory*. Upper Saddle River, NJ, USA: Prentice Hall, 1993.
- [23] A. Gelman, H. S. Stern, J. B. Carlin, D. B. Dunson, A. Vehtari, and D. B. Rubin, *Bayesian Data Analysis*. London, U.K.: Chapman & Hall, 2013.
- [24] N. Zhu, J. Marais, D. Bétaille, and M. Berbineau, “GNSS position integrity in urban environments: A review of literature,” *IEEE Trans. Intell. Transp. Syst.*, vol. 19, no. 9, pp. 2762–2778, Sep. 2018.
- [25] A. Hjørungnes, *Complex-Valued Matrix Derivatives: With Applications in Signal Processing and Communications*. Cambridge, U.K.: Cambridge Univ. Press, 2011.
- [26] G. Dahlquist and A. Björck, *Numerical Methods in Scientific Computing: Volume 1*. Philadelphia, PA, USA: SIAM, 2008.

APPENDIX D

Robust Adaptive Beamforming for Air Surveillance System using 2D Antenna Array

A. Tart and T. Trump, 2014 Tyrrhenian International Workshop on Digital Communications - Enhanced Surveillance of Aircraft and Vehicles (TIWDC/ESAV), Rome, Italy, 2014, pp. 110-115, doi: 10.1109/TIWDC-ESAV.2014.6945459.

ROBUST ADAPTIVE BEAMFORMING FOR SURVEILLANCE SYSTEM USING 2D ANTENNA ARRAY

Allan Tart and Tõnu Trimp

Tallinn University of Technology
Department of Radio and Communication Engineering
Ehitajate tee 5, Tallinn, 19086, Estonia

ABSTRACT

In this paper we propose an algorithm for 2D antenna array that can be used in ground surveillance systems. Due to the multipath propagation of signals robustness against imperfect knowledge about direction of arrival (DOA) is needed. We achieve the needed robustness by using two dimensional Slepian window functions. Although main interest of our research is surveillance, results of it may be also implemented in other domains of CNS (communication, navigation and surveillance). It is so because relatively similar nature of the systems – they all exchange data between avionics and ground based systems.

1. INTRODUCTION

One of the weak points of any surveillance system, capable of exchanging data, is that they do not contain any channel access mechanisms. It is especially crucial in ground surveillance, where multipath propagation of signal adds complexity to the overall system. From one hand degarbling of the transponder reply signals must be performed. Methods based on blind source separation has been proposed previously (e.g. in [2]) and they prove to be better on performing given task than adaptive beamforming does. On the other hand, very accurate pulse leading edge detection is needed for aircraft's position determinations. Due to the multipath effect as already mentioned, adaptive beamforming (or "smart antennas" as proposed in [3]) are expected to perform better than blind source separation algorithms.

In this paper we propose a adaptive beamforming algorithm based on Generalized Sidelobe Canceller where imperfect knowledge about direction of arrival is allowed. This is achieved by using Discrete Prolate Spheroidal Windows (DPSW), also often referred to as Slepian sequences. Compared with previous works (e.g. [4]) we have extended the theory to two dimensional case for extra robustness.

The results of this paper are the bases for proposing a novel aeronautical communication system architecture for exchanging CNS (Communication, Navigation and Surveillance) related data between aircraft and air traffic management(ATM) system in general. We broaden the scope of potential domains from surveillance to CNS due to fact, that the nature of communication, navigation and surveillance in today's aviation is relatively similar –

all the system, independent from the domain, exchange coded messages between avionics and ground equipment. Although the proposed algorithm is seen to have most potential in the surveillance domain, there are clear benefits in using adaptive beamforming in other domains also. Next steps will be proposing a best suited DOA algorithm and distributed beamforming algorithm for wireless sensor networks. Proposed system will achieve higher availability and reliability with lower implementing and maintaining costs.

In this paper we assume the sensor array to be a 2D narrow band linear array. Slepian sequences have been used in both the steering and blocking branches of the algorithm. The steering and blocking branches have been directed in opposite directions.

Throughout the paper the italic, bold face lower case and bold face upper case letters will be used for scalars, column vectors and matrices respectively. The superscript T denotes transposition of a matrix, superscript H Hermitian transposition of a matrix and superscript $*$ denotes conjugate of a complex number. The symbol \odot stands for Hadamard multiplication of two matrices and $\text{vec}(\cdot)$ represents vectorization of a matrix. Column vector consistent of ones is denoted as $\mathbf{1} = [1, 1, 1, \dots, 1]^T$, \mathbf{I} denotes for identity matrix. Trace of a matrix is written as $\text{Tr}(\cdot)$.

2. SLEPIAN SEQUENCES

In the article we assume, that the wave impinging sensor array at electrical incidence angle Φ_{AZ} and Φ_{EL} is planar. Φ_{AZ} shows the azimuth, Φ_{EL} the elevation of the source. Both angles are measured with respect to the normal of the array. Sensor array is rectangular and consists $M \times N$ antenna elements. The antenna steering matrix toward incidence angle can be expressed as

$$\mathbf{A}_{m,n} = [e^{i(m-1)\Phi_{AZ}} e^{i(n-1)\Phi_{EL}}], \quad (1)$$

where $m = 1, 2, \dots, M$ and $n = 1, 2, \dots, N$.

Slepian sequences, denoted as \mathbf{B} , are window functions that for given angular region $D = [(-\varphi_{AZ}, \varphi_{AZ}), (-\varphi_{EL}, \varphi_{EL})]$ provide the maximal concentration of energy so that the spectral consecration is maximal.

$$\lambda = \frac{\iint_D \|\mathbf{1}^T [\mathbf{B} \odot \mathbf{A}(\Phi_{AZ}, \Phi_{EL})] \mathbf{1}\|^2 d\Phi_{EL} d\Phi_{AZ}}{\iint_G \|\mathbf{1}^T [\mathbf{B} \odot \mathbf{A}(\Phi_{AZ}, \Phi_{EL}), \Phi_{EL}] \mathbf{1}\|^2 d\Phi_{EL} d\Phi_{AZ}} \quad (2)$$

In the above $G = [(-\pi, \pi), (-\pi, \pi)]$

In what follows we drop explicit arguments Φ_{AZ} and Φ_{EL} , if they are not necessary to avoid confusion.

After normalising the total power in the denominator in (2) to unity, we need to maximize

$$\lambda = \iint_D \|\mathbf{1}^T [\mathbf{B} \odot \mathbf{A}] \mathbf{1}\|^2 d\Phi_{EL} d\Phi_{AZ} \quad (3)$$

It has been shown in [1] that

$$\mathbf{y}^H (\mathbf{S} \odot \mathbf{V}) \mathbf{x} = \text{Tr}[(\mathbf{y}\mathbf{1})^H \mathbf{S} (\mathbf{x}\mathbf{1}) \mathbf{V}^T] \quad (4)$$

where \mathbf{S} and \mathbf{V} are arbitrary matrices; \mathbf{x} and \mathbf{y} arbitrary column vectors with respectful lengths. Taking into account equation (4) we can write

$$\mathbf{1}^T [\mathbf{B} \odot \mathbf{A}] \mathbf{1} = \text{Tr}(\mathbf{B}\mathbf{A}^T) \quad (5)$$

It can easily be shown that trace of a matrix product can be written as follows

$$\text{Tr}(\mathbf{B}\mathbf{A}^T) = \text{Tr}(\mathbf{B}^T \mathbf{A}) = \text{vec}(\mathbf{B}^T) \text{vec}(\mathbf{A}) \quad (6)$$

We now can write (3) as follows

$$\begin{aligned} \lambda &= \iint_D \text{vec}(\mathbf{B})^T \text{vec}(\mathbf{A}) \text{vec}(\mathbf{A})^T \text{vec}(\mathbf{B}) d\Phi_{EL} d\Phi_{AZ} \\ &= \text{vec}(\mathbf{B})^T \iint_D \text{vec}(\mathbf{A}) \text{vec}(\mathbf{A})^T d\Phi_{EL} d\Phi_{AZ} \text{vec}(\mathbf{A}) \\ &= \mathbf{b}^T \mathcal{A} \mathbf{b} \end{aligned} \quad (7)$$

where $\mathcal{A} = \iint_D \text{vec}(\mathbf{A}) \text{vec}(\mathbf{A})^T d\Phi_{EL} d\Phi_{AZ}$ is a $MN \times MN$ square matrix and \mathbf{b} is a vectorized version of \mathbf{B} . From one hand, the matrix \mathcal{A} is positive definite, as has been shown in (7), on the other hand, the maximal value of (2) is 1, thus all the eigenvalues λ of \mathcal{A} lie between 0 and 1. The physical interpretation of λ is that it shows the level of energy concentration to given angular region D . As $\lambda \rightarrow 1$ shows good and $\lambda \rightarrow 0$ showing bad energy concentration.

Let's now concentrate on how one can calculate matrix \mathcal{A} . Steering matrix \mathbf{A} can be expressed as

$$\mathbf{A} = [\mathbf{a}_1, \mathbf{a}_2, \dots, \mathbf{a}_N] \quad (8)$$

where $\mathbf{a}_n = [e^{i(m-1)\Phi_{AZ}} e^{i(n-1)\Phi_{EL}}]$ is a column vector. Square of vectorized matrix \mathbf{A} can be written as

$$\text{vec}(\mathbf{A}) \text{vec}(\mathbf{A})^T = \begin{bmatrix} \mathbf{a}_1 \mathbf{a}_1^T & \mathbf{a}_1 \mathbf{a}_2^T & \dots & \mathbf{a}_1 \mathbf{a}_N^T \\ \mathbf{a}_2 \mathbf{a}_1^T & \mathbf{a}_2 \mathbf{a}_2^T & \dots & \mathbf{a}_2 \mathbf{a}_N^T \\ \vdots & \vdots & \ddots & \vdots \\ \mathbf{a}_N \mathbf{a}_1^T & \mathbf{a}_N \mathbf{a}_2^T & \dots & \mathbf{a}_N \mathbf{a}_N^T \end{bmatrix} \quad (9)$$

5 It is evident that $\text{vec}(\mathbf{A}) \text{vec}(\mathbf{A})^T$ is consistent of N^2 square matrices, each being with size $M \times M$. We first need to calculate $\iint_D (\mathbf{a}_k \mathbf{a}_l^T)_{u,v} d\Phi_{EL} d\Phi_{AZ}$, o be able to find

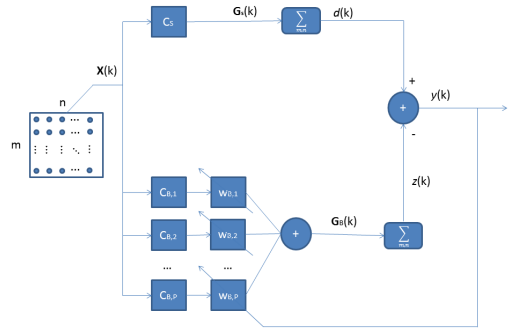


Fig. 1. Block diagram of robust generalized sidelobe canceller for 2D antenna array.

each element of \mathcal{A}

$$\begin{aligned} &\iint_D (\mathbf{a}_k \mathbf{a}_l^T)_{u,v} d\Phi_{EL} d\Phi_{AZ} \\ &= \iint_D e^{i(u+v-2)\Phi_{AZ}} e^{i(k+l-2)\Phi_{EL}} d\Phi_{EL} d\Phi_{AZ} \\ &= 4 \frac{\sin(\varphi_{AZ}(u+v-2))}{u+v-2} \frac{\sin(\varphi_{EL}(k+l-2))}{k+l-2} \end{aligned} \quad (10)$$

where $(l, k) = 1, \dots, N$ indicates a specific product of vectors in (9) and $(u, v) = 1, \dots, M$ marks each element in outcome matrix of a vector product.

3. ROBUST ADAPTIVE SIDELOBE CANCELLER WITH SLEPIAN SEQUENCES

The block diagram of a Robust Adaptive Generalized Sidelobe Canceller for two dimensional antenna array is shown in figure (1).

In an essence, the proposed beamformer is a robustified General Sidelobe Canceller and consists two branches. The upper branch forms a desired signal output $d(k)$ or in other words directs the antenna beam toward the desired source. The lower branch passes trough signals from interfering sources and blocks the signal from desired source. The output of an algorithm $y(k)$ is formed by subtracting the output of blocking branch from the output of the steering branch. **Output of the steering branch $d(k)$** is given by equation

$$d(k) = \mathbf{1}^T \mathbf{G}_s(k) \mathbf{1}, \quad (11)$$

where matrix \mathbf{G}_s is expressed as

$$\mathbf{G}_s(k) = \mathbf{C}_s \odot \mathbf{X}(k), \quad (12)$$

where \mathbf{C}_s represents the window steering matrix and $\mathbf{X}(k)$ represents the signal impinging antenna array at time instance k .

Window steering matrix \mathbf{C}_s is calculated by performing an element-wise multiplication of the steering matrix toward desired source $\mathbf{A}_s^{(0)}(\varphi_{0,AZ}, \varphi_{0,EL})$ and the Slepian

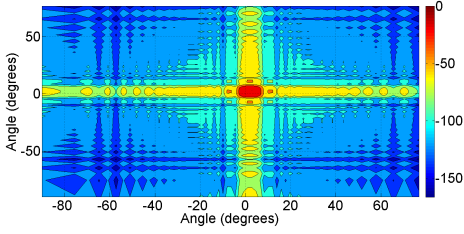


Fig. 2. Response of steering branch \mathbf{G}_s . (The values shown are in decibels).

sequence \mathbf{B}_s

$$\mathbf{C}_s = \mathbf{A}_s^{(0)} \odot \mathbf{B}_s. \quad (13)$$

It must be bared in mind that narrow Slepian gives good noise suppression whereas wide Slepian improves the robustness against imperfect knowledge of the source, so a compromise has to be made when choosing the Slepian window function for the algorithm.

Signal matrix $\mathbf{X}(k)$ in equation (12) is given by

$$\mathbf{X}(k) = \sum_{d=1}^D \mathbf{A}^{(d)} s_d(k) + \mathbf{V}(k), \quad (14)$$

where $\mathbf{A}^{(d)}$ is a steering matrix toward d -th source, $d = 1, 2, \dots, D$, with D representing the total number of sources present, $s_d(k)$ is signal at time instance k emitted by the d -th source and $\mathbf{V}(k)$ is an additive zero mean Gaussian noise matrix.

Response of steering branch, \mathbf{G}_s , toward angle $(2^\circ, 2^\circ)$ with one Slepian window is shown on figure (2)

Output of the blocking branch $z(k)$ is given by equation

$$z(k) = \mathbf{1}^T \mathbf{G}_B(k) \mathbf{1}, \quad (15)$$

where response matrix of a blocking branch $\mathbf{G}_B(k)$ is given by equation

$$\mathbf{G}_B(k) = \sum_{p=1}^P w_{B,p} \mathbf{C}_{B,p} \odot \mathbf{X}(k). \quad (16)$$

In the above, $w_{B,p}$ is a p -th filter coefficient, $p = 1, 2, \dots, P$, with P showing the length of the filter. In the paper in hand the filter coefficients are updated according Normalized Least Mean Square rule but it must be stated that any other adaptive scheme can be used instead. As one can see from the figure (1), the length of the filter is set by the number of window blocking matrices $\mathbf{C}_{B,p}$ defined in the blocking branch. The latter is tied with the number of Slepian sequences used in the blocking branch. The window blocking matrix $\mathbf{C}_{B,p}$ is given by the equation

$$\mathbf{C}_{B,p} = \mathbf{A}_b^{(0)} \odot \mathbf{B}_{b,p} \quad (17)$$

where $\mathbf{B}_{b,p}$ is p -th slepian sequence used in the algorithm. Matrix $\mathbf{A}_b^{(0)}(\varphi_{0,AZ}, \varphi_{0,EL})$ is constructed so that the low gain is formed in the direction of the desired source and high gain is formed in all other direction. It means that in

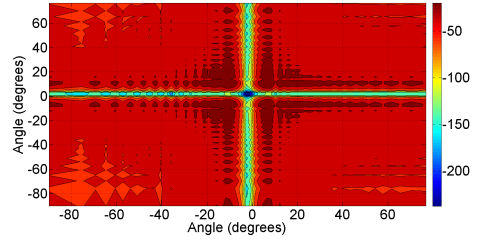


Fig. 3. Response of blocking branch \mathbf{G}_b . (The values shown are in decibels).

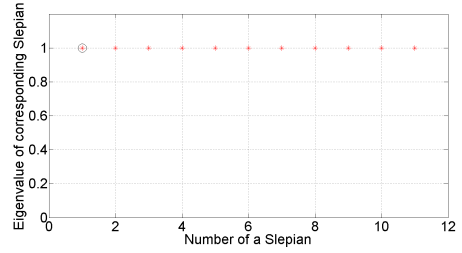


Fig. 4. Eigenvalues of used Slepian window functions. (Eigenvalue of a steering Slepian is shown with \circ and eigenvalues used in blocking branch with $*$)

a sense the $\mathbf{A}_b^{(0)}$ contrary to steering matrix toward desired source $\mathbf{A}_s^{(0)}$ and can be expressed as follows

$$\mathbf{A}_b^{(0)} = [e^{i(m-1)(\varphi_{0,AZ}+\pi)} e^{i(n-1)(\varphi_{0,EL}+\pi)}]. \quad (18)$$

The output signal $y(k)$ of whole algorithm is given by

$$y(k) = d(k) - z(k). \quad (19)$$

The eigenvalues of Slepian window functions used in the example in this section are shown in figure (4). It is evident that window functions used are good in concentrating energy into the specified angular region.

4. ADAPTIVE GENERAL SIDELobe CANCELLER

We have chosen non-robust Adaptive General Sidelobe Canceller (AGCS) as a reference to the proposed beamformer. AGCS has been implemented as shown on figure (5) and a brief description of the algorithm has been given in this section.

Like any other General Sidelobe Canceller, the one described here comprise two branches: upper branch (the steering branch) filters out signals emitted by unwanted sources and the lower branch (blocking branch) filters out signal emitted by the desired source. The output of an algorithm is calculated by subtracting the output of the blocking branch from the output of the steering branch. Latter can be expressed with the following expression

$$y(k) = d(k) - z(k), \quad (20)$$

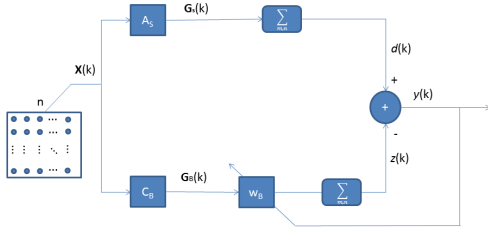


Fig. 5. Block diagram of two dimensional Adaptive General Sidelobe Canceller.

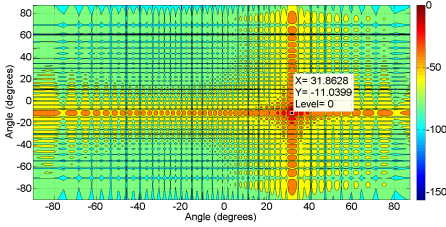


Fig. 6. An example of the response of a steering branch. (The values shown are in decibels).

where $d(k)$ and $z(k)$ are the outputs of steering and blocking branch at the k -th time instance respectively.

Output of the steering branch $d(k)$ is expressed as

$$d(k) = \mathbf{1}(\mathbf{A}_s \odot \mathbf{X}(k))\mathbf{1} \quad (21)$$

where \mathbf{A}_s in equation is a steering matrix toward desired source given in equation (1) and $\mathbf{X}(k)$ is a signal impinging antenna array at time instance k and is given with equation (14).

An example of the response of a steering branch $\mathbf{G}_S = \mathbf{A}_s \odot \mathbf{X}(k)$ is shown on figure (6).

The output of blocking branch $z(k)$ is given by

$$z(k) = \mathbf{w}_b \mathbf{G}_B \mathbf{1} \quad (22)$$

where \mathbf{w}_b is a weight vector updated by Normalized Least Mean Square rule. But as stated in the Section 3. other adaptive algorithms may be used instead. \mathbf{G}_B can be expressed as follows

$$\mathbf{G}_B = \mathbf{C}_U \mathbf{X}(k) \mathbf{C}_V \quad (23)$$

The matrices \mathbf{C}_U and \mathbf{C}_V are extracted from the steering matrix toward desired source \mathbf{A}_s as follows.

As proposed in [5] we are using singular value decomposition of a \mathbf{A}_s so that

$$\mathbf{A}_s = \mathbf{U} \mathbf{S} \mathbf{V}^H \quad (24)$$

where \mathbf{U} is a $M \times M$ matrix containing orthonormal eigenvectors of $\mathbf{A}_s \mathbf{A}_s^H$, \mathbf{V} is a $N \times N$ matrix consistent of orthonormal eigenvectors of $\mathbf{A}_s^H \mathbf{A}_s$. \mathbf{S} , with size $M \times N$, contains the singular values of \mathbf{A}_s in its diagonal in descending order. Singular values of a matrix essentially

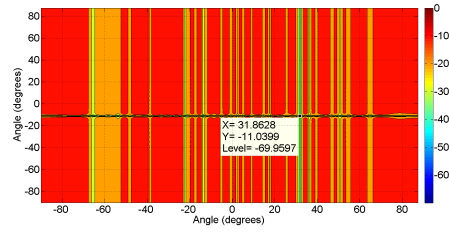


Fig. 7. An example of the response of a blocking branch. (The values shown are in decibels).

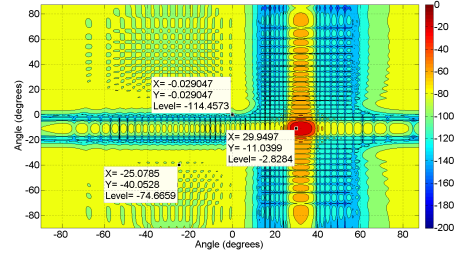


Fig. 8. Antenna pattern of the proposed sidelobe canceller (direction of the desired source $(30^\circ, -11^\circ)$). (The values shown are in decibels).

are the square roots of the eigenvalues of both $\mathbf{A}_s \mathbf{A}_s^H$ and $\mathbf{A}_s^H \mathbf{A}_s$

We can express \mathbf{U} and \mathbf{V} as a set of vectors

$$\begin{aligned} \mathbf{U} &= [\mathbf{u}_1, \mathbf{u}_2, \dots, \mathbf{u}_M] \\ \mathbf{V} &= [\mathbf{v}_1, \mathbf{v}_2, \dots, \mathbf{v}_N] \end{aligned} \quad (25)$$

where \mathbf{u}_n and \mathbf{v}_m are column vectors with lengths M and N respectively.

The matrices \mathbf{C}_U and \mathbf{C}_V in equation (23) are formed by discarding a first column or in other words the first vector from the \mathbf{U} and \mathbf{V} . By doing so the matrices \mathbf{C}_U and \mathbf{C}_V will take the following forms

$$\begin{aligned} \mathbf{C}_U &= [\mathbf{u}_2, \mathbf{u}_3, \dots, \mathbf{u}_M] \\ \mathbf{C}_V &= [\mathbf{v}_2, \mathbf{v}_3, \dots, \mathbf{v}_N] \end{aligned} \quad (26)$$

Using matrices \mathbf{C}_U and \mathbf{C}_V as given by equation (26) in the equation (23) blocks the signal from the desired source from passing through the blocking branch. An example of the response of a blocking branch is shown on figure (7).

5. SIMULATION RESULTS

In the first example the antenna consists 32×32 elements. The elements are directed toward array broadside and are uniformly spaced with half wave length space between each antenna element.

The source in interest is supposed to be at $(-23^\circ, -51^\circ)$ but actually is located at $(-25^\circ, -49^\circ)$. Signal power emitted by the source in interest is $P_{d,1} = 1$.

Interfering sources are located at $(60^\circ, 40^\circ)$ and $(-60^\circ, -10^\circ)$ with emitted signal powers $P_{i,1} = 100$ and

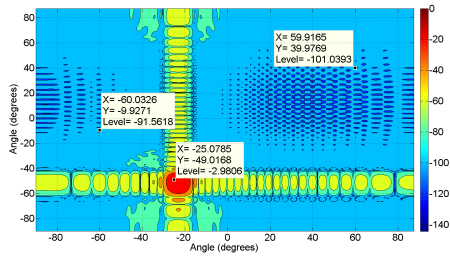


Fig. 9. Antenna pattern of the proposed sidelobe canceller (direction of the desired source $(-25^\circ, -49^\circ)$). (The values shown are in decibels).

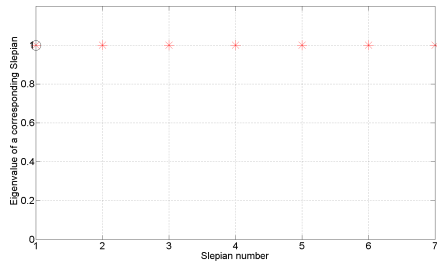


Fig. 10. Eigenvalues of Slepian window functions (direction of the desired source $(-25^\circ, -49^\circ)$; eigenvalue of a steering Slepian is shown with \circ and eigenvalues used in blocking branch with $*$).

$P_{I,2} = 400$ respectively. Additive noise at all the antenna elements are assumed to be zero mean Gaussian noise with variance $\sigma_v^2 = 1$.

One Slepian window function is used in the steering branch and seven in the blocking branch. All Slepian used in the exercise have the eigenvalue equal to 1 (figure (10)).

The steady state antenna pattern is shown on figure (9). At angles $(-25^\circ, -49^\circ)$ the gain is about 3 dB smaller than the maximum gain which is located at $(-23^\circ, -51^\circ)$. In the directions of the interferes the gain of a antenna is smaller than -101 dB and -91 dB indicating good sidelobe cancellation capability.

gradual development of the magnitudes of NLMS filter coefficients, used in the blocking branch, are shown on figure (11). It can be seen from the figure that the system achieves its steady state after 5000 iterations.

In the second example source in interest is expected to be at $(33^\circ, -9^\circ)$ but actually is located at $(30^\circ, -11^\circ)$. Power of the desired signal is set to unity.

There are two interferes at $(-25^\circ, -40^\circ)$ and $(0^\circ, 0^\circ)$ with emitted signal powers $P_{I,1} = 1400$ and $P_{I,2} = 1100$ respectively. Like in the first example Gaussian noise, independent from at all antenna elements, with variance $\sigma_v^2 = 1$ has been added to the signal impinging antenna array.

The antenna has 48×32 elements and is assumed to be planar antenna array. Antenna elements are evenly spaced

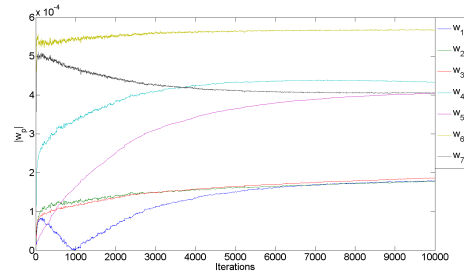


Fig. 11. Evolution of NLMS filter coefficients magnitudes (direction of the desired source $(-25^\circ, -49^\circ)$).

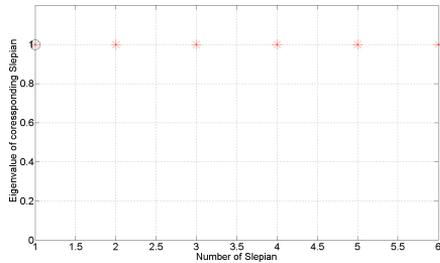


Fig. 12. Eigenvalues of Slepian window functions (direction of the desired source $(30^\circ, -11^\circ)$; eigenvalue of a steering Slepian is shown with \circ and eigenvalues used in blocking branch with $*$).

with half wave length distance between them. A different set of Slepian have been chosen for this example but the eigenvalues of all the window functions are again one as shown on figure (12).

The steady state antenna pattern can be seen in (8). Gain in the actual direction of source in interest is about -3 dB compared with 0 dB at $(30^\circ, -11^\circ)$ where the desired source was expected to be. The antenna gains in the directions of the interfering sources are -75 dB and -114 dB below maximum. Due to the fact that we have used more antenna elements in horizontal plane than in vertical, one can notice slightly lower sidelobes in horizontal plane.

The progression of the NLMS filter coefficients is shown on figure (13) where it can be seen that the steady state is achieved after 500 iterations. Higher variations of the coefficients can be explained with stronger interfering signals.

In the third example, the antenna and signal parameters are set exactly the same as in the second example.

The progression of the first six filter coefficients, used in the AGSC, are shown on the figure (15). One can see that the steady state antenna pattern is achieved approximately after 500 filter iterations.

The steady state antenna pattern of AGSCanceller is given on figure (14). As expected, the antenna gain is relatively low in the direction of the interferes (-54 dB and -62 dB), as well as in the actual direction of desired source (-24 dB). It is evident that erroneous estimate of directions

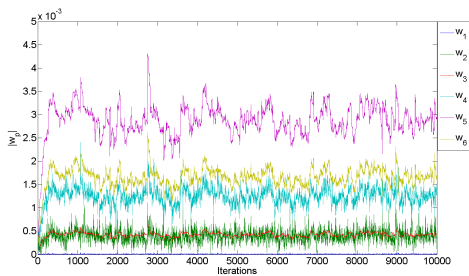


Fig. 13. Evolution of NLMS filter coefficients magnitudes (direction of the desired source ($30^\circ, -11^\circ$)).

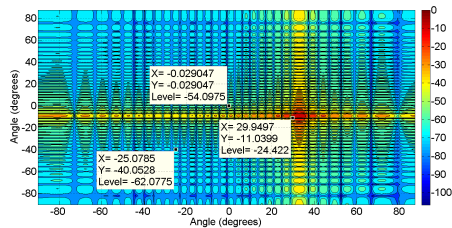


Fig. 14. Antenna pattern of the Adaptive Sidelobe Canceller (direction of the desired source ($30^\circ, -11^\circ$)). (The values shown are in decibels).

of arrival has a significant impact on the performance of the Generalized Sidelobe Canceller.

6. CONCLUSIONS

In this paper we propose a Robust Generalized Sidelobe Canceller using Slepian window functions that can be used in airport ground surveillance system. We have extended the theory to two dimensions so that 2D antenna arrays may be used for gaining extra robustness. Simulations clearly show that the robustified GSC using Slepian window functions outperforms the non-robust GSC, proving that the theoretical results are correct. The proposed algorithm is a bases for proposing a novel communication system using distributed beamforming algorithm.

7. REFERENCES

- [1] R. A. Horn and C. R. Johnson, *Topics in Matrix Analysis*. Cambridge University Press, 1991.
- [2] N. Petrochilos, G. Galati, and E. Piracci, "Separation of ssr signals by array processing in multilateration systems," in *IEEE Transactions on Aerospace and Electronic Systems*, vol. VOL. 45, no. NO. 3, July 2009, pp. 965–982.
- [3] C. Reck, M. S. Reuther, U. Berold, and L. Schmidt, "Spatial filtering and equalization for ssr signal detection in a multipath environment," in *Microwave Conference (GeMIC)*, 2011, pp. 1–4.

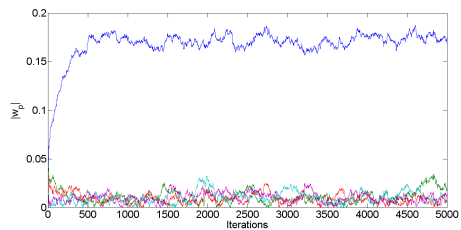


Fig. 15. Evolution of first six coefficients magnitudes of the NLMS filter used in the AGSC (direction of the desired source ($30^\circ, -11^\circ$)).

- [4] T. Trump, "A robust adaptive sensor array with slepian sequences," in *Sensor Array and Multichannel Signal Processing Workshop (SAM), 2012 IEEE 7th*, 2012.
- [5] B. D. Van Veen and K. M. Buckley, "Beamforming: A versatile approach to spatial filtering," *IEEE ASSP Magazine*, pp. 4–24, April 1988.

APPENDIX E

OpenSky Report 2020: Analysing In-Flight Emergencies Using Big Data

X. Olive et al., 2020 AIAA/IEEE 39th Digital Avionics Systems Conference (DASC), San Antonio, TX, USA, 2020, pp. 1-10, doi: 10.1109/DASC50938.2020.9256787.

OpenSky Report 2020: Analysing in-flight emergencies using big data

Xavier Olive^{¶||}, Axel Tanner^{**}, Martin Strohmeier^{¶†§}, Matthias Schäfer^{¶‡*}, Metin Feridun[§],
Allan Tart[¶], Ivan Martinovic^{¶†}, Vincent Lenders^{¶§}

[¶]OpenSky Network, Switzerland
lastname@opensky-network.org

^{||}ONERA, Université de Toulouse, France
xavier.olive@onera.fr

^{**}IBM Research, Switzerland
axs@zurich.ibm.com

^{*}TU Kaiserslautern, Germany
schaefer@cs.uni-kl.de

[†]University of Oxford, UK
firstname.lastname@cs.ox.ac.uk

[‡]SeRo Systems, Germany
schaefer@sero-systems.de

[§]armasuisse, Switzerland
firstname.lastname@armasuisse.ch

Abstract—Transponder codes are four octal digit numbers transmitted by an aircraft transponder in response to a secondary surveillance radar interrogation. These discrete transponder codes (also known as squawk codes) help with the clear labelling of an affected aircraft on radar screens. Three particular squawk codes are associated with specific situations: 7500 for hijacking, 7600 for radio failure and 7700 for general emergencies, often related to medical or technical issues.

In this paper, we analyse more than 800 trajectories received by the OpenSky Network over a two-year period as they were broadcasting the 7700 emergency code. Background information about the reason of these emergencies is taken from social networks and other crowdsourced information sources on the Internet. We provide an overview of various reasons for in-flight emergencies, typical trajectory patterns and communication strategies by airlines. Based on our semi-labelled dataset of trajectories, we also train models able to suggest possible explanations for trajectories when no information is available.

I. INTRODUCTION

A transponder is a key electronic on-board device which helps identifying aircraft on air traffic control (ATC) radars. Traditionally, transponders produce a response on the 1090 MHz frequency after receiving a radio-frequency interrogation on 1030 MHz from Secondary Surveillance Radar (SSR) systems (both from the ground and other aircraft). In particular, they support the transponder Modes A, C and S, traffic alert and collision avoidance systems (TCAS) [1], and the novel Automatic Dependent Surveillance – Broadcast (ADS-B), which does not require interrogations.

Air traffic controllers use the term *squawk* to assign aircraft a transponder code which is used to identify an aircraft uniquely in a distinct flight information region (FIR). The most elementary information transmitted by transponders (Mode A/C) include information about pressure altitude (Downlink Format 4) and identification (or squawk code, Downlink Format 5).

Squawk codes are made of four octal digits; the traditional dials on a transponder read from zero to seven. In normal use, squawk codes are assigned to an aircraft by ATC and subsequently applied by the pilot. Beyond this procedure, there are conventions for squawk codes, which can be selected by aircraft if and when the situation requires or allows it,

without permission from ATC. Three such emergency codes are applicable worldwide: 7500 is reserved for hijacking situations and may not be used during training as it triggers a very strict security protocol; 7600 reports a radio failure to the ATC, and 7700 is reserved for general emergencies.

Usually, emergencies are first reported to the ATC over the radio while the crew is assessing the situation or running through checklists (after following the old adage, “aviate, navigate, communicate”). Depending on the nature of the issue, on its gravity and on provided facilities for the airline in different airfields, pilots may choose to divert the aircraft or to continue to their final destination. When diverting, aircraft type and airline procedures may require specific manoeuvres and dumping fuel before landing. Squawking 7700 helps ATC taking the emergency into account in terms of separation, priority and logistics: they may have to get Aircraft Rescue and Fire Fighting (ARFF) ready on the runway if necessary. Finally, there are regular occurrences where transponder squawk codes have been set mistakenly and/or only for a short time. It is important to detect and filter such occurrences.

The wide variety of aircraft emergency situations include technical issues, e.g. landing gear failing to retract, pressurisation issues, cracked windshield; fuel issues, e.g. after holding or several failed attempts to land; and passenger issues, e.g. serious medical trouble or unruly passengers. Collecting and analysing such situations on a larger scale can provide two benefits: First, the insights from the use of transponder codes in real emergencies may assist in future safety analyses of emergency situations. Second, comparative knowledge about the differences between airspace in their handling of 7700 codes could provide incentives to refine such procedures.

In this paper, we present the first large-scale study about emergency squawks, their causes and consequences. In order to present a comprehensive view, we collect open-source information about worldwide emergency situations over two years (2018 and 2019). Trajectory and squawk information are extracted from the OpenSky Network [2] database and background information related to the situations is found on external sources, including social networks such as Twitter and crowdsourced information related to incidents and accidents (such as The Aviation Herald [3]).

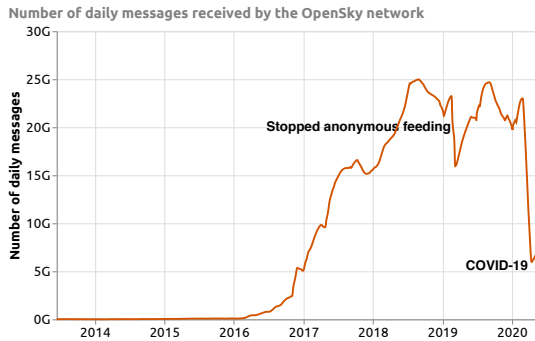


Fig. 1. The growth of OpenSky’s dataset over time from 2013 to May 2020

The remainder of this work is organised as follows: Section II describes the overall data collection and preprocessing from various sources of information. Section III provides statistics and observations in the data. Section IV describes common trajectory patterns with real-world emergency situations. This is followed by Section V that with a short overview of findings of the other general emergency transponder codes in the data. Section VI discusses our results and some general points on emergency squawks while Section VII concludes this work.

II. DATA COLLECTION AND PROCESSING

A. The OpenSky Network

The OpenSky Network is a crowdsourced sensor network collecting air traffic control (ATC) data. Its objective is to make real-world ATC data accessible to the public and to support the development and improvement of ATC technologies and processes. Since 2013, it has continuously been collecting air traffic surveillance data. Unlike commercial flight tracking networks (e.g., Flightradar24 or FlightAware), the OpenSky Network keeps the raw Mode S replies as they are received by the sensors in a large historical database, which can be accessed by researchers and analysts from different areas.

The network started with eight sensors in Switzerland and Germany and has grown to more than 3000 registered receivers at locations all around the world. As of this writing, OpenSky’s dataset contains seven years of ATC communication data. While the network initially focused on ADS-B only, it extended its data range to the full Mode S downlink channel in March 2017, which is also the base for this present work. The dataset currently contains more than 22 trillion Mode S replies and, before COVID 19, received more than 20 billion messages per day. Fig. 1 shows the growth and development over the past several years which saw the inclusion of the dump1090 and Radarcape feeding solutions and the integration of non-registered, anonymous receivers, which has been discontinued early 2019 to further ensure the quality of the feeder data. In March 2020, the number of daily messages dropped to about 30% of the previous level, reflecting the curtailment of

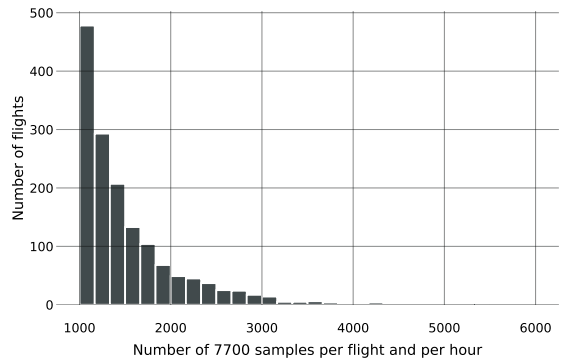


Fig. 2. Distribution of number of 7700 samples per flight per hour

air travel around the world due to the COVID 19 pandemic. Recovery has been slow so far and it may take years to return to the previous numbers. Besides the payload of each Mode S downlink transmission, OpenSky stores additional metadata. Depending on the receiver hardware, this metadata includes precise timestamps (suitable for multilateration), receiver location, and signal strength. For more information on OpenSky’s history, architecture and use cases refer to [4], [5] or visit <https://opensky-network.org>.

B. Data collection

The OpenSky Network provides a SQL-like Impala-based API to the whole database of collected and decoded trajectory information. As 7700 emergency codes remain exceptional events, we first identified emergency trajectories based on the number of samples in a given flight that contained 7700 squawk codes. A first request to the database collected *icao24* addresses (a 6-character hexadecimal number, 24 bits, named after the International Civil Aviation Organization and uniquely associated to a transponder), *callsigns* (a 8 character alphanumeric identifier associated to a mission or a commercial route), *first* and *last* timestamps, a maximum value of altitude and a number of 7700 messages per hour.

The result of this request shows an exponential distribution (see Figure 2) of the number of 7700 squawk samples per flight. We find that there are many unreliable short alerts; either aircraft sending 7700 for only few seconds or a ground receiver wrongly decoding 7700 for an aircraft. One of the challenges of a large-scale distributed network of ADS-B receivers is to manage to collect enough data around the world: this is difficult to achieve without accepting data of a poorer quality. Before 2019 (see Figure 1), anonymous feeding of preprocessed data included false 7700 alerts from some receivers that we had to later manually remove from our dataset. For a longer discussion of data integrity issues in crowdsourced ADS-B networks, see our OpenSky Report 2018 [6].

Another main reason for false alarms in the data comes from transitions in squawk codes. While pilots are taught not

to manually accidentally roll over the emergency codes, some transponder models seem to transition from a squawk code to the next one by not changing digits all at the same time. This also happens when aircraft transition from a squawk code to an emergency 7700 squawk code. For instance, in the dataset associated to this contribution, aircraft 3c9432 (D-BEAR) with callsign AXG1801 started squawking 7700 on Sep. 17, 2019. After squawking 6603, the aircraft very shortly emitted 7703 before switching to 7700:

icao24	timestamp	squawk code
3c9432	2019-09-17 06:25:00Z	6203
3c9432	2019-09-17 06:41:11Z	7703
3c9432	2019-09-17 06:41:14Z	7700

TABLE I
TRANSITION FROM 6203 TO 7700 SQUAWK CODES

After analysing the non-processed flight data, we decided to limit our selection of trajectories to aircraft respecting the following constraints:

- 1) more than 1000 samples with a 7700 squawk code;
- 2) a valid icao24 value (i.e., we remove 000000, 000001 and other anomalous or wrongly decoded identifiers);
- 3) a callsign starting with three letters and one number (to remove most non-commercial flights);
- 4) a valid value of maximum altitude: most messages emitted from the ground do not send any altitude value and we focus here on flown trajectories.

After obtaining this preprocessed dataset of relevant emergency codes, we matched each selected icao24, start and end timestamps with samples the `flights_data4` table in the database, which contains one line of information per trajectory, including first and last recorded timestamps for each trajectories. Appropriate requests were written to efficiently download corresponding trajectories between January 1st 2018 and January 31th 2020.

C. Trajectory processing

All trajectories have been requested and preprocessed with the help of the `traffic` Python [7] library, which downloads OpenSky data, converts the data to structures wrapping pandas data frames and provides specialised semantics for aircraft trajectories (e.g., intersection, resampling or filtering). In particular, it iterates over trajectories based on contiguous timestamps of data reports from a given icao24 identifier.

Data selected from the OpenSky database for our emergency dataset yielded 1506 trajectories. In spite of the efforts described in previous section, many trajectories in this first version of the dataset remained irrelevant:

- 1) no positional (latitude/longitude) information was included for a trajectory due to a lack of ADS-B capable transponder;
- 2) ground vehicles at airports were associated to a 7700 squawk code (Figure 3);
- 3) irrelevant legs from the same flight: when an aircraft is associated to a (mostly medical) 7700 emergency, diverts

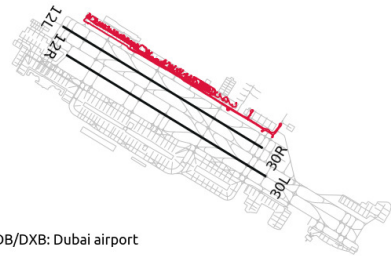


Fig. 3. Ground vehicle (identifier 896ed4) continuously squawking 7700 on October 12th, 2019 at Dubai airport

to the closest airport and takes off again after things have been cleared, we need to trim the trajectory down to the leg ending at the diversion airport.

Trajectories have been selected, filtered with the help of the traffic library grammar and enriched with information from OpenSky aircraft database, including aircraft registration and typecodes, as well as commercial International Air Transport Association (IATA) numbers and a planned route associated to a callsign. Ground vehicles were thereby filtered out with information from the aircraft database.

Then, a set of traffic methods has been chained to:

- remove non-positional samples;
- filter out invalid values of altitude;
- filter out invalid positions based on recomputed invalid ground speeds values (too fast often means invalid lat/lon position, too slow could mean that the transponder is still on after the aircraft reached its parking position);
- trigger a new iteration on all trajectories;
- remove flights with no 7700 samples;
- remove flights sending 7700 only in areas covered by a suspicious set of anonymous receivers;
- resample trajectories with one sample per second.

The resulting dataset contains 832 trajectories fully labelled with aircraft information (icao24 identifier, registration number, typecode), flight information when available (flight commercial IATA number, planned origin and destination airports, detected take-off and landing airports and when applicable diversion airports)

The data presented in this paper is now provided as a generic import in the `traffic` library as `squawk7700`, triggering a download from a corresponding Zenodo repository [8] if the data is not in the cache directory of the user. ADS-B trajectory information are available in a first tabular file, a second one contains metadata information associated to each trajectory.

D. Additional data sources

For further enrichment and a complementary perspective on the cases identified in the OpenSky data, we looked at two publicly available data sources on the web.

- **Twitter:** We conducted searches through the Twitter web page, using callsign, registration, flight number as

	Africa	America	Asia	Europe	Mid. East	Russia
Africa				15		
America		361	6	44	3	1
Asia		1	11		3	
Europe	25	59	2	213	2	5
Mid. East	1	1	3	5	6	
Russia				4		12

TABLE II
NUMBER OF EMERGENCY FLIGHTS PER ORIGIN (LINE) AND DESTINATION (COLUMN) CONTINENT.

identifiers together with the since and until keywords as defined in its advanced search capabilities, in order to restrict the date ranges of the search, starting with the day of the first emergency squawk to 4 days later: this allows emerging explanations or details to be found.

- **The Aviation Herald:** Relevant articles were identified using date, flight numbers and registration. Data has been manually classified to evaluate the reasons of the emergency, the resulting action (divert, return, continue) and whether fuel was dumped or flights put on hold to burn fuel where possible from the sources.

Whereas Twitter provides fast, often unsourced, information within short text messages provided by a mix of users, The Aviation Herald focuses on safety-relevant technical issues through detailed and thoroughly sourced reporting. Information provided by Twitter users can comprise first-hand accounts by companies, passengers or crew, but also bots and non-involved enthusiasts speculating wildly with unsubstantiated guesses.

III. STATISTICS

a) *Global coverage:* Data collected for this analysis heavily depend on the global coverage of the OpenSky Network of ADS-B receivers. Anonymous feeding has been discontinued in early 2019 in order to improve data quality: this had few impact on the dataset we constituted since anonymous feeders were a serious source of false positive.

Figure 4 compares the OpenSky Network global coverage (above) at the time of submission with the density of emergency trajectories (below). The distribution is consistent with the global coverage, although Northern France and the UK (zoomed in upon in Figure 5) seem to yield a rather high distribution of emergency squawks in the vicinity of Paris airports and along the path to transatlantic routes. This reveals different practices in dealing with emergencies according to countries.

Tables II and III list the most common airlines and aircraft types with a number of emergency situations to be compared with a reference number of flights in one month (January 2019) Bigger absolute values come from the bigger airlines and most short-haul aircraft: European airlines seem to yield a higher ratio, consistent with the higher distribution of 7700 situations in Europe (Figure 5), whereas the ratio for aircraft type seems more constant.

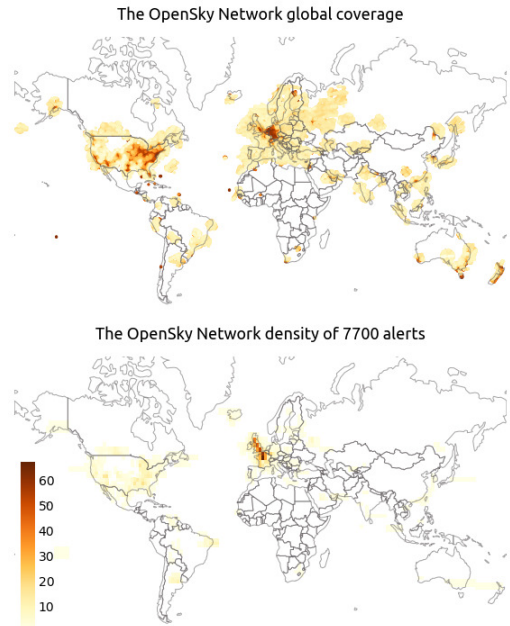


Fig. 4. Global coverage of the OpenSky Network (above) and density of 7700 alerts (below); the scale below refers to a number of unique aircraft. Note that this illustration is dependent on the density of OpenSky's coverage and air traffic in general.

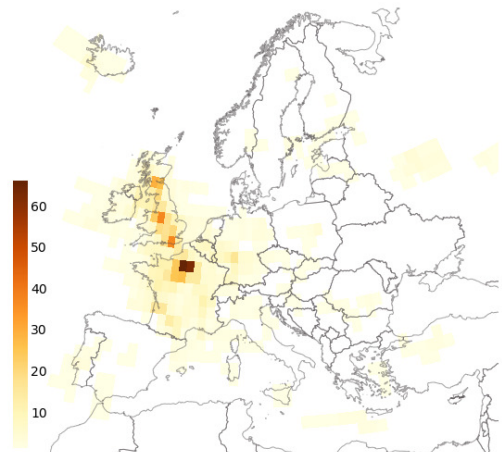


Fig. 5. Density of 7700 alerts in Europe. The clearly identifiable hotspots in the UK and around the Paris airspace are likely indicative of different approaches to handling emergency squawk procedures.

airline	7700	Jan 19	typecode	7700	Jan 19
AAL	47	72490	B738	122	173267
UAL	45	41965	A320	120	151494
EZY	40	577	A319	53	50296
DAL	38	53451	A321	42	59433
AFR	33	5118	B763	36	20156
SWA	30	63015	B737	35	51149
BAW	27	15213	B752	27	17372
RYR	19	1909	B739	27	30765
RPA	16	13585	E75L	27	33098
FDX	16	14535	B772	22	14460

TABLE III
TOP 10 BY AIRLINE AND AIRCRAFT TYPE

b) *Causes of emergency*: As specified above, additional data sources were used to evaluate known causes for an emergency, namely Twitter and reports from The Aviation Herald. In our methodology, we build and expand on earlier work in this area of data fusion [9].

In our results, we can broadly differentiate *technical*, *environmental* and *medical* causes. Table IV summarises the findings from these two sources including some subcategories in case a more detailed description was found. The subcategories are not always clear or unique, so should be considered with care.

We found *Twitter* messages for 419 cases and reports in *The Aviation Herald* for 90 cases of the total number of 832 cases identified in the OpenSky data.

Interesting to note is the high number of cases leaving traces in *Twitter* messages (419 out of 832 cases), which is, of course, to some extent, explained by some automated bots like the *Twitter* user @OpenSkyAlerts itself. That we do not find *Twitter* messages from these bots for *all* cases seems to be a limitation imposed by our way of accessing *Twitter* messages through their search mechanism. On the other hand, many other accounts add manually information related to emergency situations (for a more detailed discussion see Section III-0d).

The focus of *The Aviation Herald* is explicitly on safety-related issues, therefore in general medical emergencies are not covered. The two corresponding reports are indeed cases of medical problems of crew members and therefore included in its coverage.

c) *Measures taken after emergency*: Apart from extreme events (e.g. broken windshield, bird strike) requiring immediate action, when an incident occurs, pilots or crew first take time to assess the situation in the cockpit (technical issue) or in the cabin (smoke, passengers with an unruly behaviour or seeking immediate medical attention). Pilots may engage in holding patterns to run through checklists. The 7700 code is set upon requests from ATC, which reveals different practices according to countries. Subsequently, pilots coordinate with ATC and take a decision: follow their route or divert.

We detected 295 diverted flights in the dataset, 111 of them returned to their airport of origin. The choice of the airport of diversion usually depends on the nature of the emergency: when aircraft can divert to major hubs for the airline, it is easier to accommodate passengers on new flights,

Category	Detailed Cause	Twitter	The Aviation Herald
Technical	Unspecified technical	34	-
	Engine	18	19
	Fire/Smoke/Smell	17	16
	Cabin Pressure	12	19
	Hydraulics	5	5
	Cracked window	5	3
	Landing gear	5	2
	Fuel related	4	6
	Instrumentation	-	3
	Flaps	-	1
	Heating	-	1
	Tires	1	1
	Hot air leak	1	1
	Maintenance	-	1
	Brakes	-	1
	Miscellaneous	-	6
Slats	-	1	
Door	1	-	
Subtotal		103	86
Medical		72	2
External	Bird strike	4	1
	Weather related	3	1
	Bomb threat	2	-
	Operational issue	1	-
Unknown		234	-
Total		419	90

TABLE IV
MOST COMMON CAUSES FOR EMERGENCY AS OBSERVED IN TWITTER DATA AND THE AVIATION HERALD

LFPG	Paris CDG	France	27
EGLL	London Heathrow	United Kingdom	12
LFPO	Paris Orly	France	10
EGPF	Glasgow	United Kingdom	10
LFBD	Bordeaux	France	9
EGPH	Edinburgh	United Kingdom	7
EDDF	Frankfurt	Germany	7
EIDW	Dublin	Ireland	7
LFLL	Lyon	France	6
EGKK	London Gatwick	United Kingdom	5
LFML	Marseille	France	5
LFRS	Nantes	France	5
EGCC	Manchester	United Kingdom	5
KPHL	Philadelphia	United States	4

TABLE V
MOST COMMON 7700 DIVERSION AIRPORTS.

and to work through shift limits for the crew. In case of medical emergencies, aircraft usually resume their route after the passenger and their family have been disembarked and taken care of. When the aircraft is diverted to an inconvenient location, the airline may need to send a replacement aircraft with crew to the airport of diversion.

Table V plots the most common diversion airports in the data set. Most airports in the dataset are French or British airports: the first American airport is in 14th position in the list. This can be partly explained by different 7700 practices according to the countries.

d) *Twitter analysis*: For a large part of the emergency cases (419 out of 832) we find related messages in *Twitter*. Comparing OpenSky data and *Twitter* messages, we evaluate

the delay between first observed 7700 code and the first related Twitter message for each case. For each account we therefore can generate a distribution of delays across the different cases mentioned by that account. Figure 6 highlights Twitter accounts that have sent messages related to at least 14 cases in our observations. Each account is placed according to the median of the distribution of the delays (x-axis) and the number of our observed cases, for which we see messages by that account (y-axis). The spread of the delays is further indicated by the horizontal error bar spreading from first to third quartile of the distribution. Major language for each account is indicated by a colour.

Overall the largest coverage of our observed emergency cases is by the @OpenSkyAlerts account, not very surprising as the observed emergency cases have been derived from the OpenSky data itself used for this analysis and this account is a bot maintained by the OpenSky Network. The delay is very consistently close to 5 minutes, as the Twitter bot is using this as the delay to avoid sending spurious alert messages. Looking at the respective messages by an account, we can clearly see a bot-like behaviour with a fixed message structure for some accounts (like @OpenSkyAlerts, @SquawkAlert). These have also nearly exactly one message per case, though the relative timing might vary. Other accounts, like @planefinder, @FlightIntl, @airlivenet, also have a bot-like behaviour looking at their messages, but provide in addition to the initial message also updates where additional information (place of diversion, reason for the emergency) is broadcast.

But there also seem to be many individuals interested in aviation (respectively aviation emergencies) that have a high coverage of cases with very short delay times and a high number of informative update messages, most specifically the account @NikPhillips666.

Nearly all accounts shown here sent messages covering cases through well above one year of our two-year observation period, most of the frequent messengers cover the full observation period, showing a consistent long-term interest of the users in the topic.

Still, although social media in many cases can provide quick and accurate additional information, it is still severely limited as the data is very noisy and the role of the messenger and therefore the reliability of the message is often unclear (e.g., an airline community manager for an airline, a direct observer sitting in the aircraft or an outsider stating a guess for the reason of the emergency).

IV. ANALYSIS OF COMMON EMERGENCY PATTERNS

a) *Medical issues:* When a passenger or a crew member is unwell and their medical situation is life-threatening, the pilot will take the decision to divert to the closest airport with proper medical facilities. The aircraft will resume its route after the person has been taken care of. The dataset contains 72 situations labelled as medical emergencies; most information is provided by Twitter accounts.

Practices about the use of the 7700 emergency code differ according to countries, only one medical issue in the dataset

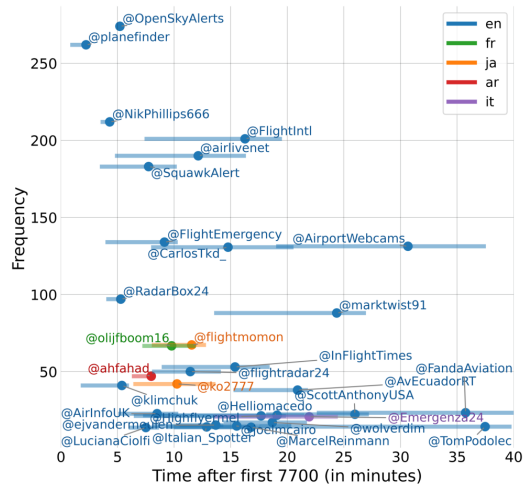


Fig. 6. Twitter accounts for which we have seen messages for at least 14 of our observed cases. The x-axis represents the median of the time delay between the first observed transponder code 7700 and the first observed tweet by that user for the cases. The horizontal error bar indicates the spread of delay times by spanning from first to third quartile of the distribution. The y-axis is the count of cases for which we have observed messages for the account. Colour highlights the main language of the tweets by that account.

diverted to an American airport (Dallas Fort-Worth KDFW). European ATC will often require aircraft to squawk 7700 for a priority landing, they will also get ARFF or ambulances ready at the airport. Twitter activities of popular accounts reveal many *non emergency* medical diversions to Gander CYQX or Saint-John CYYT airports on Newfoundland, Canada, before or after a transatlantic crossing. Figure 7 plots a situation when one of the pilots felt unwell. Passengers had to wait for several hours at the diversion airport before another pilot was able to reach Rennes LFRN.

b) *Cabin pressure issues:* During a flight, commercial aircraft are usually pressurised at an equivalent altitude of 10,000 ft (slightly more than 3,000 m). Issues with the pressurisation system or cracked windshields in the cockpit will most often lead to a steep descent to 10,000 ft (at up to $-6,000$ ft/min), which is illustrated in Figure 8. Then, flights are not necessarily diverted as it may become safe to fly at this altitude with a defunct pressurisation system. The dataset contains 31 situations labelled as cabin pressure or cracked windscreen issues, 27 of which leading to a diversion.

Regarding the situation shown in Figure 8, it is possible that most passengers did not notice any emergency until landing. The Aviation Herald mentioned the issue but only bots reacted to this event on Twitter.

c) *Fuel dumping:* Long-haul flights embark large amounts of fuel before take-off. Emergency landings may be performed at any time but a heavy landing provides a risk of significant damage to the structure of the aircraft. In order to avoid immobilising the aircraft for a mandatory maintenance

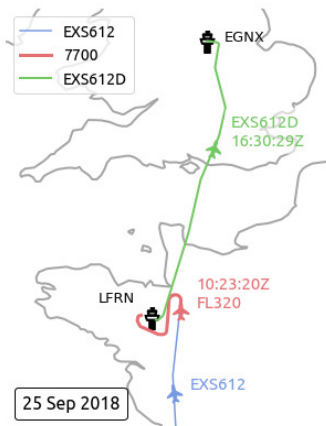


Fig. 7. On September 25th, 2018, Jet2.com flight EXS612/LS612 from Girona LEGE to East Midlands EGXN diverted to Rennes LFRN after one of the pilots felt unwell. Another pilot was flown to Rennes and the same aircraft took off again five hours later with callsign EXS612D.

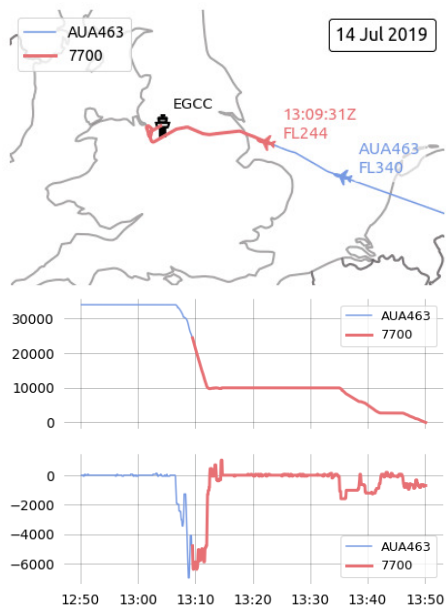


Fig. 8. On July 14th, 2019, Austrian Airlines flight AUA463/OZ463 from Vienna LOWW to Manchester EGCC started an early abrupt descent (down to -6,000ft/min) before starting to squawk the emergency code. Once at 10,000ft, the aircraft was considered safe to fly to its final destination without the need to divert. The same aircraft flew back to Vienna two days later, after a probable maintenance in Manchester.

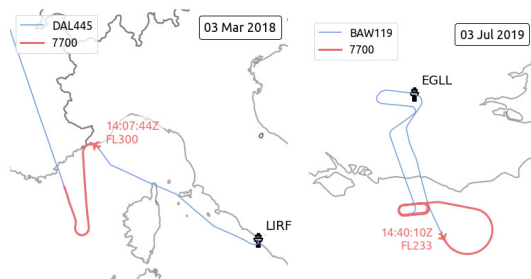


Fig. 9. On March 3rd, 2018, Delta Airlines flight DAL445/DL445 from Rome LIRF to New York JFK detected an instrument issue when reaching the vicinity of Nice. They turned over the Mediterranean sea to jettison fuel before diverting to Charles-de-Gaulle LFRN. On July 3rd, 2019, British Airways flight BAW119/BA119 bound for Bangalore VOBL interrupted their climb before FL240 and entered into a holding pattern over the Channel to jettison fuel before requesting a priority landing at Heathrow EGLL.

after a heavy landing, it is common practice to jettison fuel under close monitoring with the ATC until the aircraft is light enough to land safely. Fuel dumped above 6,000 ft will dissipate before reaching the ground.

Figure 9 shows two common patterns for fuel dumping: hippodrome-shaped holding patterns or a long detour above uninhabited areas. In the dataset, 32 aircraft were found to dump fuel according to external sources, among them 23 aircraft engaged in several holding patterns.

d) *Diversions due to weather:* Poor weather conditions are a common source of disruption in airline operations. Even if the airport is still open to landing in degraded mode, procedures may require a diversion after two failed attempts at landing at the same field. As aircraft divert to neighbouring airports, some of them could become short of fuel and ask for priority landing. Squawking 7700 can assist ATC in scheduling landing operations with this factor in mind.

Figure 10 plots two such situations. On January 14th 2020, Storm Brendan forced airlines bound to London to divert: crosswind gales of up to 80mph caused major disruption. Flight BAW79J/BA2777 entered a holding pattern before diverting to Birmingham EGBB. The 7700 emergency code was triggered after the decision to divert. On January 20th 2019, severe weather conditions (wind, snow and ice) at Boston Logan airport KBOS cancelled more than 10% of the scheduled flights. After UAL342/UA342 entered a holding pattern, they took the decision to divert before any landing attempt. They triggered the 7700 emergency code later: the hypothesis of low fuel is reasonable and is labelled accordingly based on analysis expressed on Twitter.

e) *Major technical issues:* Serious technical issues may lead to a diversion to the closest airport, not necessarily a major hub for the airline. When the aircraft is not fit for taking off again, solutions to accommodate passengers must be taken: they may be rebooked on different flights, driven by bus to a major airport or a replacement aircraft may be reserved or dispatched to fly people forward to their intended destination.

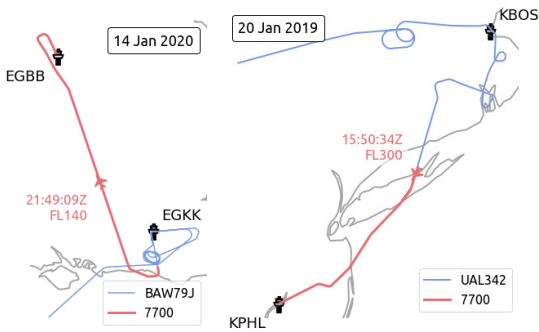


Fig. 10. British Airways BAW79J/BA2777 from Jersey EGJJ to London Gatwick EGKK diverted to Birmingham EGBB after two failed attempts at landing in gusty crosswinds of Storm Brendan in early January 2020. On January 20th, 2019, many flights to and from Boston Logan airport KBOS were cancelled because of severe wind, snow and ice conditions. United Airlines UAL342/UA342 from Chicago KORD was diverted to Philadelphia KPHL without any landing attempt.

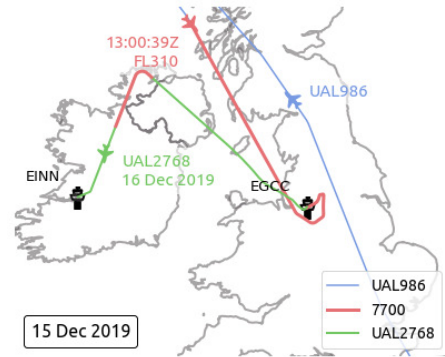


Fig. 13. On December 15th, 2019, United Airlines UAL986/UA986 from Paris CDG/LFPG to Chicago KORD diverted to Manchester EGCC after a suspicion of fuel leak. On the next day, as the aircraft was about to be ferried back to Chicago, it diverted to Shannon EINN with the same issue. It was finally sent back to Washington KIAD on December 19th.

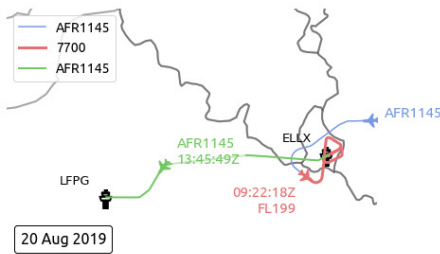


Fig. 11. On August 20th, 2019, Air France AFR1145/AF1145 from Moscow Sheremetyevo UUEE to Paris CDG/LFPG diverted to Luxembourg ELLX after an issue with the braking system. The aircraft did a first low approach, probably asking the tower for a visual inspection, before landing. The same aircraft resumed its flight to Paris few hours later.

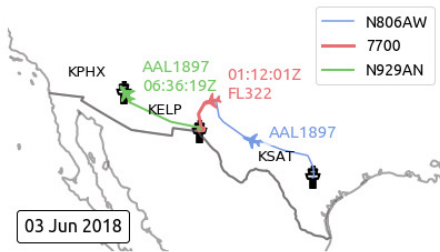


Fig. 12. On June 3rd, 2018, American Airlines AAL1887/AL1887 from San Antonio KSAT to Phoenix KPHX diverted to El Paso KEMP after experiencing turbulence and major damages to the aircraft. Few hours later, a replacement aircraft flew passengers to their final destination.

Illustrations include an emergency landing in Luxembourg for brake issues: the same aircraft took off later and returned to Paris with passengers on board (Figure 11); an emergency landing in El Paso after an aircraft experienced severe turbulence with serious damages to the windshield and nose: a replacement aircraft was used to take passengers to their final destination (Figure 12). Figure 13 displays an aircraft diverting to Manchester upon suspicion of a fuel leak: passengers were taken by bus to Heathrow. The next day, the same aircraft was ferried back to Chicago without passengers but had to divert again to Shannon airport.

f) *Atypical approaches:* Many emergency situations, technical or medical, do not lead to a diversion. The 7700 squawk code triggers a particular way of displaying the aircraft on all radar screens, even for controllers in charge of different sectors in the same ACC. Displaying 7700 may help ATC assisting the aircraft in providing ARFF on the runway or making them fly unbeaten tracks for a swift priority landing.

Figure 14 displays the trajectory of AFR48FC between Toulouse and Paris–Orly. All trajectories flying the same call sign in the same month are plotted in the background for reference: they mostly match the STAR procedure through ODILO (IAF). AFR48FC had a technical issue and squawked 7700 as they bypassed the usual procedure, descended with a very steep profile (several segments at less than $-3,000$ ft/min) for an emergency landing. Only bots reacted to the event on Twitter with no relevant information and it is reasonable to think most passengers did not notice anything unusual apart from the discomfort of a steep descent.

g) *Non-commercial flights:* The Airbus A300-600ST (Beluga) transports oversized aircraft components (like wings) between Airbus factories in Europe, including Toulouse, Saint-Nazaire (France), Hamburg (Germany) or Seville (Spain). On March 5th, 2018, one such aircraft bound for Saint-Nazaire LFRZ turned back to Toulouse during climb and aligned on

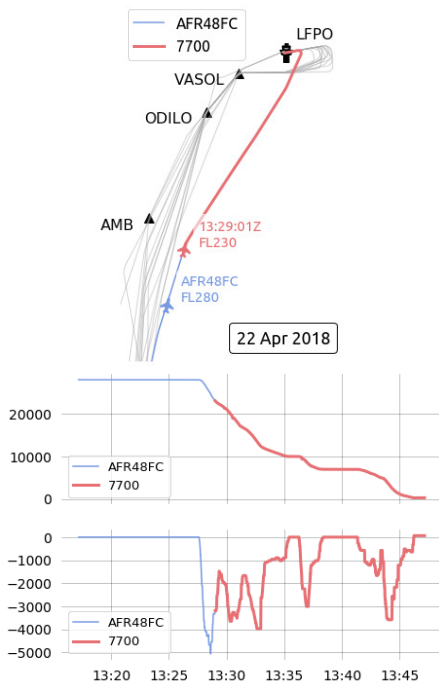


Fig. 14. On April 22nd 2018, Air France flight AFR48FC/AF6127 from Toulouse LFBO to Paris Orly LFPO squawked 7700 as they left the usual STAR procedure route (AMB ODILO VASOL) for a steep descent and a circle to land manoeuvre to landing.

runway 14R before heading aside, probably investigating a possible issue. Only after getting out of the two holding patterns did the Beluga start squawking 7700, probably to remind tower controllers they might need a particular attention, shall they need extra time on the runway or in case of a missed approach.

On July 15th 2019, private aircraft F-GJFE covered the Tour de France to relay audio and video signals from helicopters flying below to cover the 10th stage of the Grande Boucle between Saint-Flour and Albi. Few minutes after Wout Van Aert aced the sprint to stage victory in Albi, the aircraft headed west with an emergency squawk code before turning back to park in Castres LFCK. The nature of the issue remains unclear. There would have been time for maintenance on July 16th if needed, as it was a scheduled rest day. The aircraft was back in service on the Tour on July 17th between Albi and Toulouse.

Non-commercial flights are not very well covered in social networks as the general public is not much impacted. Naturally, emergency situations occur, too, but it is more difficult to get relevant contextual information from public sources.

V. OTHER TRANSPONDER CODES

While this work focuses on the 7700 emergency squawks, we briefly discuss the other two universal transponder codes,

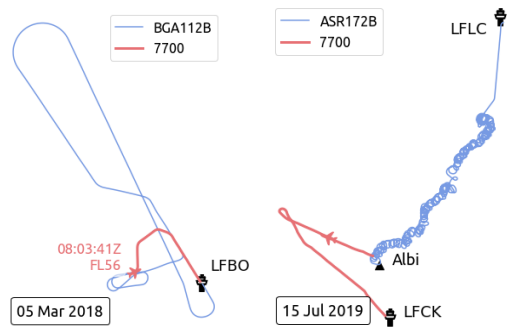


Fig. 15. Airbus Beluga flight BGA112B returned to Toulouse with a possible technical issue on March 5th, 2018. On July 15th 2019, private aircraft F-GJFE with callsign ASR172B covered the Tour de France between Saint-Flour and Albi to relay audio and video signals for television.

7500 and 7600 as they were seen, pre-filtered and stored by OpenSky's alert service. [10] We analysed a four-month period between 17 January 2020 and 17 May 2020.

A. 7500

Over the four months, four hijack codes of significant length were reported, none of which could be suspected as a relevant case. All were still relatively short lived (the median time was around 5 minutes); indicating a mistake by the pilot(s). For example, in one of the cases the aircraft eventually switched to 7600 on approach.

Taking a closer look at the raw flight data for the same period, over 8000 distinct aircraft reporting squawk 7500 were filtered out, as their squawks were only sent a single time or for a few seconds. In some cases, the short sequences seem to be glitches in systems or in transmission, e.g., a stream of code 1000 followed by a short sequence (2-3 seconds) of code 7500, followed again by code 1000. Some of these sequences are observed from state-of-the-art, new aircraft.

In further examining squawk 7500 incident tweets informally sampled using Google search, we found 29 tweets reporting hijack codes between 2017 and 2020. Out of these, 17 were issued from USAF aircraft, and none were related to an actual incident.

It is crucial to note that such errors with regards to 7500 can cause major disruption and are not to be taken lightly. For example, Amsterdam Schiphol airport made the news on November 6th 2019 when an Air Europa Airbus A300 EC-LQP accidentally started squawking the hijack code 7500. The aircraft was parked at the gate (outside the ground coverage of the OpenSky Network). Security procedures seriously disrupted the airport operations and parts of the terminal were closed to the public for several hours.

B. 7600

Over the four-month period, 70 radio failures were reported. While we cannot assume this period to be representative

due to the effect of the COVID-19 pandemic on aviation, in particular commercial and scheduled flights, we identified and categorised these occurrences. 5 (7%) were military planes, 10 (14%) commercial airliners, and the remaining 55 (79%) smaller private aircraft, mostly Cessnas or Pipers. Just over half (37 of 70 or 53%) occurred during approach with the 7600 code set during landing. The mean (median) time that the transponder code was set was 22 (11) minutes, respectively.

VI. DISCUSSION

As known within the aviation community and confirmed by our data analysis, a large majority of 7700 do not point towards safety-relevant events but are short-lived errors, which are possible at several levels (transponder setting, message decoding). Of those that can be assumed to be correctly set and decoded, many will still not produce a safety-related incident report or a noticeable diversion from planned flight plan or operating procedures. In case of a medical or unruly passenger issue or similar cases where the aircraft works normally, information provided by airline or third parties may shed some light on the reason as shown in our analysis in this paper.

While squawking 7700 in case of an emergency is not a requirement, it can be helpful for pilots in particular when in non-domestic airspaces. It is a proven way to get the undivided attention and priority by all ATC facilities in the area, even if a mayday – pan-pan call via radio is not an option [11]. As such, the 7700 squawk remains an important tool for ATC as any such aircraft is displayed prominently on all screens of the concerned Area Control Centers (ACC). As an alternative and complement to radio calls, it helps to clearly visualise that there is an important issue [12].

As using 7700 is not a requirement or always feasible, it should also be noted that there are many true emergencies where the transponder code is not set. Analysing this number was out of the scope of this work but it is estimated to be significant.

With regards to comparative analysis, it is important to consider the differences between airspaces and countries. For example, there are ATC facilities, which assign 7700 squawks to aircraft with any type of anomaly, e.g. routing problems, paperwork issues, or minor technical problems.

Besides the reason for applying emergency squawks, the timings can also differ. For example, we observe aircraft squawking 7700 when doing specific patterns related to the emergency and switch it off after the decision is taken (diversion for instance); some others investigate first and then switch the squawk to 7700 until landing.

With the high-profile nature of aviation accidents, there are regular cases of users and news reports jumping prematurely on reports of squawk codes instantly available through ADS-B networks, despite the low information value provided by 7700 squawk occurrences, as outlined in this paper. Taking all discussed issues together, we hope that our work provides some accessible background information that can counteract the fast-paced internet news and reporting cycle on aviation

accidents and prevent at least some premature speculation leading to potential anxiety and loss of trust.

VII. CONCLUSION

In this work, we used the data collected by the OpenSky Network over several years to analyse the occurrence and impact of emergency transponder codes, the well-known squawk 7700. While our results indicate that analysing the three universal squawks still requires significant manual work and some of the methods and gained insights are potentially airspace-specific, we showed that many relevant case studies can be obtained with our approach. By filtering and enriching the data with external data sources, we created a dataset that offers ground truth and thus opportunities for teaching, for ATC and pilot training using realistic emergency situation references and for further research. Eventually, it may also provide insights into the possible harmonisation of the handling of transponder codes both within and across airspaces.

ACKNOWLEDGEMENTS

The authors would like to give special thanks to Stefan Hradecky, the driving force behind The Aviation Herald, for his interesting comments and insights.

REFERENCES

- [1] M. Schäfer, X. Olive, M. Strohmeier, M. Smith, I. Martinovic, and V. Lenders, "OpenSky Report 2019: Analysing TCAS in the Real World using Big Data," in *2019 IEEE/AIAA 38th Digital Avionics Systems Conference (DASC)*. IEEE, 2019, pp. 1–10.
- [2] M. Schäfer, M. Strohmeier, M. Smith, M. Fuchs, R. Pinheiro, V. Lenders, and I. Martinovic, "OpenSky Report 2016: Facts and figures on SSR mode S and ADS-B usage," in *2016 IEEE/AIAA 35th Digital Avionics Systems Conference (DASC)*. IEEE, 2016, pp. 1–9.
- [3] "The Aviation Herald," accessed 2020-05-20. [Online]. Available: <https://www.avherald.com/>
- [4] M. Schäfer, M. Strohmeier, V. Lenders, I. Martinovic, and M. Wilhelm, "Bringing Up OpenSky: A Large-scale ADS-B Sensor Network for Research," in *Proceedings of the 13th IEEE/ACM International Symposium on Information Processing in Sensor Networks (IPSN)*, Apr. 2014.
- [5] M. Strohmeier, M. Schäfer, M. Fuchs, V. Lenders, and I. Martinovic, "OpenSky: A Swiss Army Knife for Air Traffic Security Research," in *Proceedings of the 34th IEEE/AIAA Digital Avionics Systems Conference (DASC)*, Sep. 2015.
- [6] M. Schäfer, M. Strohmeier, M. Smith, M. Fuchs, V. Lenders, and I. Martinovic, "OpenSky report 2018: assessing the integrity of crowdsourced mode S and ADS-B data," in *2018 IEEE/AIAA 37th Digital Avionics Systems Conference (DASC)*. IEEE, 2018, pp. 1–9.
- [7] X. Olive, "traffic, a toolbox for processing and analysing air traffic data," *Journal of Open Source Software*, vol. 4, no. 39, p. 1518, Jul. 2019. [Online]. Available: <http://joss.theoj.org/papers/10.21105/joss.01518>
- [8] X. Olive, A. Tanner, M. Strohmeier, M. Schäfer, M. Feridun, A. Tart, I. Martinovic, and V. Lenders, "Reference datasets for in-flight emergency situations," Jul 2020. [Online]. Available: <https://zenodo.org/record/3937483>
- [9] A. Tanner, A. Blarer, and V. Lenders, "Fusing flight data with social media data," in *NATO Science and Technology Organization: Big Data and Artificial Intelligence for Military Decision Making*, may 2018.
- [10] The OpenSky Network, Online, accessed 2020-05-20. [Online]. Available: <https://opensky-network.org/network/alerts>
- [11] I. Petchenik, "Squawking 7700—In-flight Emergencies from a Pilot's Perspective," Online, Oct. 2015, accessed 2020-05-20. [Online]. Available: <https://www.flightradar24.com/blog/squawking-7700-in-flight-emergencies-from-a-pilots-perspective/>
- [12] —, "Squawking 7700 — An Air Traffic Controller's Perspective on In-flight Emergencies," Online, Oct. 2015, accessed 2020-05-20. [Online]. Available: <https://www.flightradar24.com/blog/squawking-7700-an-air-traffic-controllers-perspective-on-in-flight-emergencies/>

CURRICULUM VITAE

Allan Tart

Institutions and positions

01.03.2018–...	Ericsson AB, Researcher (1,00)
01.07.2017–...	OpenSky Network, Researcher (0,50)
2010–...	Estonian Aviation Academy, Lecturer (0,10)
01.05.2015–	Estonian Air Navigation Services, Air Traffic Management
01.03.2017	Expert (1,00)
01.01.2008–	Estonian Air Navigation Services, Estonian Air Navigation
01.05.2015	Services, Head of Surveillance and Navigation Subdivision (1,00)

Education

2013–...	Tallinn University of Technology
2008–2012	Tallinn University of Technology
2001–2008	Tartu Aviation Collage

Academic degrees

Allan Tart, Master's Degree, 2012, (sup) Tõnu Trump, Algorithm Mode S sõnumi vastuvõtu parendamiseks (Algorithm for Enhancing Mode-S Message Reception), Tallinn University of Technology School of Information Technologies, Department of Radio and Communication Engineering.

Publications

2021

Tart, Allan; Trump, Tonu (2021). Position Report Enhancement Using Bayesian Estimator. IEEE Aerospace and Electronic Systems Magazine, 36 (1), 4–13. DOI: 10.1109/MAES.2020.3015604.

2020

Olive, Xavier; Tanner, Axel; Strohmeier, Martin; Schafer, Matthias; Feridun, Metin; Tart, Allan; Martinovic, Ivan; Lenders, Vincent (2020). OpenSky Report 2020: Analysing in-flight emergencies using big data. *2020 ALAA/IEEE 39th Digital Avionics Systems Conference (DASC)*. IEEE, 1–10. DOI: 10.1109/DASC50938.2020.9256787.

2017

Tart, A.; Trump, T. (2017). Addressing security issues in ADS-B with robust two dimensional generalized sidelobe canceller. *2017 22nd International Conference on Digital Signal Processing (DSP)*. IEEE, 1–5. DOI: 10.1109/ICDSP.2017.8096046.

2014

Tart, A.; Trump, T. (2014). Robust Adaptive Beamforming for Air Surveillance System using 2D Antenna Array. *Proceedings of the Tyrrhenian International Workshop on Digital Communications: Enhanced Surveillance of Aircraft and Vehicles: Tyrrhenian International Workshop on Digital Communications: Enhanced Surveillance of Aircraft and Vehicles*. Ed. G. Galati, P. van Gendeeren. IEEE, 129–134.

Tart, A.; Trump, T. (2014). Two Dimensional Robust Beamforming for Air-Ground Communication System. *Integrated Communications, Navigation and Surveillance Conference (ICNS); Westin Washington Dulles Airport, Herndon, Virginia, USA; April 8-10, 2014*. IEEE, B2-1–B2-8. DOI: 10.1109/ICNSurv.2014.6819978.

2013

Tart, A.; Trump, T. (2013). Adaptive Equalizer for Mode S Receiver. *8th International Workshop on Systems, Signal Processing and their Applications (WoSSPA), Mazafran, Algiers, Algeria, 12-15 May 2013*. IEEE, 277–282.

Trump, Tõnu; Tart, Allan (2013). A Dual Filter Scheme for Secondary Surveillance Radar Reply Signals. In: E.O. Ahmed, K.Y. Kim, Y. Shang, T. Draganova, M. Roushdy and A.M. Salem (Ed.). *Recent Advances in Telecommunications* (149–154). Dubrovnik, Croatia: WSEAS. (Recent Advances in Electrical Engineering Series).

ELULOOKIRJELDUS

Allan Tart

Töökohad ja ametid

01.03.2018–...	Ericsson AB, Teadur (1,00)
01.07.2017–...	OpenSky Network, Teadur (0,50)
2010–...	Eesti Lennuakadeemia, Lektor (0,10)
01.05.2015–	Estonian Air Navigation Services, ekspert (1,00)
01.03.2017	
01.01.2008–	Lennuliiklusteeninduse Aktsiaselts, Lennuliiklusteeninduse AS,
01.05.2015	seire- ja navigatsioonisüsteemide talituse juht (1,00)

Haridustee

2013–...	Tallinna Tehnikaülikool
2008–2012	Tallinna Tehnikaülikool
2001–2008	Tartu Lennukolledž

Teaduskraadid

Allan Tart, magistriskraad, 2012, (juh) Tõnu Trump, Algoritm Mode S sõnumi vastuvõtu parendamiseks, Tallinna Tehnikaülikool, Infotehnoloogia teaduskond, Raadio- ja sidetehnika instituut.

Publikatsioonid

2021

Tart, Allan; Trump, Tõnu (2021). Position Report Enhancement Using Bayesian Estimator. IEEE Aerospace and Electronic Systems Magazine, 36 (1), 4–13. DOI: 10.1109/MAES.2020.3015604.

2020

Olive, Xavier; Tanner, Axel; Strohmeier, Martin; Schafer, Matthias; Feridun, Metin; Tart, Allan; Martinovic, Ivan; Lenders, Vincent (2020). OpenSky Report 2020: Analysing in-flight emergencies using big data. 2020 AIAA/IEEE 39th Digital Avionics Systems Conference (DASC). IEEE, 1–10. DOI: 10.1109/DASC50938.2020.9256787.

2017

Tart, A.; Trump, T. (2017). Addressing security issues in ADS-B with robust two dimensional generalized sidelobe canceller. *2017 22nd International Conference on Digital Signal Processing (DSP)*. IEEE, 1–5. DOI: 10.1109/ICDSP.2017.8096046.

2014

Tart, A.; Trump, T. (2014). Robust Adaptive Beamforming for Air Surveillance System using 2D Antenna Array. *Proceedings of the Tyrrhenian International Workshop on Digital Communications: Enhanced Surveillance of Aircraft and Vehicles: Tyrrhenian International Workshop on Digital Communications: Enhanced Surveillance of Aircraft and Vehicles*. Ed. G. Galati, P. van Gendeeren. IEEE, 129–134.

Tart, A.; Trump, T. (2014). Two Dimensional Robust Beamforming for Air-Ground Communication System. *Integrated Communications, Navigation and Surveillance Conference (ICNS); Westin Washington Dulles Airport, Herndon, Virginia, USA; April 8-10, 2014*. IEEE, B2-1–B2-8. DOI: 10.1109/ICNSurv.2014.6819978.

2013

Tart, A.; Trump, T. (2013). Adaptive Equalizer for Mode S Receiver. *8th International Workshop on Systems, Signal Processing and their Applications (WoSSPA), Mazafran, Algiers, Algeria, 12-15 May 2013*. IEEE, 277–282.

Trump, Tõnu; Tart, Allan (2013). A Dual Filter Scheme for Secondary Surveillance Radar Reply Signals. In: E.O. Ahmed, K.Y. Kim, Y. Shang, T. Draganova, M. Roushdy and A.M. Salem (Ed.). *Recent Advances in Telecommunications* (149–154). Dubrovnik, Croatia: WSEAS. (Recent Advances in Electrical Engineering Series).

ISSN 2585-6901 (PDF)
ISBN 978-9949-83-700-7 (PDF)